PONTIFÍCIA UNIVERSIDADE CATÓLICA
DO RIO DE JANEIRO

Emanuel do Couto Pessanha

Solar light-sensitive heterostructured nanomaterials: enhancing photocatalytic hydrogen production and probing ROS generation for environmental remediation

Tese de Doutorado

Thesis presented to the Programa de Pós-Graduação em Engenharia Química, de Materiais e Processos Ambientais of PUC-Rio in partial fulfillment of the requirements for the degree of Doutor em Engenharia Química, de Materiais e Processos Ambientais.

Advisor: Prof. Bojan Marinkovic

Rio de Janeiro
April 2024

Emanuel do Couto Pessanha

Solar light-sensitive heterostructured nanomaterials: enhancing photocatalytic hydrogen production and probing ROS generation for environmental remediation

Thesis presented to the Programa de Pós-Graduação em Engenharia Química, de Materiais e Processos Ambientais of PUC-Rio in partial fulfillment of the requirements for the degree of Doutor em Engenharia Química, de Materiais e Processos Ambientais. Approved by the Examination Committee.

Prof. Bojan Marinkovic
Advisor
Pontifícia Universidade Católica do Rio de Janeiro (PUC-Rio)

Prof. Jordi Llorca Piqué
Co-Advisor
Universitat Politècnica de Catalunya (UPC)

Dr. Edisson Morgado Junior
Pesquisador Autônomo

Prof. Marco André Fraga
Institudo Nacional de Tecnologia (INT)

Prof^a^. Anupama Ghosh
Pontifícia Universidade Católica do Rio de Janeiro (PUC-Rio)

Prof. Roberto Ribeiro de Avillez
Pontifícia Universidade Católica do Rio de Janeiro (PUC-Rio)

Rio de Janeiro, April 29th, 2024.

All rights reserved.

Emanuel do Couto Pessanha

Graduated in Mechanical Engineering at Universidade Candido Mendes (UCAM) in 2017 and obtained his M.Sc. Degree in Materials Science and Engineering from Universidade Estadual do Norte Fluminense Darcy Ribeiro (UENF). He had experience in physical metallurgy, mechanical properties of metallic materials, synthesis and characterization of nanostructures, visible light-sensitive TiO_2-based nanomaterials, and photocatalysis. Currently, he works as researcher specializing in X-ray diffraction, thermogravimetric analysis, scanning electron microscopy and X-ray fluorescence.

Ficha Catalográfica

Pessanha, Emanuel do Couto

Solar light-sensitive heterostructured nanomaterials: enhancing photocatalytic hydrogen production and probing ROS generation for environmental remediation / Emanuel do Couto Pessanha; advisor: Bojan Marinkovic. – Rio de Janeiro: PUC, Departamento de Engenharia Química e de Materiais, 2024.

135 f.: il. color.; 30 cm

Tese (doutorado) - Pontifícia Universidade Católica do Rio de Janeiro, Departamento de Engenharia Química e de Materiais.

Inclui referências bibliográficas.

1. Engenharia Química e de Materiais – Teses. 2. Metais abundantes. 3. heterojunção p-n. 4. Coleta de energia. 5. H_2 verde. 6. Engenharia de banda. 7. Remoção por adsorção. I. Marinkovic, Bojan. II. Pontifícia Universidade Católica do Rio de Janeiro. Departamento de Engenharia Química e de Materiais. III. Título.

CDD: 620.11

To my parents, Walfredo and Mônica, to my sisters, Maria Carolina and Maria Letícia, and to my fiancée, Maria Fernanda.

Acknowledgments

First and foremost, I thank God for His grace, mercy, and daily sustenance.

I am grateful to my family and my fiancée for their support and unconditional love.

I express my deep gratitude to my advisor, Prof. Bojan Marinkovic, for trusting in my abilities, opportunities granted to me, guidance, support, and fruitful discussions throughout this process. His dedication and guidance were crucial for the development of this thesis. I also thank my co-advisor, Prof. Jordi Llorca, for his guidance, support, fruitful discussions, and for opening the doors of his laboratory and providing all the infrastructure of the Nanoengineering of Materials Applied to Energy (NEMEN) so that I could work.

I express my sincere gratitude to my friends and colleagues from Center for Research and Advanced Characterization of Materials (CePeCAM) and the Department of Chemical and Materials Engineering (Deqm) at PUC-Rio. Your contributions, discussions, and feedback were extremely valuable for this work. In particular, I thank Lucas Almeida, Juliana Viol, Freddy Rojas, Fabián Orozco, Esteban Camilo, Ananias Emmerick, Andres Esteban, Jessica Gil, and Marianne Diniz.

I thank the institutions which, through the access granted to their infrastructure, also made possible the realization of this research. To Prof. Paula Jardim and Dr. Beatriz Canabarro from UFRJ, for TEM analyses. To Prof. André Guimarães and M.Sc. Francine Menezes from UENF, for EPR analyses. To Prof. Eliane D'Elia and M.Sc. Victor Magno Paiva from UFRJ, for EIS analyses. To Dr. Thiago Mori from the Brazilian Synchrotron Light Laboratory (LNLS - CNPEM), for XAS analyses.

Finally, I would like to express my gratitude to all the people who in some way contributed to the development of this Thesis, even if not directly mentioned here.

This work would not have been possible without the support and contributions of each of you. Thank you very much!

This study was financed by the Coordenação de Aperfeiçoamento de Pessoal de Nível Superior - Brasil (CAPES) - Finance Code 001.

Abstract

Pessanha, Emanuel do Couto; Marinkovic, Bojan (Advisor); Piqué, Jordi Llorca (Co-Advisor). **Solar light-sensitive heterostructured nanomaterials: enhancing photocatalytic hydrogen production and probing ROS generation for environmental remediation**. Rio de Janeiro, 2024. 135p. Tese de Doutorado - Departamento de Engenharia Química e de Materiais, Pontifícia Universidade Católica do Rio de Janeiro.

Solar light-responsive heterostructures hold great potential in different applications toward a clean and sustainable future, such as hydrogen (H_2) photoproduction and environmental remediation. In the context of photocatalysis, titanium dioxide (TiO_2) plays a crucial role due to its wide range of applications, excellent chemical stability, low toxicity, and relatively low cost. However, neat TiO_2 has some shortfalls, such as a high recombination rate and low sensitivity to solar light, which limits its efficiency in photocatalytic applications in general. Therefore, the continuous development of new materials aimed at improving these limitations is mandatory. Among the approaches to overcome the neat TiO_2 shortfalls is the formation of heterojunctions with suitable semiconductors, improving charge separation and, therefore, photocatalytic efficiency. Nickel oxides and copper oxides are reported as promising alternatives for forming heterojunctions with TiO_2, enhancing the charge transfer and broadening the light absorption in the visible spectrum. This thesis presents different studies aimed at the synthesis and characterization of new efficient heterostructured nanomaterials for photocatalytic hydrogen generation and hazardous pollutants abatement. In the first study, a NiO/TiO_2 p-n heterojunction obtained via mechanochemistry was reported, which exhibited an improved solar-driven H_2 photoproduction rate compared to neat TiO_2 (8.85 mmol h^{-1} g^{-1} *vs.* 0.73 mmol h^{-1} g^{-1}). In all cases, the addition of NiO supported on TiO_2 reduced the recombination rate and enhanced the visible light absorption. TEM, XPS, and XAS studies demonstrated that a homogenous dispersion and a favorable spin configuration of NiO clusters supported on TiO_2 were responsible for the superior efficiency exhibited by the sample prepared via mechanochemistry, labeled as NiO/P90-BM. Noticeably, cycling, long-term, and aging tests have shown that the reported photocatalyst is efficient after several cycles, prolonged use, and after long periods of storage. Furthermore, studies combining EPR and the spin trapping technique were carried out to delve into the production of superoxide $(O_2^{-\bullet})$ and hydroxyl $(OH^{\bullet})$ by NiO/TiO_2 heterojunctions. These studies provided insights into the potential application of the NiO/TiO_2 heterojunctions for the photocatalytic degradation of gaseous and aqueous pollutants. The EPR results shed light on the NiO/P90-BM sample as the most efficient in ROS photogeneration, revealing that mechanochemical synthesis resulted in a more efficient architecture for generating $O_2^{-\bullet}$ and $OH^{\bullet}$ radicals. Besides, a simple soft chemistry route was reported to prepare a heterostructure of cuprous oxide nanocubes (Cu_2O NCs) and TiO_2, labeled as Cu_2O NCs/TiO_2, as an efficient adsorbent for tetracycline (TC), which is a broad-spectrum antibiotic. FTIR and TGA were carried out before and after the adsorption process to demonstrate the adsorption of TC by the Cu_2O NCs/TiO_2 heterostructure. Additionally, tests with visible light irradiation were performed to distinguish between adsorption and photocatalytic removal processes. In addition, EPR measurements were also carried out using spin trapping to investigate the ROS photoproduction. Interestingly, there was no detectable ROS photoproduction by the Cu_2O NCs/TiO_2 heterostructure, demonstrating that TC removal is solely due to adsorption. These results contribute to clarifying a discrepancy in the literature regarding the photocatalytic activity of Cu_2O NCs under visible light. Collectively, this research has advanced the understanding of photocatalytic mechanisms and reported new heterostructured nanomaterials, while highlighting their potential for sustainable applications in diverse environmental and energy transition related contexts.

Keywords

Earth-abundant metals; p-n heterojunction; Energy harvesting; green H_2; Bandgap engineering; Adsorptive removal.

Resumo

Pessanha, Emanuel do Couto; Marinkovic, Bojan (Advisor); Piqué, Jordi Llorca (Advisor). **Heteroestruturas de nanomateriais sensíveis à luz solar: aprimoramento de produção fotocatalítica de hidrogênio e exploração da geração dos ROS para remediação ambiental**. Rio de Janeiro, 2024. 135p. Tese de Doutorado - Departamento de Engenharia Química e de Materiais, Pontifícia Universidade Católica do Rio de Janeiro.

Heteroestruturas sensíveis à luz solar possuem grande potencial em diferentes aplicações direcionadas a um futuro limpo e sustentável, como a fotoprodução de hidrogênio (H_2) e a remediação ambiental. No contexto da fotocatálise, o dióxido de titânio (TiO_2) desempenha um papel crucial devido à sua ampla gama de aplicações, excelente estabilidade química, baixa toxicidade e custo relativamente baixo. No entanto, o TiO_2 puro possui algumas desvantagens, como uma alta taxa de recombinação e baixa sensibilidade à luz solar, o que limita sua eficiência em aplicações fotocatalíticas. Portanto, o desenvolvimento contínuo de novos materiais com o objetivo de superar essas desvantagens é obrigatório. Entre as abordagens reportadas para superar as deficiências do TiO_2 puro está a formação de heterojunções com outros semicondutores, melhorando a separação de cargas e, portanto, a eficiência fotocatalítica. Óxidos de níquel e óxidos de cobre são relatados como alternativas promissoras para a formação de heterojunções com TiO_2, melhorando a transferência de carga e aumentando a absorção de luz no espectro visível do TiO_2 puro. Esta tese apresenta diferentes estudos voltados para a síntese e caracterização de novos nanomateriais heteroestruturados eficientes para geração fotocatalítica de hidrogênio e degradação de poluentes perigosos. No primeiro estudo, foi relatada uma heterojunção p-n de NiO/TiO_2 obtida via mecanoquímica, que apresentou uma taxa elevada de fotoprodução pelo sol de H_2 em comparação com o TiO_2 puro (8.85 mmol h^{-1} g^{-1} *vs.* 0.73 mmol h^{-1} g^{-1}). Em todos os casos, a adição de NiO suportado em TiO_2 reduziu a taxa de recombinação e aumentou a absorção de luz visível. Estudos de TEM, XPS e XAS demonstraram que uma dispersão homogênea e uma configuração de spin favorável dos pequenos aglomerados de NiO suportados em TiO_2 foram responsáveis pela eficiência superior exibida pela amostra preparada via mecanoquímica, denominada NiO/P90-BM. Notavelmente, testes de ciclagem, de longo prazo e de envelhecimento mostraram que o fotocatalisador relatado é eficiente após vários ciclos, para uso prolongado e após longos períodos de armazenamento. Além disso, foram realizados estudos combinando EPR e a técnica de captura de spin para aprofundar na produção de superóxido ($O_2^{-\bullet}$) e hidroxila ($OH^{\bullet}$) pelas heterojunções de NiO/TiO_2. Esses estudos forneceram insights sobre a aplicação potencial das heterojunções de NiO/TiO_2 para a degradação fotocatalítica de poluentes gasosos e aquosos. Os resultados de EPR lançaram luz sobre a amostra de NiO/P90-BM como a mais eficiente na fotogeração de ROS, revelando que a síntese mecanoquímica resultou em uma arquitetura mais eficiente para a geração de radicais $O_2^{-\bullet}$ e $OH^{\bullet}$. Finalmente, foi relatada uma rota simples de química branda para preparar uma heteroestrutura de nanocubos de óxido cúprico (Cu_2O NCs) e TiO_2, denominada Cu_2O NCs/TiO_2, como um adsorvente eficiente para a tetraciclina (TC), que é um antibiótico de amplo espectro. FTIR e TGA foram realizados antes e após o processo de adsorção para demonstrar a adsorção de TC pela heteroestrutura Cu_2O NCs/TiO_2. Além disso, foram realizados testes com irradiação de luz visível para distinguir entre os processos de remoção por adsorção e fotocatalítica. Além disso, foram realizadas medições de EPR usando captura de spin para investigar a fotoprodução de ROS. Curiosamente, não houve fotoprodução de ROS detectável pela heteroestrutura Cu_2O NCs/TiO_2, demonstrando que a remoção de TC é exclusivamente devido à adsorção. Estes resultados contribuem para esclarecer uma discrepância na literatura quanto à atividade fotocatalítica dos Cu_2O NCs sob luz visível. Coletivamente, esta pesquisa avançou o entendimento dos mecanismos fotocatalíticos e relatou novos nanomateriais heteroestruturados, destacando seu potencial para aplicações sustentáveis em diversos contextos relacionados ao meio ambiente e transição energética.

Palavras-chave

Metais abundantes; heterojunção p-n; Coleta de energia; H_2 verde; Engenharia de banda; Remoção por adsorção.

Contents

List of Figures

List of Tables

List of Equations

“Pensava que quando se sonha tão grande a realidade aprende.”
O filho de mil homens: Valter Hugo Mãe

“Fazer o poema da consciência humana, ainda que fosse a respeito de um só homem, e ainda que fosse a respeito do mais ínfimo dos homens, seria fundir todas as epopeias em uma epopeia superior e definitiva.”
Os Miseráveis: Victor Hugo

1.
Introduction

The extensive use of fossil fuels has been linked to serious environmental issues, including risks to ecosystems and the Earth's climate (Höök e Tang, 2013). For more than a century, coal, oil, and natural gas have been used as the world's primary energy sources (Panwar, Kaushik e Kothari, 2011; Shirazi e Fuinhas, 2023). However, their extensive usage has resulted in various detrimental effects, including air and water pollution, and greenhouse gas emissions that trap heat and contribute to global warming (Soeder, 2021). For instance, smog, acid rain, and various respiratory and cardiovascular health issues in humans are all potential outcomes resulting from the release of these air pollutants during the combustion of fossil fuels. Additionally, accidental spills and leaks from fossil fuel extraction, processing, and transportation can contaminate water sources, disturbing and destroying the delicate balance of aquatic ecosystems, and generating socio-economic problems (Burgherr, 2007; Durango-Cordero *et al.*, 2018). To address these environmental issues, it must have a global transition towards sustainable, renewable, and carbon-free energy sources.

In this framework, hydrogen (H_2) is an effective and frequently regarded as the most promising energy carrier for creating a low-carbon economy (Dutta, 2021). The H-H bond can release chemical energy when it combines with oxygen, *i.e.*, during the combustion, producing solely harmless water as a byproduct in a highly exothermic process (Dutta, 2021). In fact, among the frequently utilized gaseous, liquid, and solid fuels, H_2 has the largest energy content per mass (Sarker *et al.*, 2023). Since Fujishima and Honda's pioneering study on photoelectrocatalytic water splitting on a TiO_2 electrode (FUJISHIMA e HONDA, 1972), photocatalysis has been considered a promising way to generate green H_2.

Moreover, another emergent environmental issue arises from aqueous pollution caused by the release of antibiotics into water bodies through various routes. The emergence of multidrug-resistant bacteria (MDR) is among the major risks for humans related to aqueous pollution from antibiotics (Zhang *et al.*, 2015). Antibiotic exposure at sub-lethal doses in aquatic environments can lead to the selection and multiplication of bacteria that are resistant to these antibiotics, giving rise to antibiotic-resistant bacteria (ARB) and MDR (Larsson e Flach, 2021). This poses a severe hazard to public health, as it reduces the effectiveness of medicines in treating infections. It is important to highlight that current wastewater treatment procedures are ineffective at eliminating antibiotics, contributing to their persistence in the environment (Almeida *et al.*, 2022a; Rogowska *et al.*, 2020). To address this issue, a multifaceted strategy is required, including improved and new wastewater treatment approaches, stronger legislation, as well as other actions.

Likewise in the case of H_2 generation, photocatalysis has demonstrated a remarkable potential for antibiotic abatement, notably in wastewater treatment and environmental remediation (Wei, Liu e Shangguan, 2020). Thus, photocatalysis can play a pivotal role as an effective and sustainable method for the abatement of antibiotic pollution by converting popular antibiotics, such as tetracycline, sulfamethoxazole, and ciprofloxacin, into harmless products by photochemical processes. For instance, antibiotics may undergo complete mineralization during photocatalysis, generating carbon dioxide, water, and harmless inorganic chemicals (Adeyemi, Ajiboye e Onwudiwe, 2021). This mineralization process promotes the antibiotic's eradication and mitigate its adverse effects on the environment.

Due to its advantageous properties, TiO_2-containing photocatalysts have mostly been reported for H_2 photoproduction as well as for photocatalytic pollutant degradation. However, to improve the photocatalytic efficiency of neat TiO_2, some shortfalls must be addressed, namely the high recombination rate and the low solar light sensitivity.

This Thesis is organized as follows:

- Chapter 2: Literature review, where the fundamental principles of heterogeneous photocatalysis are presented, the pivotal role played by TiO_2 in this context, and some of the strategies used to enhance its efficiency as a catalyst. Also, mechanochemical synthesis is presented and how it has been employed to prepare highly efficient catalysts. Finally, the topic of facet engineering is presented, and how this strategy can be used to increase the efficiency of catalysts.

- Chapter 3: Objectives of this Thesis.

- Chapter 4: Mechanochemical approach towards optimized Ni^{2+} spin configuration in NiO/TiO_2 heterojunction with enhanced solar-driven H_2 photoproduction.

- Chapter 5: Efficient sunlight-driven photoproduction of superoxide and hydroxyl radicals by mechanochemically synthesized NiO/TiO_2 heterojunction: Insights from EPR/spin trapping.

- Chapter 6: Cu_2O nanocubes/TiO_2 heterostructure and its adsorption and photocatalytic properties for tetracycline removal (Pessanha *et al.*, 2023).

- Chapter 7: General conclusions and prospects for future works.

2.
Literature Review

2.1.
Fundamentals of Heterogeneous Photocatalysis

According to the IUPAC (International Union of Pure and Applied Chemistry), the process of photocatalysis is defined as follows: a change in the rate of a chemical reaction - or its initiation - under the action of ultraviolet, visible, or infrared radiation in the presence of a substance - the photocatalyst - that absorbs light and is involved in the chemical transformation of the reaction participants. Furthermore, the term "heterogeneous" aims to differentiate heterogeneous photocatalysis from homogeneous photocatalysis, in which the photocatalyst is dissolved in a solution forming a homogeneous mixture. On the other hand, in heterogeneous photocatalysis, the photocatalyst is in the solid state and acts as a separate phase within the medium where the reactions take place. Typically, inorganic semiconductors are used in heterogeneous photocatalysis (Braslavsky, 2007; García-López e Palmisano, 2021).

The phenomena involved in heterogeneous photocatalysis can be understood at a more fundamental level by considering the theory of molecular orbitals. In broad terms, this theory posits that the bonds between atoms occur through the formation of molecular orbitals (MOs). MOs are obtained by linearly combining the wave functions that describe the atomic orbitals (AOs) involved in the molecule's formation. Considering the wave-like nature of the electrons involved in bonding, two types of interaction are possible: constructive interaction – resulting from the sum of the wave functions – and destructive interaction – resulting from the subtraction of the wave functions. The first type of interaction will give rise to the so-called bonding molecular orbital (BMO), which will have lower energy than the AOs from which it originated. On the other hand, the second type of interaction will generate the antibonding molecular orbital (ABMO), with energy higher than that of the AOs that gave rise to it (Atkins *et al.*, 2010).

To illustrate the above, one can consider a simple example, demonstrating how the theory of molecular orbitals describes the connection between two hydrogen atoms to form a hydrogen molecule.

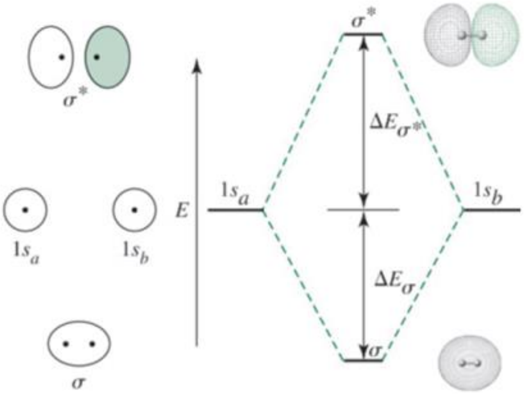

Figure 1: Molecular orbitals of hydrogen formed by the combination of the 1s atomic orbitals of two hydrogen atoms (Miessler, Fischer e Tarr, 2014).

As can be observed by analyzing Figure 1, the 1s atomic orbitals of the two hydrogen atoms approach and interact, giving rise to a stabilized molecular orbital (σ), *i.e.*, the BMO, and a destabilized molecular orbital (σ*), *i.e.*, the ABMO. Considering the above for a material composed of many atoms, it can be considered that, from the contribution of many stabilized molecular orbitals (σ) and destabilized molecular orbitals (σ*), energy bands will form through the overlap of the molecular orbitals (Figure 2) (West, 2014).

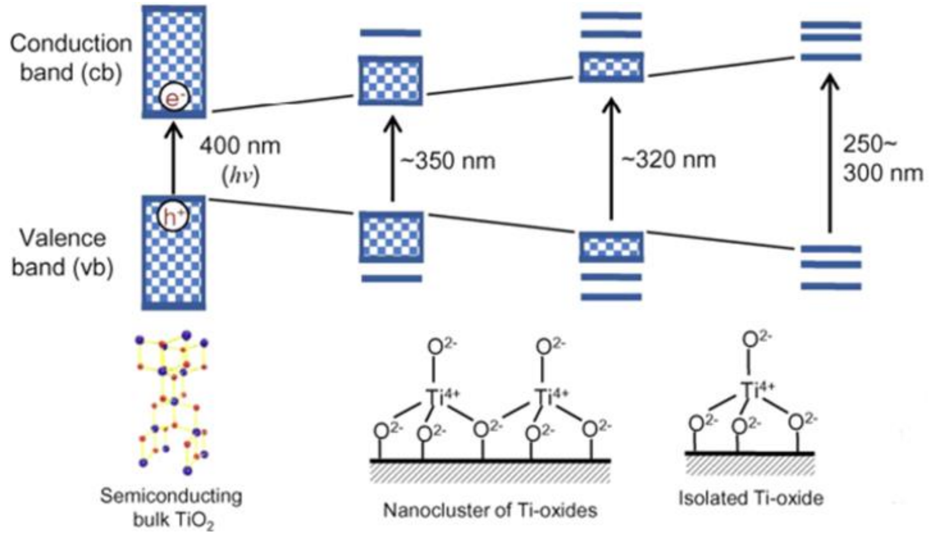

Figure 2: Schematic representation of the change in dimension and structure of the electronic bands of a semiconductor as a function of the number of atoms (Ma *et al.*, 2014).

It is worth noting that the formed bands do not consist of a continuum of energy. The designation of bands is because the energy levels between same type of MO (Molecular Orbitals) are quite narrow, and seems like a continuum of energy at first glance - see highlight in Figure 3 (Atkins *et al.*, 2010).

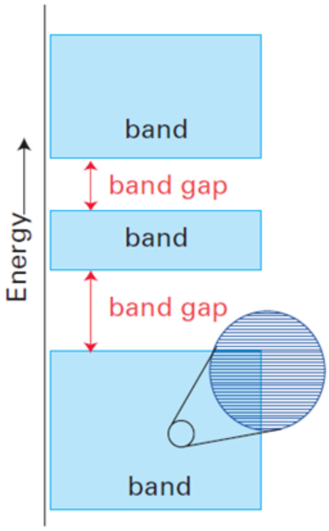

Figure 3: Energy bands formed by the contribution of a large number of molecular orbitals (Atkins *et al.*, 2010).

The band originating from the BMOs is called the valence band (VB), while the ABMOs give rise to the so-called conduction band (CB). These bands, in semiconductors and insulators, are separated by an energy gap - called the band gap (E_g), which consists of an energy interval for which no molecular orbitals are formed, and, consequently, cannot be occupied by electrons. The value of the E_g of a semiconductor corresponds to the energy difference between the top of the VB and the bottom of the CB (Miessler, Fischer e Tarr, 2014; Serpone e Emeline, 2002).

Considering the above, in photocatalysis, upon the incidence of photons with energy greater than or equal to the E_g of the material acting as a photocatalyst, there will be the absorption of photons by the material (Figure 4). The absorbed photons promote the generation of electron/hole pairs (e^-/h^+) (Figure 4 - i). These two types of charge carriers can diffuse to the surface of the photocatalyst (Figure 4 - ii) and participate in reduction (Figure 4 - v) and oxidation (Figure 4 - vi) semi-reactions or undergo processes of bulk and/or surface recombination (Figure 4 - iii and iv).

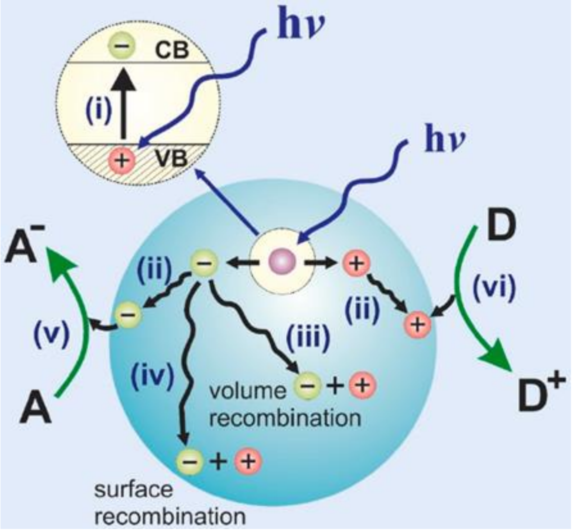

Figure 4: Schematic representation of the phenomena involved in photocatalysis (Xia *et al.*, 2022).

Finally, it is worth noting that the field of heterogeneous photocatalysis has been the subject of significant scientific and technological interest. This is due to the potential that the processes involved in this phenomenon could assist in resolving environmental emerging issues in the present and those projected as inevitable soon. Some examples of potential applications of photocatalysis include inactivation of pathogenic microorganisms, hydrogen production, and reduction of gaseous and liquid pollutants (Chen *et al.*, 2010; Dell'Edera *et al.*, 2021; Fuentes, Tapia e Pozo, 2021; Habibi-Yangjeh *et al.*, 2020; Habran, Krambrock, *et al.*, 2018; Pasquale, De *et al.*, 2021; Xia *et al.*, 2022).

2.1.1.
Heterogeneous photocatalysis on TiO_2

In the context of photocatalysis, from early studies to current research, TiO_2 plays a dominant role in various applications. This is mainly due to the properties that TiO_2 exhibits. Among these properties, its wide applicability for different purposes stands out due to the positioning of the VB and CB on the redox potential scale. Additionally, it demonstrates high chemical stability over a wide range of conditions, non-toxicity, and low cost (Hashimoto, Irie e Fujishima, 2005; Nakata e Fujishima, 2012; Nunes *et al.*, 2021).

Titanium dioxide exhibits polymorphism, with its main phases being anatase, rutile, and brookite (Figure 5). Anatase and rutile phases have a tetragonal structure. In anatase, the TiO_6 octahedra share edges, while in rutile, they share edges and vertices. In the case of brookite, the adopted structure is orthorhombic with the sharing of edges and vertices by the TiO_6 octahedra. As can be seen, all three phases can be depicted as composed of distorted TiO_6 octahedra arranged in different patterns (Colmenares e Xu, 2016; Dambournet, Belharouak e Amine, 2010).

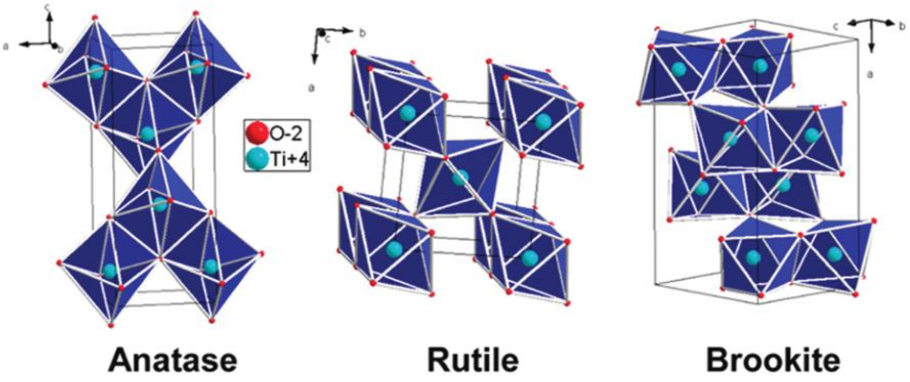

Figure 5: Most common polymorphs of TiO_2 (Dambournet, Belharouak e Amine, 2010).

Among the mentioned phases above, rutile is the thermodynamically stable phase. Also, for photocatalytic applications, rutile and anatase are referred in the literature as the most relevant phases of TiO_2 (Ma *et al.*, 2014).

Figure 6 presents the resulting molecular orbitals from the interaction between the atomic orbitals of titanium and oxygen in rutile and anatase. As can be observed, for both polymorphs of TiO_2, the VB - filled in the ground state - is predominantly composed of O 2p orbitals. On the other hand, the CB - empty in the ground state - is formed by the contribution of Ti 3d, Ti 4s, and Ti 4p orbitals. Regarding E_g, the values are approximately $E_g \sim 3$ eV for rutile and $E_g \sim 3.2$ eV for anatase (Ma *et al.*, 2014; Thomas *et al.*, 2007).

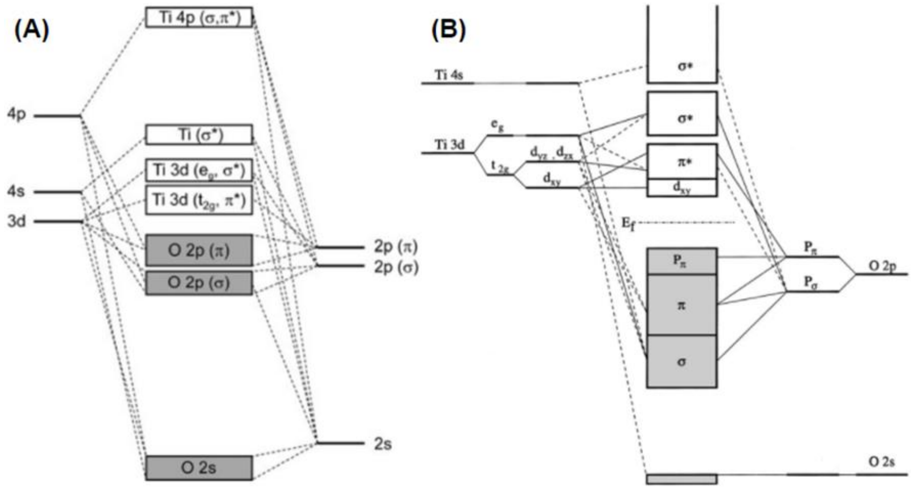

Figure 6: Molecular orbitals for Ti–O bonding in rutile (A) and anatase (B) (Asahi, Taga e Mannstadt, 2000; Krol e Grätzel, 2012).

Comparatively, despite having a larger band gap, anatase exhibits higher photocatalytic activity than rutile. Among the reasons for this are the type of electronic transition involved in the recombination process of photo-generated electron-hole pairs and, consequently, the charge carries' lifetime (Luttrell *et al.*, 2015; Zhang *et al.*, 2014).

Regarding the type of electronic transition performed in recombination, it will depend on the wave vector of the CB and VB. If the bottom of the CB and the top of the VB correspond to the same wave number, a direct transition will occur upon recombination – where the emission of a photon takes place (Figure 7 - b). On the other hand, if the wave number is different, the transition observed in recombination will be indirect – requiring the release of a phonon in addition to the photon (Figure 7 - a) (Mannu, Pietro, Di e Mele, 2020).

The type of transition has a direct implication on the lifetime of electron-hole pairs. The indirect transition has slower kinetics, which reduces the recombination rate compared to the direct transition. As can be seen from Figure 7, anatase exhibits an indirect transition, while rutile exhibits a direct transition. Thus, the type of transition also contributes to the enhanced photocatalytic activity exhibited by anatase (Luttrell *et al.*, 2015).

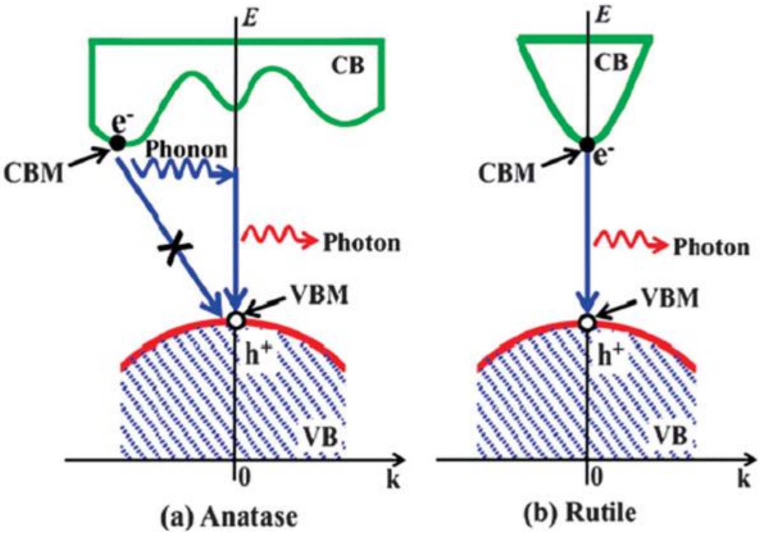

Figure 7: Recombination process of electron (e^-) / hole (h^+) pairs via indirect transition in anatase and direct transition in rutile (Zhang *et al.*, 2014).

2.1.2.
TiO_2-based heterostructures

Despite the advantages presented by TiO_2 as a photocatalyst, neat TiO_2 presents some shortfalls that limit its photocatalytic performance. The main shortfalls reported in the literature for neat TiO_2 are a high rate of recombination of photogenerated charge carriers and low sensitivity to visible light (Kisch e Macyk, 2002; Luo e Lee, 2021).

Consequently, over time, there has been a strong effort by the scientific community to obtain materials that maintain the benefits of titania but also make progress in overcoming the reported shortfalls. Among the proposed results are the aliovalent doping of TiO_2 with metallic or non-metallic ions and TiO_2-based heterostructures (Basavarajappa *et al.*, 2020; Li *et al.*, 2015).

The doping process creates additional energy levels within the E_g of TiO_2. The additional levels contribute to increased sensitivity to visible light - as it reduces the energy required for electronic transitions - and to the reduction of the recombination rate - since these levels can act as trap states for electrons or holes (Figure 8) (Basavarajappa *et al.*, 2020; Kohtani, Kawashima e Miyabe, 2017; Valentin, Di *et al.*, 2007; Zaleska, 2008).

Figure 8 schematically demonstrates potential changes in the E_g of pure TiO_2 (a) through doping. Depending on the element used in doping, there may be the formation of bands of donor (b) and acceptor (c) levels, bands of deep energy levels (d), or the creation of discrete energy levels (e) (Nah, Paramasivam e Schmuki, 2010).

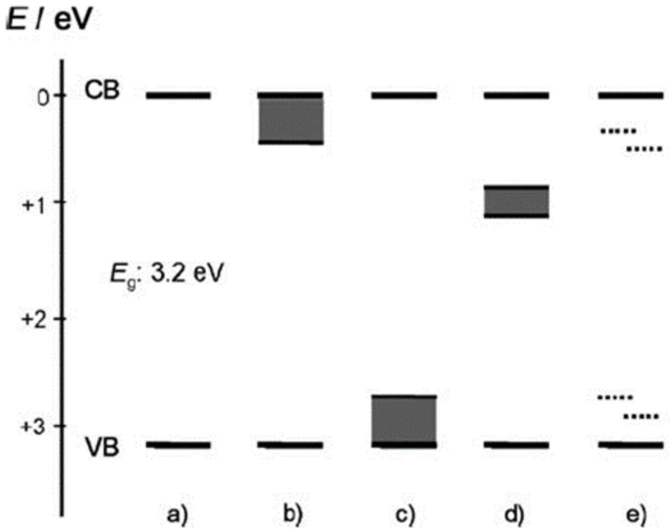

Figure 8: Schematic representations of modifications in the E_g of pure TiO_2 (a), producing donor (b) and acceptor (c) electron level bands, deep levels band (d), and discrete energy levels (e) through doping processes (Nah, Paramasivam e Schmuki, 2010).

In Figure 9, it is possible to observe a specific example, where the sensitization of TiO_2 to visible light is represented through doping with nitrogen.

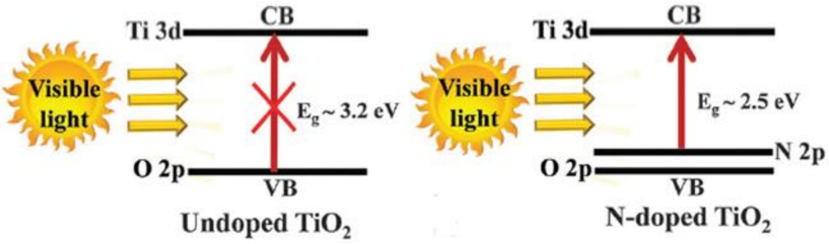

Figure 9: Schematic representation of TiO_2 visible sensitization through N doping (Ansari *et al.*, 2016).

Another proposed solution to improve the photocatalytic performance of TiO_2 is the obtaining of heterostructures based on it. One type of heterostructure widely reported in the literature consists of the junction of different materials that, when combined through interface sharing, exhibit better photocatalytic performance than each phase separately. This type of heterostructure is classified in the literature as a heterojunction. Heterojunctions of TiO_2 combined with metals - also called Schottky junctions -, with other semiconductors, with organic materials such as dyes or carbon-based materials and allotropes thereof, are commonly reported in the literature. Such materials, through different mechanisms, enhance the photocatalytic performance of TiO_2 (Lettieri *et al.*, 2021; Low *et al.*, 2017; Martins *et al.*, 2018).

As an example, Figure 10 illustrates two sensitization mechanisms in the visible range of heterojunctions formed by semiconductor/metal (A) and semiconductor/dye (B).

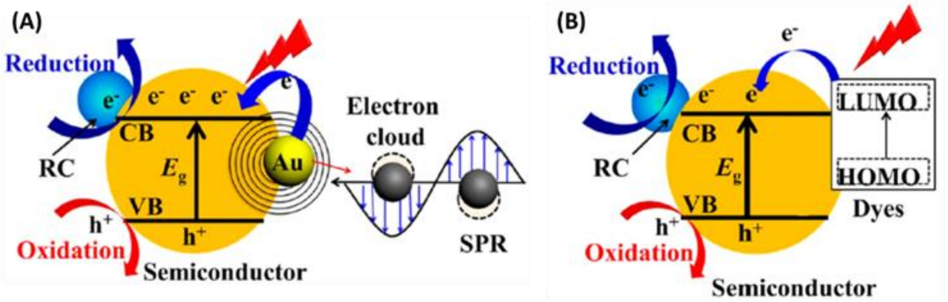

Figure 10: Schematic representation of visible sensitization of a semiconductor/metal heterojunction (A) and semiconductor/dye (B) (Li, X. *et al.*, 2019).

When in nanometric dimensions, some metals, such as gold, subjected to light incidence, exhibit the phenomenon of surface plasmon resonance (SPR). In SPR, surface plasmons resonate with the electric component of the incident electromagnetic wave. For gold and some other metals SPR occurs for wavelengths within the visible spectrum. When coupled at the interface with a semiconductor, such as TiO_2, through excitation in SPR, electrons from these metals can be injected into the semiconductor's conduction band and participate in reduction reactions (Figure 10 - A).

In the case of some organic compounds, such as dyes, light incidence promotes the excitation of electrons from the Highest Occupied Molecular Orbital (HOMO) to the Lowest Unoccupied Molecular Orbital (LUMO). Through charge transfer processes, these electrons originating from the LUMO of the organic compound can be transported to the semiconductor's conduction band. For this transfer to occur, the semiconductor's conduction band must have a reduction potential lower than the LUMO of the organic molecule. (Figure 10 - B).

Another emerging possibility is the use of p-type semiconductor oxides, which can form a p-n heterojunction with TiO_2, which is an n-type semiconductor. In this case, when the interfacial contact between the two materials is established, electrons, the excess charge carriers on the n-side, migrate to the p-side, while the excess electronic holes on the p-side migrate to the n-side of the interface. This process continues until the Fermi level equilibrium is reached for the system composed of the two materials. This migration and accumulation of charges near the interface lead to the formation of a depletion zone, also called a built-in electric field. When this heterojunction is irradiated, the photo-generated charge carriers tend to be attracted to different sides of the junction; electrons (e^-) towards the n-side and electronic holes (h^+) towards the p-side. All these described phenomena are illustrated in Figure 11. This phenomenon provides excellent charge separation, leading to a significant decrease in the recombination rate (Low *et al.*, 2017).

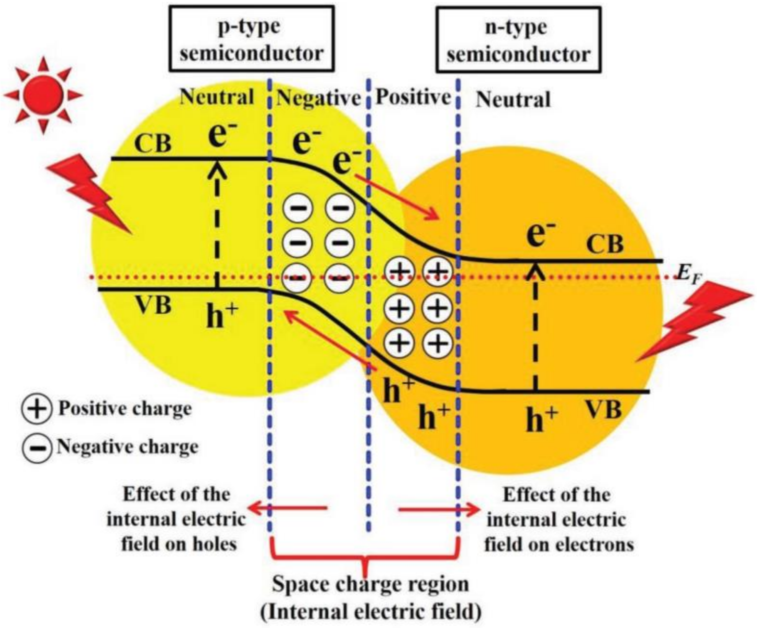

Figure 11: Illustrative diagram of the formation of a p-n heterojunction and the migration of photo-generated charge carriers under the influence of the generated electric field (Low *et al.*, 2017).

In this regard, copper(I) oxide, Cu_2O, stands out as a material with excellent photocatalytic properties, as well as being relatively low-cost, abundant, and non-toxic. With a band gap of 2.1 eV, Cu_2O, is capable of absorbing photons in the visible region of the solar spectrum (Janczarek e Kowalska, 2017). However, the use of pure Cu_2O is challenging due to its poor photo-stability. Considering that Cu_2O is a p-type semiconductor, its combination in heterostructures with TiO_2 to form a p-n junction can increase its stability and, consequently, its photocatalytic activity. In fact, Xing *et al.*, (Xing *et al.*, 2021a) reported a hydrothermal approach for obtaining a Cu_2O/TiO_2 heterojunction for H_2 photoproduction. Through UV-

Vis spectroscopy techniques and Mott-Schottky (M-S) measurements, the authors demonstrated the formation of the p-n junction, which provided the material with light absorption in the visible range and favored the decrease in the recombination rate, and ultimately catalytic activity in H_2 photoproduction.

2.2.

Mechanochemical synthesis as a green route to prepare heterostructured nanomaterials as efficient photocatalysts

The international union of pure and applied chemistry (IUPAC) defines mechanochemical synthesis as a type of chemical reaction induced by the direct action of mechanical energy (Eaborn, 1988). According to the literature, synthesis *via* ball milling (BM) involves a type of mechanochemical reaction. This technique can be defined as a powder processing method that entails deformation, fracturing, and cold welding of particles due to repeated collisions with a ball during the milling process (Fig. 12), which leads to chemical reactions occurring (Danielis *et al.*, 2023; Sopicka-Lizer, 2010).

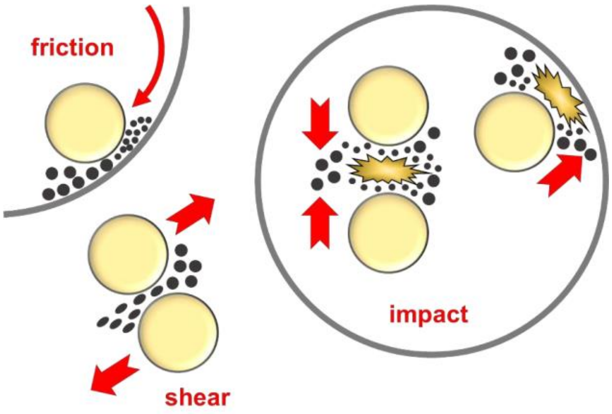

Figure 12: Schematic representation of the mechanochemical synthesis via ball milling and the main forces involved in this process (Danielis *et al.*, 2023).

Since ancient times, humans have employed mechanochemistry. One example of such usage was the friction of mineral materials to generate sparks for obtaining fire. Currently, mechanochemical synthesis has been the subject of growing interest in the context of nanomaterial synthesis. The reasons for such interest are based on the advantages presented by this synthetic approach. Among its main benefits, we can mention the operational simplicity, easy scalability, and the possibility of eliminating the use of solvents, which are often toxic to humans and to the environment. Furthermore, in the vast majority of cases, BM synthesis does not generate waste and, consequently, pollution after the process. For these reasons, it has been identified as one of the greenest synthesis approaches for heterostructured catalysts. In addition to these environmentally and economically significant issues, BM has been reported as an efficient method for the synthesis of highly active single-atom catalysts (SACs) (Hu *et al.*, 2023). Additionally, there is the possibility of controlling crystallite size and defect formation through the manipulation of simple variables such as milling time, ball-to-powder ratio (BPR), and frequency, grinding media, among others (Danielis *et al.*, 2023; Oliveira, De *et al.*, 2020; Zhang *et al.*, 2024). Due to these characteristics and advantages, the IUPAC recently classified mechanochemical synthesis as one of the ten innovations, in the context of chemistry, with the potential to change the world (Boldyrev e Tkáčová, 2000; Gomollón-Bel, 2020; James *et al.*, 2012; Tsuzuki, 2021).

Notwithstanding the advantages mentioned above for the BM method, chemical methods such as sol-gel, hydrothermal, and wetness impregnation remain more commonly used for the synthesis of heterostructures analogous to those discussed in section 2.1.2 (Pasquale *et al.*, 2020; Qiu *et al.*, 2012).

Chen *et al.* (Chen *et al.*, 2020a) recently reported the synthesis of an Au/TiO_2 heterojunction obtained via ball milling (BM). The results illustrate the potential application of mechanochemical synthesis by BM for obtaining TiO_2-based heterojunctions as photocatalysts with enhanced efficiency. The authors compared the photocatalytic activity of samples obtained by wet impregnation (IWI), designated Au/P90-IWI, and by BM, designated Au/P90-BM. Commercial TiO_2 P90 and gold acetate (III) were used as raw materials to obtain the samples.

The BM method proved to be simple, direct, and environmentally friendly, avoiding the use of solvent and subsequent treatments. As demonstrated, the material obtained by BM showed considerably higher photocatalytic activity than that obtained by IWI and dramatically improved the pure P90 catalytic activity. As can be observed in Figure 13, the Au/P90-BM sample exhibits a significantly higher current density (Fig. 13a) and H_2 generation rate (Fig. 13b) compared to the Au/P90-IWI sample. The observed behavior of the Au/P90-BM sample was ascribed to its higher surface area (98.2 $m^2.g^{-1}$) compared to that of the Au/P90-IWI sample (89.3 $m^2.g^{-1}$), alongside a smaller average size and more uniform distribution of metallic gold clusters on the TiO_2 surface.

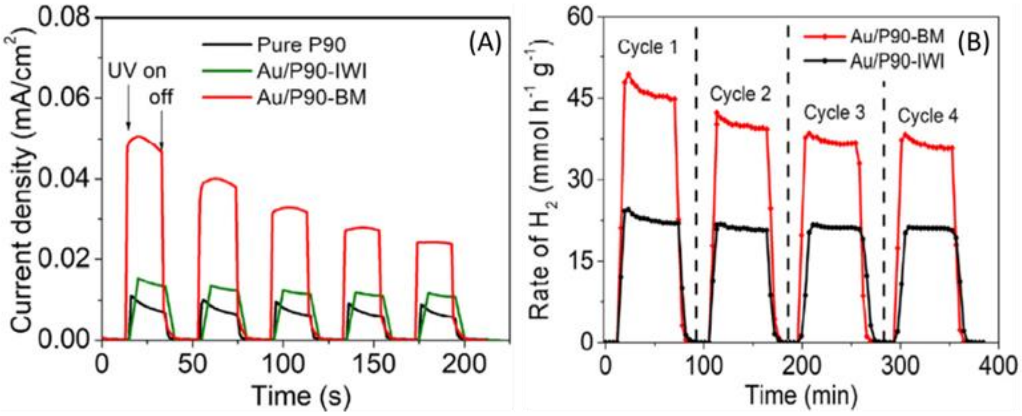

Figure 13: Transient photocurrent response (A) and H_2 photoproduction (B) for the Au/TiO_2 heterojunctions (Chen *et al.*, 2020a).

More recently, Chen *et al.*, (Hu *et al.*, 2023) reported a Pd/TiO_2 heterostructure which, due to the unique interaction between the metal and the support provided by mechanochemical synthesis, resulted in a more active Pd/TiO_2 catalyst for H_2 photoproduction compared to other reference catalysts with the same composition. In this study, it was found that the friction and impacts involved in the BM process, which leads to high local temperature, result in the decomposition of the precursor, palladium acetate (II), leading the generated Pd clusters to be immediately anchored on the TiO_2 support. Responsible for this outstanding performance, in addition to this unique architecture obtained by BM, was the high and homogeneous dispersion of these Pd species on the TiO_2 support. Furthermore, a higher fraction of metallic Pd, which was found to be responsible for favoring H_2 photoproduction due to a more effective charge transfer at the interface, was observed in the sample obtained by ball milling.

2.3.
Facet-dependent photocatalytic properties and tailored architectures

Since photocatalysis is a surface phenomenon, characteristics such as exposed facets and atomic arrangements on the material's surface play a pivotal role in the catalytic performance of the material. Facet engineering has proven to be a versatile method for adjusting photocatalytic properties and can completely modify the electronic and optical properties of the same phase/material. For example, by adjusting exposed facets, it is possible to provide an increase in the lifetime of photogenerated charge carriers, *i.e.*, a reduction in the recombination rate, an increase in the efficiency of visible light absorption, and adjustment of adsorption properties based on the reaction of interest. Some possibilities of properties adjustment through facet engineering are schematically illustrated in Figure 14. Therefore, facet engineering in tailored crystals has been the subject of numerous studies and is of growing interest in the field of materials engineering toward energy conversion and environmental remediation. The commonly used methods for synthesizing materials with controlled facets are mainly hydrothermal approaches, synthetic routes using templates, and by selective corrosion (Bai *et al.*, 2017; Cheng, Zhao e Sun, 2022; Tu *et al.*, 2020).

Figure 14: illustrative scheme of some of the main factors influenced by facet engineering in photocatalysts (Tu *et al.*, 2020).

Chen *et al.* (Chen *et al.*, 2023) demonstrated both experimentally and by first-principles studies how the {001} and {101} facets of TiO_2 (anatase) used as supports for Pt, Pd, and Au clusters influence the reactivity and stability of Me/TiO_2-001 and Me/TiO_2-101 heterostructures (where Me = Pt, Pd, or Au) obtained through a mechanochemical approach via BM. It was found that the different facets of TiO_2 induce distinct oxidation states and consequently exert a strong influence on the reactivity of the heterostructure. The best performance was achieved by the Pt/TiO_2-101 material, which showed by far the highest rate of H_2 photoproduction. This result was attributed to the fact that the {101} facet induced the formation of a significantly higher amount of the Pt^0 species, which is the most active, compared to the amount of this same species formed when the {001} facet of TiO_2 was used as a support (52.44% vs. 34.89%). Furthermore, due to the higher interaction energy observed between the metal clusters and the TiO_2 support, in all cases, the {001} facet provided more stability than the {101} facet. These results shed light on the importance of the role that facet engineering can play in the design of efficient photocatalysts.

3.
Objectives

3.1
General objective

Development of heterostructures formed between TiO_2 and two other abundant oxides, such as NiO and Cu_2O, for obtaining efficient catalysts for the photocatalytic production of hydrogen and removal of an antibiotic (tetracycline) under visible light irradiation.

3.2
Specific objectives

- Synthesize nanometric heterostructures containing TiO_2 *via* simple, direct, potentially scalable, and non-intensive in energy approaches, such as ball milling and soft chemistry;
- Thorough characterization of the obtained materials to understand the phenomena causing different physicochemical properties of the prepared heterostructures;
- Assess the feasibility of the mechanochemical approach *via* ball milling for the preparation of a TiO_2-based heterostructure without the use of noble metal for visible light-driven H_2 production;
- Evaluate the Cu_2O/TiO_2 heterojunction with controlled Cu_2O facets for photocatalytic degradation and adsorption of tetracycline (TC), and investigate the effects of a low-index facet on charge transfer and efficient generation of reactive oxygen species (ROS).

4.
Mechanochemical approach towards optimized Ni^{2+} spin configuration in NiO/TiO_2 heterojunction with enhanced solar-driven H_2 photoproduction

Emanuel do Couto-Pessanha, Victor Magno Paiva, Thiago J. A. Mori, Lluís Soler, Beatriz Canabarro, Paula Jardim, Eliane D'Elia, Jordi Llorca, Bojan A. Marinkovic

The results presented in chapter 4 are under review in the International Journal of Hydrogen Energy (Elsevier) - HE-S-24-03869.

4.1
Background

The increasing global energy demand must be addressed by clean energy due to the depletion of fossil fuels and, principally, owing to environmental and climate concerns (Höök e Tang, 2013). Given this concern, it is important to account that the current annual energy needs of the whole of humanity consist of only a narrow fraction of the solar energy that reaches the Earth's surface annually (Hisatomi, Kubota e Domen, 2014; Kabir *et al.*, 2018; Wen *et al.*, 2017). Therefore, any effort aimed at developing or enhancing methods to harness a greater amount of this abundant free energy is highly desirable.

In this regard, green hydrogen is frequently highlighted as the most eco-friendly fuel. This is attributed to its high heat content and the fact that its combustion generates energy with water vapor as the sole by-product (Dutta, 2021; Kim *et al.*, 2021; Spek, van der *et al.*, 2022; Toit, Du, Avdeenkov e Bessarabov, 2018). Indeed, hydrogen has the highest energy content per mass among the commonly used gaseous, liquid, and solid fuels. For example, hydrogen has approximately three times more energy per kilogram than diesel and gasoline, and 4.7 times more energy per kilogram than ethanol and coal (Armaroli e Balzani, 2011; Sarker *et al.*, 2023).

Since the seminal work by Fujishima and Honda (Fujishima e Honda, 1972) on the feasibility of H_2 and O_2 evolution through photocatalytic water splitting, heterogeneous photocatalysis is mentioned as a promising and profitable path to produce green H_2 (Chen *et al.*, 2020a, 2022; Colón, 2016; Xing *et al.*, 2021a). Since then, TiO_2 emerged as the most important semiconductor for photocatalytic purposes because of its high photo-chemical stability, broad applicability, low cost, and non-toxicity (Almeida *et al.*, 2020, 2022a; Fujishima, Zhang e Tryk, 2008; Gil-Londoño, Krambrock, *et al.*, 2023; Navidpour *et al.*, 2023; Pessanha *et al.*, 2023). However, the usage of neat TiO_2 as a photocatalyst is hindered by its low quantum efficiency which arises from both the high recombination rate and the low visible light sensitivity (Kisch e Macyk, 2002). One of the most effective and cheap strategies to overcome these drawbacks and boost the photocatalytic performance is to combine the TiO_2, an n-type oxide, with a suitable visible light sensitive p-type oxide leading to a p-n heterojunction formation, providing charge separation and increased visible light sensitivity (Brito, de *et al.*, 2018; Hou *et al.*, 2016; Villamayor *et al.*, 2023; Zeng *et al.*, 2021a; Zhang *et al.*, 2021).

NiO is a p-type semiconductor and has the potential to form a p-n heterojunction with TiO_2, providing charge carrier separation and boosting solar light harvesting. In fact, in the field of photocatalysis, the combination of nickel oxide (NiO) and titanium dioxide (TiO_2) in heterostructured composites has attracted a lot of interest. The beneficial synergies that arise from mixing NiO and TiO_2, utilizing the distinct features of both materials, have been clarified by numerous investigations (Faisal *et al.*, 2018; Hou *et al.*, 2016; Jasim, Azeez Dakhil e Abdullah, 2020; Sun *et al.*, 2016). For instance, NiO nanoparticles can be anchored to TiO_2, improving the processes of charge separation and transfer, therefore, boosting the H_2 evolution (Mannaa *et al.*, 2021; Yoo, Kalanur e Seo, 2019; Yu *et al.*, 2021; Zheng *et al.*, 2021).

Very recently, Eisapour *et al.* (Eisapour *et al.*, 2023) reported a p-n heterojunction made of NiO supported on TiO_2 (anatase) nanosheets with improved photocatalytic efficiency for H_2 photoproduction driven by solar light. Firstly, they employed a hydrothermal route to obtain the TiO_2 nanosheets. Hereafter, the researchers loaded the NiO into the nanosheets by impregnating it using a nickel acetate solution. Furthermore, Liu *et al.* (Liu *et al.*, 2018b) reported a p-n heterojunction composed of black NiO_x supported on TiO_2 nanorods, which serves as an efficient photocatalyst. The supported NiO_x displays plenty of defects that enhance sunlight harvesting, favor charge carrier migration, and reduce the recombination rate.

Despite the good activity shown by these NiO/TiO_2 heterojunctions, the used synthetic protocols are not entirely environmentally benign, as they involve the use of hazardous chemicals, high temperatures, high pressures (*i.e.*, extensive energy use), and complex synthesis pathways. As such, aiming for a minimal environmental impact and scalability, the mechanochemical approach is probably the most appealing route to prepare efficient photocatalysts (Braga *et al.*, 2023; Danielis *et al.*, 2018; Fazlikeshteli, Vendrell e Llorca, 2023a; Moores, 2018; Oliveira, De *et al.*, 2020). This cutting-edge strategy not only overcomes the environmental drawbacks of conventional synthetic approaches but also paves the way for precise control over outstanding heterostructured materials by new reaction routes (Danielis *et al.*, 2023; Tsuzuki, 2021).

Finally, as the authors are aware, a bottom-up mechanochemical approach has not yet been employed to prepare NiO/TiO_2 p-n heterojunction. Therefore, this study aims to i) report a green protocol, employing mechanochemistry, for preparation of a NiO/TiO_2 p-n heterojunction; ii) evaluate the feasibility of NiO supported on TiO_2 to boost H_2 photoproduction using a solar light simulator as the light source; iii) accomplish a thorough characterization of the as-obtained photocatalysts; iv) demonstrate that a one-step ball-mill (BM) approach allows for the synthesis of highly efficient TiO_2-based noble metal-free photocatalysts for H_2 photoproduction.

4.2.
Experimental

4.2.1.
Mechanochemical synthesis of NiO/TiO_2 photocatalysts

All the chemicals and reagents were of analytical grade and were used without further treatment.

For typical NiO/TiO_2 sample preparation, a stainless-steel vessel (10 mL) and a stainless-steel ball (16.6 g weight) were used. Furthermore, a proper amount of nickel (II) acetate tetrahydrate ($Ni(OCOCH_3)_2{\cdot}4H_2O$, Sigma-Aldrich, purity $\geq$ 98%) and commercial TiO_2 P90 (Evonik®) were added directly into the vessel without any solvents addition. The ball milling process was carried out using the FRITSCH® Mini-Mill pulverisette 23.

For an efficient and rational ball milling synthesis, the milling conditions, ball-to-powder ratio (BPR, 12-48), milling time (5-20 min), and vibration frequency

(15–50 Hz), were varied to evaluate the impact of the milling parameters on the hydrogen photoproduction (Fig. 34a). Only one parameter was altered for each experiment, while the rest were held constant. The best parameters found were BPR of 24, milling time of 10 min, and frequency of 15 Hz. Additionally, the nickel content was also varied, and, among the prepared materials with different Ni amounts (0.1, 0.5, 0.75, 1 and 2 wt.% Ni), 0.5 wt.% of Ni yielded the best hydrogen photoproduction rate (Fig. 34b). Then the ball-milled sample with 0.5 wt.% Ni, BPR of 24, 10 min, and 15 Hz was labeled as NiO/P90-BM.

4.2.2.
Synthesis of two reference photocatalysts

The incipient wetness impregnation (IWI) method was used as a benchmark synthesis method for supported catalysts (Danielis *et al.*, 2021) to assess the influence of the BM process on the H_2 photoproduction. For IWI sample preparation, 0.0424 g of nickel (II) acetate tetrahydrate ($Ni(OCOCH_3)_2{\cdot}4H_2O$, Sigma-Aldrich, purity ≥ 98%) was dissolved in absolute ethanol and added dropwise on 2 g of the support, *i.e.*, the TiO_2 P90 (Evonik®) to attain the nominal composition of 0.5 wt.% Ni, which was the one for which the best hydrogen photoproduction rate was found. During the IWI sample preparation, the nickel acetate solution was added dropwise onto the support until reaching the wetting limit. At this point, the material was taken to an oven at 50 °C for drying. Subsequently, homogenization was carried out with a mortar and pestle, and the process was repeated several times until all the solution with the nickel precursor was added to the support. Hereafter, the sample was labeled as NiO/P90-IWI.

In addition, it is well known that the calcination process could improve the contact between the cocatalyst and the support. Therefore, after the milling process, a part of the NiO/P90-BM sample was separated and calcined under a static air atmosphere at 400 ºC for 2 h (*vide infra* § 2.3). Hereafter, the calcined sample was labeled as NiO/P90-BMAC.

4.2.3.
Characterization of NiO/TiO$_2$ photocatalysts

Even though a composition with 0.5% Ni showed the highest photocatalytic activity, the characterization techniques benefited from larger Ni content. Therefore, samples with a 2% Ni content were prepared following the same procedure described in sections 2.1 and 2.2.

X-ray powder diffraction (XRPD) analyses were carried out using a Bruker D8 Discover diffractometer, with Cu K_α radiation (λ = 1.5418 Å). The analyses were performed at room temperature using 40 mA and 40 kV, over the 2θ range between 20° and 80°, with a step size of 0.02°, and a counting time of 2 s/step. Raman spectra were acquired using a confocal Raman spectrometer (Renishaw, inVia Qontor), equipped with a Leica DM2700M microscope, and a laser (λ = 532 nm) used as the excitation source operating at 1 mW cm^{-2}.

Transmission electron microscopy (TEM), scanning transmission electron (STEM), X-Ray energy-dispersive spectroscopy (EDS), and selected area electron diffraction (SAED) were performed to gain more insights into the morphological and structural aspects of the samples. All the TEM analyses were carried out on a Thermo Fisher Scientific TEM, model Talos 200X, operating at 200 kV. For the TEM analyses, a small amount of the sample powder was ultrasonically dispersed in isopropyl alcohol for 30 min and then dropped onto a holey carbon film supported by a copper grid.

N_2 adsorption/desorption was performed at -196 °C using a NOVAtouch LX2 (Quantachrome) to determine the textural properties. The specific surface area was calculated from adsorption isotherms by the Brunauer-Emmett-Teller (BET) approach, whereas the mesoporous volume was determined from desorption isotherms by the Barrett-Joyner-Halenda (BJH) method, considering cylindrical pore model.

X-ray photoelectron spectroscopy (XPS) was performed in a SPECS system equipped with an X-ray source (XR-50) operating at 150 W and a PHOIBOS 150 MCD-9 detector. The binding energy (BE) was calibrated using the C 1s signal peak of adventitious carbon at 284.8 eV as the reference value. The raw data were processed using the CasaXPS® software and a Shirley background type subtraction was used to fit all spectra.

We employed X-ray absorption spectroscopy (XAS) to probe the local atomic structure and electronic properties of as-prepared samples. To optimize our investigation, we employed a soft X-ray source, focusing on Nickel (Ni) and Titanium (Ti) L-edge transitions. These transitions have longer core-hole lifetimes compared to K-edge transitions, resulting in narrower inherent linewidths and more distinct spectral features. Consequently, we gathered spectral data for Ni and Ti at the L-edge. XAS at the Ti edge provides valuable insights into the crystal field's symmetry, facilitating the determination of TiO_2 structure and Ti valence. Concurrently, measurements at the Ni L-edge, combined with XPS data, aided in determining the Ni oxidation state. This comprehensive approach allowed us to gain deeper insights into both the nickel oxidation state and its chemical environment. The measurements were conducted at the IPE beamline, located at the Brazilian Synchrotron Light Laboratory.

Diffuse reflectance spectroscopy (DRS) was performed to acquire the absorbance spectra using a Lambda 650 UV/Vis spectrophotometer (Perkin-Elmer, Waltham, MA, USA), assuming spectralon® as blank reference. Hereafter, the DRS data were used as input for the Kubelka-Mulk function to estimate band-gap energies by fitting the linear portion of Tauc plots of $[F(R)h\nu]^{1/2}$ *vs*. energy.

Thermogravimetric analysis (TGA) and Fourier transform infrared spectroscopy (FTIR) were performed to probe residues of the precursor salt, nickel (II) acetate, in the prepared materials. The FTIR spectra were collected using a Perkin-Elmer Frontier spectrometer in the range of 400 cm^{-1} to 4000 cm^{-1}, with a resolution of 4 cm^{-1} and 8 scans. TGA was carried out using a Perkin-Elmer Simultaneous Thermal Analyzer (STA) 6000 under a synthetic air flow of 20 mL min^{-1}, with a heating rate of 10 ºC min^{-1} over a temperature range of 25 - 900 ºC.

4.2.4.
Photoelectrochemical measurements

The Electrochemical Impedance Spectroscopy (EIS), Mott-Schottky (M-S), and Transient Photocurrent techniques were used for the photoelectrochemical measurements. For conducting EIS, M-S, and Transient Photocurrent studies, a conventional 3-electrode electrochemical cell system has been employed, with tests conducted using the Potentiostat/Galvanostat (PGSTAT204, Metrohm) with a quartz cell. The working electrode utilized was a glassy carbon electrode (GCE) with an effective surface area of 0.096 cm², while the reference electrode and counter electrode were Ag/AgCl (3 M KCl) and platinum wire electrodes, respectively.

The EIS tests covered a frequency spectrum ranging from 1 MHz down to 10 mHz, utilizing a 10 mV amplitude relative to the open circuit potential (OCP). For M-S measurements, a 10 mV amplitude was maintained within a potential window spanning from -1 to 1 V *vs* Ag/AgCl, while the frequency remained fixed at 1 kHz. Both the EIS and M-S experiments were conducted without and under UV radiation. In addition, Transient Photocurrent responses were obtained at a fixed bias potential of 10 mV (vs. OCP), under cyclic exposure to UV light (365 nm), employing manual on-off intervals of 20 s.

In all tests, Na_2SO_4 0.5 M (pH = 7) was used as supporting electrolyte. The preparation of the electrodes for the electrochemical studies was carried out following the following procedure: first, the electrode was polished with alumina powder suspension (0.30 µm), followed by sonication in 0.5 mol L^{-1} of H_2SO_4 for 10 min. Then 10 mg of each material was added to a mixture of 1 mL of methanol, 0.1 mL of 5% Nafion, and 1.4 mL of distilled water, the suspension was placed in ultrasound for 1 h and after this time an aliquot of 5 µL was applied to the surface of the GCE and allowed to dry at room temperature.

The M-S equation (Eq. 1) enabled us to derive the band flat potential (V_{fb}) and electron carrier density (N_D), allowing the determination the effective density of states (N_C) (Eq. 2).

Equation 1: Mott–Schottky equation

$$\frac{1}{C^2} = \frac{2}{N_D \varepsilon \varepsilon_0 e}\left(V - V_{fb} - \frac{kT}{e}\right)$$

Equation 2: Effective Density of States

$$N_C = 2\left(\frac{2\pi m_{de} kT}{h^2}\right)^{\frac{3}{2}}$$

where C is the space-charge capacitance, N_D represents the electron carrier density, ε (55 for TiO_2) and ε_0 (8.85×10^{-12} F m^{-1}) are the relative permittivity and vacuum permittivity of the semiconductor, respectively, e (1.6×10^{-19} C) is the elementary charge, V is the applied potential, V_{fb} is the flat band potential, k (1.38×10^{-23} m^2 kg s^{-2} K^{-1} or 8.62×10^{-5} eV K^{-1}) is the Boltzmann constant, T is the absolute temperature, h is Planck constant (6.63×10^{-34} m² kg s^{-1}), and m_{de} is the density-of-state effective mass for electrons of TiO_2 (9.1×10^{-30} kg) (Chen *et al.*, 2020a, 2022; Lee *et al.*, 2023).

4.2.5.
Photoelectrochemical measurements

For the H_2 photoproduction tests, 26 mg of the photocatalysts were ultrasonically dispersed in absolute ethanol and dripped onto a circular cellulose filter paper (from Albet, thickness 0.18 mm, pore size 35-40 µm, 80 g m^{-2} and a total impregnated area of 11.94 cm^2). After that, the paper containing the photocatalyst was dried in an oven at 50 °C. Hereafter, the paper containing the photocatalyst was positioned in a tubular glass photoreactor and then the photoreactor was properly sealed. The tests were carried out at room temperature and at atmospheric pressure. The photoreactor's input was a mixture of argon, used as the carrier gas, water, and ethanol (water:ethanol = 9:1 molar). The argon was bubbled inside the saturator containing the water/ethanol mixture to attain a 20 ml.min^{-1} in continuous flow. The gas products were monitored online using a gas chromatograph (Agilent, Micro-GC 490) in the time intervals of 4 min. The H_2 photoproduction test apparatus was well-detailed in a previous work (Chen *et al.*, 2022). In the current work, a spotlight source of solar light simulator (Hamamatsu Photonics K.K., model L9588-06A) was used as the light source, with a measured irradiance of 60 ± 0.5 mW cm^{-2}. The light-to-hydrogen ratio (LTH) was calculated by the following Eq. (3):

Equation 3: Light-to-hydrogen ratio (LTH) equation

$$\eta_{LTH}(\%) = \frac{\left(n_{H_2}.\Delta G.100\right)}{(S.P)} \tag{3}$$

Where n_{H_2} is the hydrogen produced (mmol s^{-1}), ΔG is the Gibbs Free energy of the water formation (237 kJ mol^{-1}), S is the irradiated area in the photoreactor (cm^2) and P is the light irradiance (W cm^{-2}) (Jiang *et al.*, 2017).

4.3.
Results and discussion

4.3.1.
Characterization of NiO/TiO_2 photocatalysts

Figure 15 displays the as-prepared samples' experimental XRPD patterns and Raman spectra. The diffraction lines were attributed to the TiO_2-anatase (PDF-2: 21-1272) and TiO_2-rutile (PDF-2: 21-1276) in the case of NiO/P90-BM and NiO/P90-IWI samples. On the other hand, for the NiO/P90-BMAC sample, in addition to the same diffraction lines observed for the TiO_2-anatase and TiO_2-rutile phases, it is possible to identify the emergence of the main, the most intense, diffraction line (200) of the NiO (PDF-2: 89-7130) situated at 2θ of 43.4°.

The absence of the main diffraction line from the NiO phase in NiO/P90-BM and NiO/P90-IWI samples may indicate that in these samples NiO appears as clusters (< 2 nm), highly dispersed, making their detection difficult due to the significant broadening of the peak and the overlap with background (Chen *et al.*, 2020a; Ge *et al.*, 2023; Holder e Schaak, 2019). Besides, as it was shown, after air calcination the main diffraction line of the NiO emerged in the pattern. Therefore, given the heat treatment, the NiO clusters evolved into NiO nanoparticles after the air calcination, reducing, consequently, their surface free energy.

Raman spectra (Fig. 15b) exhibited only the typical Raman-active vibrational modes for the anatase phase (Chen e Mao, 2007; Dörr *et al.*, 2018). The peaks at 143.2 cm^{-1}, 195.8 cm^{-1}, and 637.4 cm^{-1} are ascribed to E_g modes, which originate from the symmetric stretching of Ti-O bonds (Taudul, Tielens e Calatayud, 2023). Moreover, the peak at 395.7 cm^{-1} is ascribed to B_{1g} mode, and the band at 515.8 cm^{-1} combines A_{1g} + B_{1g} modes. The B_{1g} modes are the symmetric O-Ti-O bond bending, whereas the A_{1g} mode derives from the antisymmetric O-Ti-O bond bending vibrations (Taudul, Tielens e Calatayud, 2023). The absence of rutile peaks is owing to its poor scattering efficiency (Chen *et al.*, 2020a). Furthermore, neither peak shifting nor peak broadening was observed, which indicates that both Ni addition and the ball milling process do not affect the bulk TiO_2 (the support) crystal lattice (Chen *et al.*, 2022).

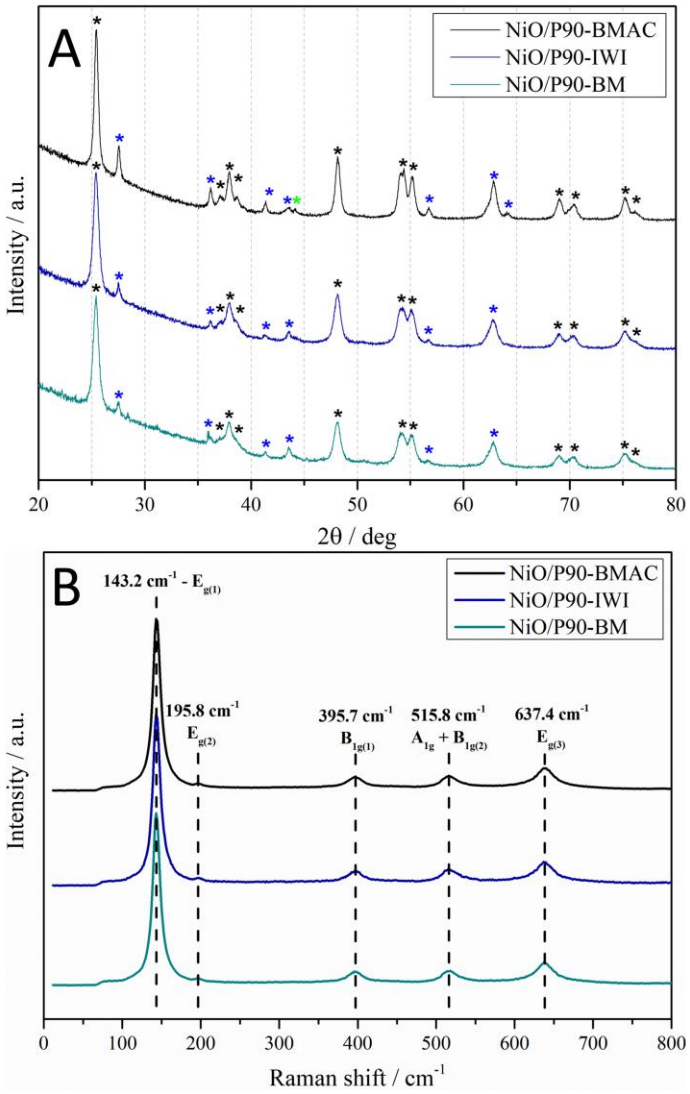

Figure 15: (A) XRPD patterns of (a) NiO/P90-BM, (b) NiO/P90-IWI, and (c) NiO/P90-BMAC samples. The black, blue, and green * stand for TiO_2 (anatase), TiO_2 (rutile), and NiO, respectively. (B) Raman spectra of (a) NiO/P90-BM, (b) NiO/P90-IWI, and (c) NiO/P90-BMAC samples attributed to anatase.

TEM, SAED, and EDS were carried out to probe the samples' morphology and the distribution of NiO species on the TiO_2 (P90) support. Figure 16 shows representative regions of the NiO/P90-BM sample, from which the SAED pattern was also obtained. The SAED pattern (see inset) exhibited a typical polycrystalline aspect (Ferreira *et al.*, 2023). Furthermore, all rings from the SAED patterns were assigned to anatase. In fact, given the XRPD data, such a result could be expected since SAED is unable to distinguish ultrasmall crystalline regions. Specifically, as the particle size decreases, its rings become diffuse, making it difficult to distinguish the nanocrystallites by SAED support (Vázquez-López et al., 202(Li, Zhang e Han, 2023). The lack of diffraction rings from NiO suggests, again, that an excellent dispersion of these NiO clusters on the TiO_2 support has been achieved for NiO/P90-BM and NiO/P90-IWI samples (Fazlikeshteli, Vendrell e Llorca, 2023b). However, after calcination, the NiO species underwent coarsening, causing the NiO clusters to evolve into easily distinguishable NiO nanoparticles (Fig. 35).

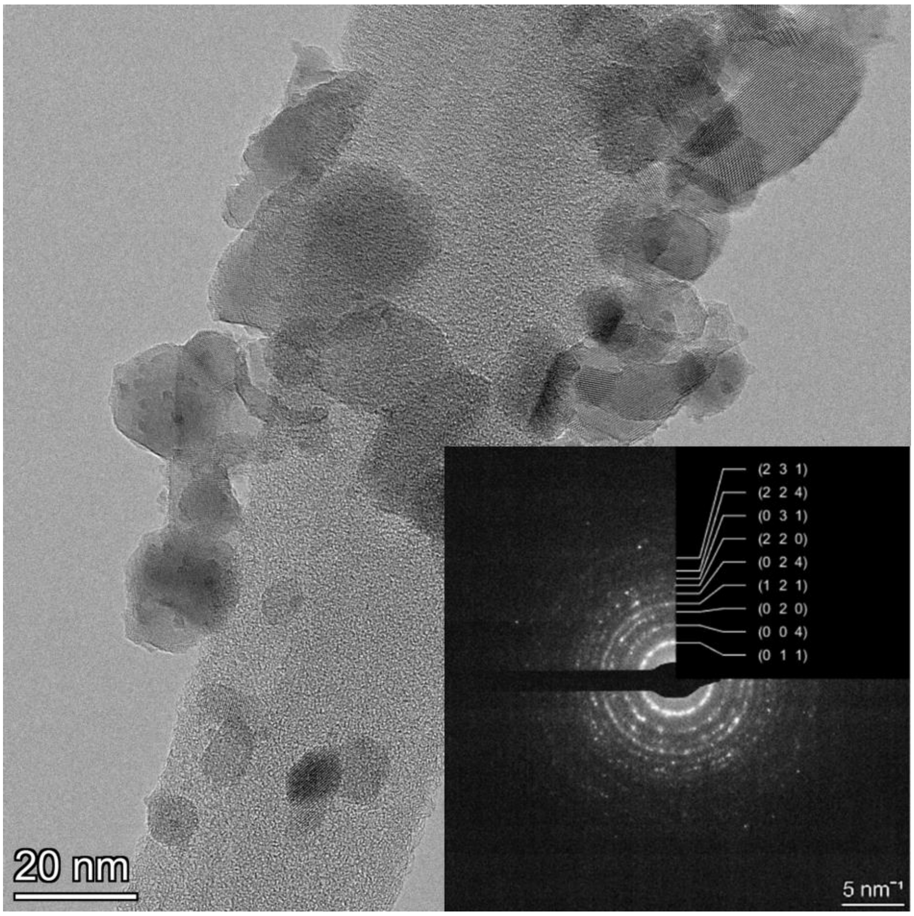

Figure 16: TEM image of NiO/P90-BM and inset of the SAED patterns of NiO/P90-BM sample. The indexed rings in the SAED pattern belong to anatase.

The STEM-EDS elemental mapping of NiO/P90-BM (Fig. 17a) and NiO/P90-IWI (Fig. 17b) showed well-distributed NiO clusters on the top of the TiO_2 (P90) particles. The selected areas in Figure 17a-c show that the Ni content in the selected areas (small yellow squares) is higher than over the total area of the photomicrographs (see Table 4 and EDS spectra in Fig. 36). These findings show that NiO forms well-dispersed clusters in both the NiO/P90-BM and NiO/P90-IWI samples and nanoparticles (< 10 nm) in the NiO/P90-BMAC sample (Fig. 35). These apparently coalesced NiO nanoparticles in the NiO/P90-BMAC sample suggest that the dispersion attained by the BM process was not preserved after calcination. Finally, it is noteworthy, that Ni elemental maps for the NiO/P90-BM and NiO/P90-IWI samples showed that the Ni content over large areas is very close to the nominal value (2%) (Table S1), which corroborates homogeneous dispersion of NiO on the TiO_2 support and the precise control of the composition provided by BM and IWI methods. However, the BMAC sample showed a value that deviates significantly from the nominal one (Table S1), which again suggests that the dispersion of NiO species attained by the BM process was lost after calcination.

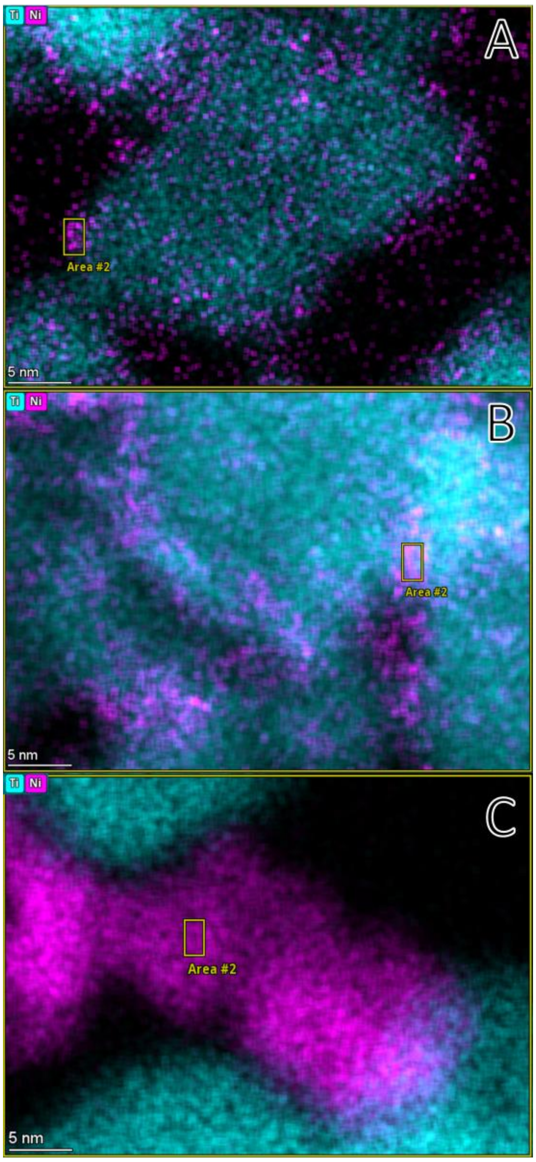

Figure 17: STEM-EDS elemental mapping of Ti and Ni for the (a) NiO/P90-BM, (b) NiO/P90-IWI, and (c) NiO/P90-BMAC samples.

The N_2 adsorption/desorption analysis was carried out to probe the textural properties of the synthesized samples and neat P90. Following the IUPAC classification, the type IVa isotherm was identified for the N_2 adsorption/desorption curves of all samples (Fig. 37). The type IVa isotherm is characteristic of mesoporous materials, having pore sizes ranging from 2 to 50 nm (Habran, Pontón, *et al.*, 2018; Sangwichien e Aranovich, 2002; Thommes *et al.*, 2015). Both the obtained surface areas (S) calculated by the Brunauer-Emmett-Teller (BET) method and the obtained volumes of mesopores (V_{meso}) calculated by the Barrett-Joyner-Halenda (BJH) method are summarized in Table 1.

Table 1: Specific surface areas (S) calculated BET approach and mesopores volumes (V_{meso}) determined by BJH method for Neat P90 (Fig. 37a), NiO/P90-BM (Fig. 37b), NiO/P90-IWI (Fig. 37c), and NiO/P90-BMAC (Fig. 37d) samples.

Sample	**S (BET) m^2 g^{-1}**	**V_{meso} (BJH) cm^3 g^{-1}**
Neat P90	94.5	0.36
NiO/P90-BM	93.3	0.35
NiO/P90-IWI	82.7	0.91
NiO/P90-BMAC	48.4	0.25

The materials' surface composition was investigated using XPS analysis. The presence of the key elements, *i.e.*, nickel, titanium, oxygen, and carbon, was confirmed by the XPS survey scan (Fig. 38). An additional thorough study of the high-resolution XPS spectra of Ni 2p, Ti 2p, O 1s and C 1s provided valuable insights into the chemical bonding environments and the metal-support interactions (Fig. 18a-c).

In all cases, the XPS spectra revealed a strong satellite component in the Ni $2p_{3/2}$ region (see Fig. 18c), confirming the presence of NiO species in all three samples (Lucentini, Casanovas e Llorca, 2019). Specifically, the peak at approximately 862 eV was attributed to the Ni^{2+} $2p_{3/2}$ shakeup satellite peak, characteristic for NiO (Kitchamsetti *et al.*, 2021). The Ni $2p_{3/2}$ main peak, observed in all three samples, was assigned to Ni^{2+} species within NiO (Wang *et al.*, 2015; Yen *et al.*, 2015). However, notable distinctions emerged when comparing the XPS spectra of the NiO/P90-BM, NiO/P90-IWI, and NiO/P90-BMAC samples. In the NiO/P90-BM and NiO/P90-IWI samples, the Ni $2p_{3/2}$ main peaks at 856.3 eV and 856.5 eV, respectively, strongly indicated the prevalence of NiO clusters with Ni^{2+} species, which was in line with STEM-EDS analyses (Fig. 17) and suggested a stronger metal-support interaction in these samples (Italiano *et al.*, 2020; Lan, Pang e Ge, 2021; Liu *et al.*, 2013). Furthermore, it is worth noting that the Ni $2p_{3/2}$ main peak in the BM sample is broader than that in the IWI sample (FWHM of 2.69 *vs*. 2.51), suggesting that the strongest NiO-TiO_2 interaction was attained in the NiO/P90-BM sample (Li *et al.*, 2017).

Curiously, after calcination (NiO/P90-BMAC), the Ni $2p_{3/2}$ main peak shifted to a slightly lower BE and an additional strong peak emerged at 853.6 eV. Firstly, the observed peak shift of the Ni $2p_{3/2}$ main peak towards slightly lower (from 856.3 to 856.1 eV comparing BM and BMAC sample) binding energy (BE) can be attributed to a subtle alteration in the chemical environment of the Ni^{2+} species within the NiO nanoparticles in the BMAC sample. Therefore, the signal of the Ni $2p_{3/2}$ main peak at 856.1 eV for NiO/P90-BMAC is also associated with the highly dispersed NiO clusters on TiO_2, *i.e.*, non-coalesced species of NiO with a high metal-support interaction (Italiano *et al.*, 2020). On the other hand, we supposed that the emergence of an additional peak at ~ 853 eV for the NiO/P90-BMAC sample was related to the photoelectron signal originating from the nanoparticles that have evolved from the NiO clusters, these ones being the dominant species before the calcination (Italiano *et al.*, 2020). In fact, as illustrated by Mossanek *et al.* (Mossanek *et al.*, 2011) through both experimental data and theoretical calculations employing cluster models, the surface contribution, which is represented by pyramidal NiO_5 clusters, results in one prominent Ni $2p_{3/2}$ main peak at 855.8 eV for NiO. This closely aligns with our results for the BM and IWI samples, as well as with the first Ni $2p_{3/2}$ main peak in the BMAC sample. Otherwise, the 'bulk' contribution at 853.6 eV, characterized by octahedral NiO_6 clusters, leads to the shift of the Ni $2p_{3/2}$ main line to a lower binding energy. Recently, the Ni $2p_{3/2}$ main peak at 853.7 eV for the signal originated from Ni^{2+} in a NiO_6 coordination due to the ‘bulk’ contribution was reported (Ding *et al.*, 2022). This is in line with the findings (Fig. 18c) of the new peak originated after calcination in NiO/P90-BMAC sample.

Therefore, we ascribe the difference between the Ni $2p_{3/2}$ main peaks presented in BM and IWI samples with the Ni $2p_{3/2}$ main peaks from BMAC sample to the dominant contribution of the NiO clusters in BM and IWI samples. Meanwhile, NiO nanoparticles originated after calcination in the BMAC sample generate a significant ‘bulk’ contribution to the Ni $2p_{3/2}$ spectrum located at 853.6 eV (Mossanek *et al.*, 2011; Preda *et al.*, 2012).

For all three samples, the Ti 2p spectra (Fig. 18a) exhibit peaks at binding energies of ~ 464 eV and ~ 458 eV, which are ascribed to the Ti $2p_{1/2}$ and Ti $2p_{3/2}$ signals, respectively (Chen *et al.*, 2020a, 2022). These signals correspond to Ti^{4+}-O bonding environments in conventional TiO_2, confirming that Ti occurs only as Ti^{4+} species in octahedral coordination. Moreover, the energy difference (ΔBE) between BE(Ti $2p_{1/2}$) and BE(Ti $2p_{3/2}$) is 5.7 eV, which is typical for Ti^{4+}-O bonds in the anatase polymorph (Gil-Londoño, Cremona, *et al.*, 2023). The O 1s signal (Fig. 18b), in all cases, corresponds to lattice oxygen in conventional TiO_2 (Chen *et al.*, 2022).

Finally, it is well known that defects on the material's surface can induce shifts in binding energy or the emergence of new XPS peaks (*e.g.*, oxygen vacancy and Ti^{3+}, respectively). Therefore, the analysis of the Ti 2p signal (Fig. 18a) revealed that such defects were not generated in TiO_2 neither due to the addition of NiO nor owing to the ball milling process. These findings of XPS analyses are consistent with the Raman spectroscopy, corroborating that the TiO_2 support did not develop defective sites.

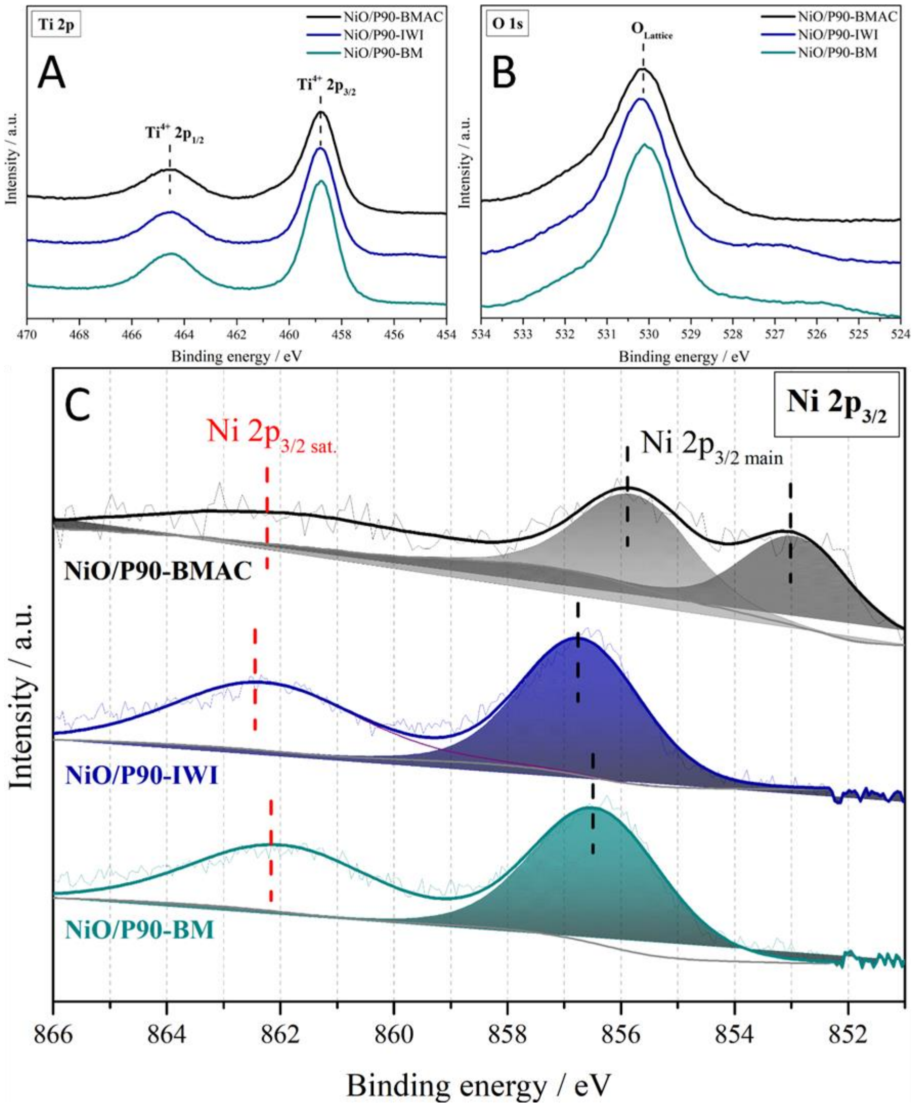

Figure 18: High resolution XPS spectra within (a) Ti 2p, (b) O 1s, and (c) Ni $2p_{3/2}$ regions of NiO/P90-BM, NiO/P90-IWI, and NiO/P90-BMAC samples.

To gain more insights into the local coordination environments of Ni onto the TiO_2 support, XAS measurements at Ni L-edge, Ti L-edge, and O K-edge were carried out. Such a study can unveil the spin state of nickel ions, based on Ni L-edge spectrum, and in addition, the oxidation state. The measurements were performed using both total electron yield (TEY) and fluorescence yield (FY) acquisition modes. Since relevant differences between the spectra acquired by TEY and FY were not identified (Fig. 19) only data obtained by FY were analyzed.

In all cases, both Ti L-edge (Fig. 19a) and O K-edge (Fig. 19b) spectra correspond to those previously reported for anatase, which is the dominant TiO_2 polymorph in the P90 support 2(Deng *et al.*, 2015; Kronawitter *et al.*, 2012; Kucheyev *et al.*, 2004; Laan, Van Der, 1990; Li *et al.*, 1994; Ruus *et al.*, 1997;

Vázquez-López *et al.*, 2022; Wang, T. T. *et al.*, 2017; Wang *et al.*, 2020; Zeng *et al.*, 2021b). The pre-edge peaks at the Ti L-edge spectra, labeled as A’ and A” in Fig. 19a, are associated with $2p^6\ 3d^0 \rightarrow 2p^5\ 3d^1$ transitions in Ti^{4+} species in octahedral coordination (Kronawitter *et al.*, 2012). In turn, the most intense peaks, labeled as A, B_1, B_2, C, and D, are related to inter-shell transitions of core electrons from occupied states (Ti 2p) to unoccupied states (Ti 3d) (Vázquez-López *et al.*, 2022). Due to the spin-orbit coupling that splits the 2p orbital into $2p_{3/2}$ and $2p_{1/2}$, the absorption L-edge presents two regions, *i.e.* the L_3 (A, B_1, and B(Ruus *et al.*, 1997; Vázquez-López *et al.*, 2022). Besides, the crystal field, generated by the oxygen atoms forming octahedral coordination around Ti^{4+}, breaks the degeneracy of the 3d valence states of Ti^{4+}, leading to the split of 3d into e_g ($d_{x^2-y^2}$ and d_{z^2} orbitals - represented by the peaks B_1, B_2, and D) and t_{2g} states (d_{xy}, d_{xz}, and d_{yz} orbitals - represented by the peaks A and C) (Deng *et al.*, 2015; Ruus *et al.*, 1997; Wang *et al.*, 2020). It is worth noting that the e_g orbitals ($d_{x^2-y^2}$ and d_{z^2}) point directly towards the 2p orbitals of the ligand atoms (oxygens) located at the vertices of the TiO_6 octahedra (Kronawitter *et al.*, 2012; Kucheyev *et al.*, 2004; Wang, T. T. *et al.*, 2017). Therefore, the bands related to the e_g states (B_1, B_2, and D) are highly sensitive to the symmetry and cation environment. The three most common polymorphs of TiO_2 (anatase, rutile, and brookite) exhibit TiO_6 octahedra with different levels of distortion (Li *et al.*, 1994). Thus, a clear distinction between those can be made by analyzing the e_g region of the Ti L-edge signal (Kucheyev *et al.*, 2004). A stronger signal of B_1 with respect to B_2, as observed in all our samples, is the well-known fingerprint of the anatase polymorph (Ruus *et al.*, 1997; Vázquez-López *et al.*, 2022).

Regarding the O K-edge spectra, it is possible to observe two distinct regions. Firstly, two intense peaks (E and F in Fig. 19b) are observed from ~530 to 536 eV. These two peaks originate from transitions from the occupied O 1s orbitals to the hybridized O 2p-Ti 3d unoccupied states (t_{2g}, peak labeled as E, and e_g, peak labeled as F) (Kronawitter *et al.*, 2012; Kucheyev *et al.*, 2004; Ruus *et al.*, 1997; Vázquez-López *et al.*, 2022). In turn, the high-energy bands (above ~536 eV and labeled as G, H, and I) originate from transitions involving the band formed by O 2p and hybridized Ti 4sp orbitals (Kucheyev *et al.*, 2004; Vázquez-López *et al.*, 2022). The O K-edge spectrum is highly sensitive to the environment of oxygen atoms. Thus, the absence of peak shifts and broadening in the samples containing NiO, compared to the neat P90 reference, allows to state that no defects have been generated due to the ball milling process and the deposition of NiO on the TiO_2 support (Vázquez-López *et al.*, 2022).

In the case of the Ni spectrum, the L_3 edge is ascribed to the Ni $2p_{3/2} \rightarrow$ Ni 3d-O 2p transition, while the L_2 edge is ascribed to Ni $2p_{1/2} \rightarrow$ Ni 3d-O 2p transition (Lei *et al.*, 2021). The energy and shape of these peaks provide valuable insights into the oxidation state of nickel species, splitting of the ligand field surrounding the nickel ions, and allowing the disclosing of the local atomic environment. In addition, the NiO XAS spectrum can give insights into the spin state of the nickel ions, as the low-spin (LS) and high-spin (HS) configurations result in different spectral signatures (Wang *et al.*, 2000). Understanding the spin state of Ni^{2+} in NiO is primordial since it was proven to influence properties such as catalytic reactivity (Ding *et al.*, 2023; Peng *et al.*, 2022).

As it can be observed in Fig. 19c, the Ni L_3-edge of all samples is around 853 eV, and the L_3 and L_2 regions are split by ~17 eV due to spin-orbit coupling. The overall shape of the experimental spectra is in close agreement with those reported for NiO in the literature (Arenholz, Laan, Van Der e Nolting, 2008; Groot, de *et al.*, 2021; Laan, Van Der *et al.*, [s.d.]). Thus, these data confirm that nickel occurs in the Ni^{2+} state, and in octahedral coordination bounded to six oxygens, giving rise to a NiO_6 octahedra (Groot, de *et al.*, 2021; Laan, Van Der *et al.*, [s.d.]; Wang *et al.*, 2000). Nevertheless, some marked differences can be observed among the samples. The BM and BMAC samples exhibit multiple structure spectra for both L_3 and L_2 edges, with an evident higher energy shoulder in the L_3 region and a double structure in the L_2 region. These shoulder and doublet structures reveal localized states, which are typical for ionic environments, and their positions (at 855.5 eV for the shoulder, and for the doublet at 870,9 eV and 871,8 eV) suggest that the dominant nickel species is high-spin Ni^{2+} (Samarai, Al *et al.*, 2019; Soriano ' *et al.*, 1993; Wang *et al.*, 2000, 2013). On the other hand, the IWI sample has a very smooth shoulder on the L_3 peak and a single unsplit band in the L_2 region. This line shape has previously been demonstrated to correspond to Ni^{2+} presenting a relevant contribution from a low-spin configuration (Wang *et al.*, 2000, 2013). It is worth noting that this modification of the spin state has been shown to have implications, for example, in electron migration and, consequently, in photocatalytic activity (Peng *et al.*, 2022). In addition to charge migration, it was observed that the spin configuration also exerts an influence on surface properties, which in turn are directly linked to catalytic activity (Ding *et al.*, 2023).

To understand the Ni^{2+} spin state, crystal field multiplet calculations have been run to obtain the theoretical spectra for both HS and LS configurations. The details of crystal field multiplet theory have been described in several books and reviews (Groot, 2005; Groot, de e Kotani, 2008). The calculations were performed using the Quanty code (Haverkort, Zwierzycki e Andersen, 2012) to solve Slater integrals and matrix elements of the dipole transition $2p^6\ 3d^8 \rightarrow 2p^5\ 3d^9$. We used an octahedral symmetry O_h (with a D_{4h} distortion in the case of LS state) and the following crystal field parameters: 1) 10Dq = 1.6 eV, Ds = 0.0, Dt = 0.0 eV for the high-spin state; and 2) 10Dq = 4.3 eV, Ds = 0.91 eV, and Dt = 0.47 eV for the low-spin state. To compare with the experimental spectra, the calculated XAS were broadened with a 0.6 eV (FWHM) Lorentzian and 0.4 eV (FWHM) Gaussian functions. The calculated spectra are shown in Fig. 19c together with the experimental ones. The double peak line shape (dashed lines J and L at L_3, M and O at L_2) of the HS configuration strongly resembles the XAS measured for BMAC and BM samples. On the other hand, the LS single peak (dashed lines K at L_3 and N at L_2), placed right in between the features J and L of the HS spectrum, seems to be much more relevant for IWI sample. With these results, it is demonstrated that the Ni^{2+} spin state configuration is strongly dominated by the HS state for BMAC and BM samples. On the other hand, IWI sample has a much more significant contribution of the LS state.

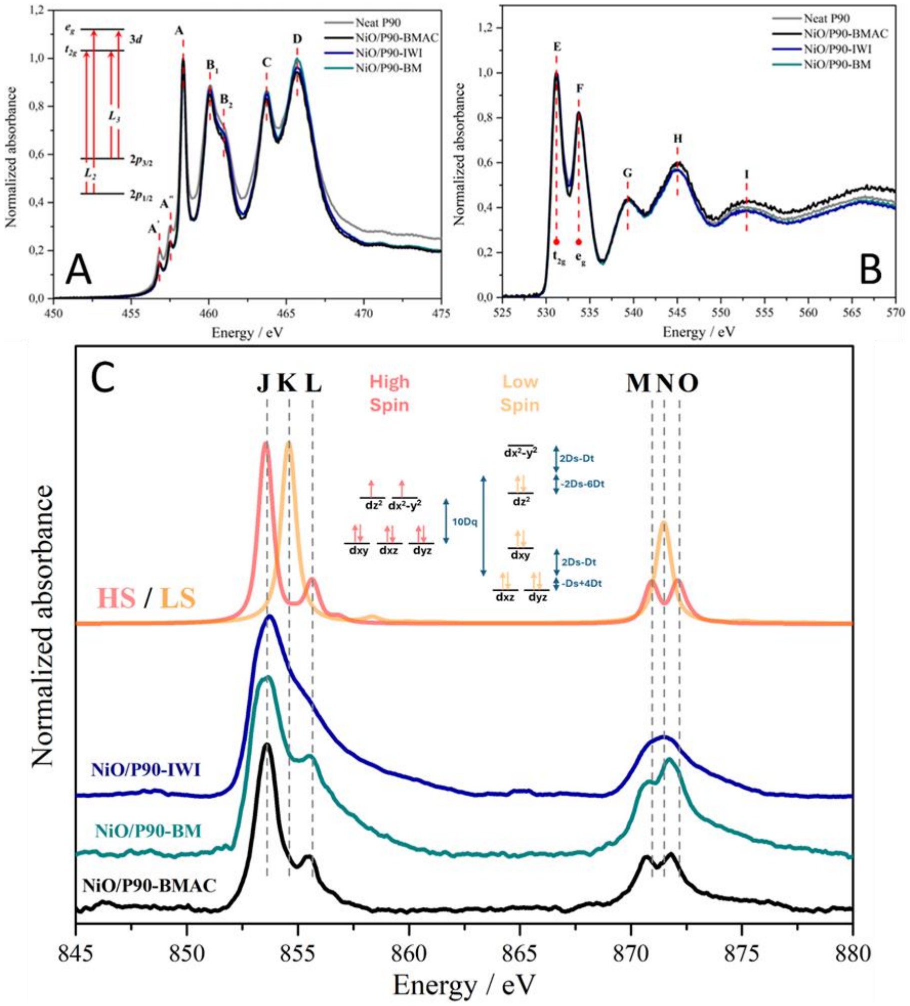

Figure 19: (a) XAS spectra at the Ti L3 and L2 edges of neat P90, NiO/P90-BM, NiO/P90-IWI, and NiO/P90-BMAC samples, with the main peaks labeled and highlighted to assist discussion, along with a representative diagram of the electronic transitions involved. (b) XAS spectra around the O K-edge of the same samples, indicating the transitions involving O orbitals hybridized with the t_{2g} (peak E) and e_g (peak F) states of Ti. (c) Experimental XAS spectra around the Ni L3 and L2 edges of NiO/P90-BM, NiO/P90-IWI, and NiO/P90-BMAC samples, along with the simulated spectra for two different spin states (low and high), including a representation of the electronic configuration of the Ni 3d states for both cases.

The diffuse reflectance spectroscopy was performed in the UV-Vis region to investigate the optical properties and electronic structure of the analyzed samples and the influence of NiO addition on the solar light sensitivity of TiO_2. The absorbance spectra (Fig. 20a) show enhanced visible light harvesting by the samples containing NiO in comparison to Neat P90. For all the samples, the absorption edge in < 400 nm region is ascribed to the support (TiO_2) intrinsic interband excitation. It is possible to notice that no additional light absorption occurs for Neat P90 in wavelengths from 400 to 700 nm, confirming the low sensitivity of TiO_2 to visible light. Otherwise, it was possible to observe, for NiO-containing samples, the regions of increased absorption, confirming that the NiO addition boosted the visible light sensitivity. Notably, two distinct regions of increased absorption compared to Neat P90 are observed for the BM and IWI samples at ~ 420 nm and in the range between ~ 600-800 nm. These regions are associated with the $^3A_{2g}(F) \rightarrow {}^3T_{1g}(P)$ and $^3A_{2g}(F) \rightarrow {}^3T_{1g}(F)$ transitions, respectively, of Ni^{2+} species in NiO (Abul-Magd, Morshidy e Abdel-Ghany, 2020; López-Fonseca *et al.*, 2012). Furthermore, the band in the ~ 600-800 nm region has been previously associated with d-d transitions in transition metals due to the breaking of the degeneracy of d orbitals promoted by the ligand field provided by the surrounding oxygen ions (Mannaa *et al.*, 2021; Morgado *et al.*, 2009). On the other hand, higher absorption is observed in the BMAC sample, making these regions more featureless. On this regard, it is well known that cationic vacancy (V_{Ni}'') is the point defect intrinsically present in NiO (Girolamo, Di *et al.*, 2020; Gong *et al.*, 2020). Furthermore, as demonstrated by Egbo *et al.* (Egbo *et al.*, 2020), these defects generate additional electronic levels in the NiO band gap. Therefore, this increased visible light absorption by the BMAC sample may be associated with electronic levels inside the band gap of NiO nanoparticles. Otherwise, the NiO clusters present in the BM and IWI samples would be less defective, thus making different transitions (at ~ 420 nm, and in the range between ~ 600-800 nm) more easily distinguishable. Finally, it is also worth note that these ionic defects (V_{Ni}'') are generally detrimental to the photocatalytic performance of the material (Gil-Londoño *et al.*, 2022), since they consist of deep states that act as recombination centers for photo-generated electrons, reducing the material's catalytic efficiency.

Regarding the Tauc plots a redshift was observed. Specifically, the values of the band gaps were 3.2 eV, 3.1 eV, 3.1 eV, and 2.9 eV for neat P90, NiO/P90-BM, NiO/P90-IWI, and NiO/P90-BMAC samples, respectively. Thus, once again, it is demonstrated that NiO enhanced the harvesting of solar light by TiO_2.

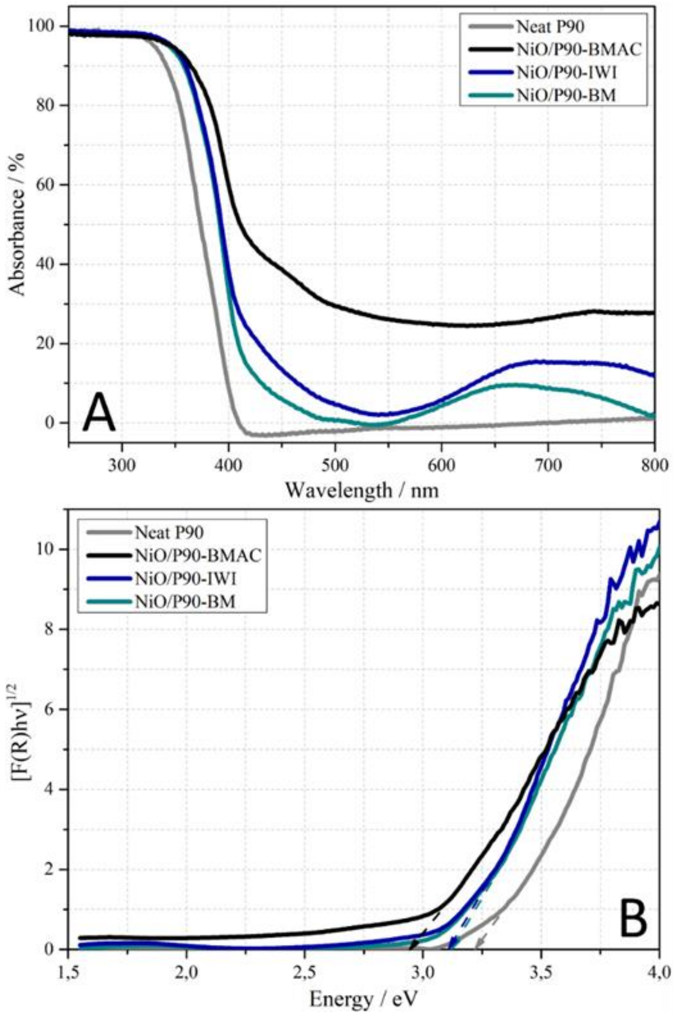

Figure 20: (a) Absorbance spectra and (b) Tauc plots of Neat P90, NiO/P90-BM, NiO/P90-IWI, and NiO/P90-BMAC samples.

The FTIR spectra (Fig. 34c), as well as the thermogravimetric curves (Fig. 34d), revealed the presence of residues from the nickel precursor salt, nickel (II) acetate, in the photocatalysts containing 2 wt.% Ni synthesized by both IWI and BM. A part of the acetate did indeed decompose during the synthesis process, as evidenced by the percentage of mass loss between 300 and 400 ºC, however, another part remained in the samples. Additionally, only two of the characteristic peaks of nickel (II) acetate are distinguished in IR spectra of NiO/P90-BM and NiO/P90-IWI samples, located at ~1531 and ~1419 cm^{-1}, and are attributed to the asymmetric and symmetric stretching of the carboxylate group (COO^{-}) in nickel (II) acetate (Hussein, Nohman e Attyia, 1994). No characteristic peaks for nickel (II) acetate were detected in the BMAC sample, indicating that the calcination eliminated the excess of acetate. Common to all samples containing Ni and Neat P90 is a broad band centered around ~3427 cm^{-1} and a peak at ~1632 cm^{-1}

associated with water molecules (moisture) adsorbed on the surface of the samples. Specifically, these signals are attributed to O-H stretching and O-H-O scissoring bend modes in water molecules, respectively (Mojet, Ebbesen e Lefferts, 2010a). Additionally, the band between 400 and ~900 cm^{-1} originates from the contribution of signals from the TiO_2 support and the NiO formed in the samples containing Ni. Strictly speaking, the Ti-O stretching modes in anatase and Ti-O-Ti bond vibrations appear at 463 cm^{-1} and 730 cm^{-1}, respectively (Pessanha *et al.*, 2023). Additionally, at ~450 cm^{-1} and ~660 cm^{-1}, there are signals originating from the stretching vibrations of Ni-O bonds in NiO (Gondal, Saleh e Drmosh, 2012; Sharma *et al.*, 2021). Therefore, the increase in the intensity of this band between 400 and ~900 cm^{-1} in all samples containing Ni would be related to the formation of NiO.

Furthermore, regarding the best performance, we observed that the 0.5 wt.% of Ni sample yielded the best hydrogen photoproduction rate (Fig. 34b). From this content, as the amount of Ni increases, a decrease in H_2 photoproduction efficiency is observed. We hypothesize that this is due to the well-known shadowing effect (Farcy *et al.*, 2024). Since titania produces electron-hole pairs as the initial step in the photoreaction, there is an ideal Ni loading. A shadowing effect occurs when the loading of Ni precursor is excessive, which prevents titania from absorbing light and, as a result, reduces the creation of electron-hole pairs.

Furthermore, the excess nickel (II) acetate that did not react during synthesis, which increases as the Ni content is increased, would also be detrimental to the catalyst efficiency since acetate is not recognized as a good cocatalyst and can compete with other reactions on the surface of the catalyst, reducing the efficiency for H_2 photoproduction.

4.3.2.
Photoelectrochemical measurements

To understand the effect of modifications on the photoelectrochemical properties of TiO_2 by addition of NiO, EIS, transient photocurrent, and M-S techniques were used. The Nyquist diagram for the studied materials in the presence of UV radiation (Fig. 21a) shows that Neat P90 and the modified materials demonstrate a tendency towards a decrease in the capacitive loop, which is directly linked to the charge transfer resistance (R_{ct}) (Carla de Santana de Lima *et al.*, 2023;

Feliu, 2020; Reséndiz-Ramírez *et al.*, 2022), indicating that the presence of NiO promoted electronic transfer. From the Nyquist diagram (Fig. 21a and Fig. 39a), the R_{ct} was calculated using the equivalent circuit schematically represented in Figure 40. In this circuit, R_s represents the electrolyte resistance, and R and CPE_1 are assigned to the bulk material impedance of the Nafion film on the GCE. R_{ct} and CPE_2 represent the GCE interface's charge transfer resistance and constant phase element (Mazurków, Kusior e Radecka, 2021). The details are compiled in Table 5. The χ^2 value obtained for all fitted circuits was less than 10^{-3} (Table 5).

According to Table 5, the R_{ct} decreases for all materials in the presence of UV light. Among the studied samples, NiO/P90-BM showed the lowest R_{ct} under light, followed by NiO/P90-IWI, NiO/P90-BMAC, and Neat P90. In the absence of light, however, (Fig. 39a), contrary to what was observed in the presence of UV radiation, the presence of NiO did not show a significant improvement in electron transfer, indicating that NiO was more beneficial for the photoelectrochemical properties.

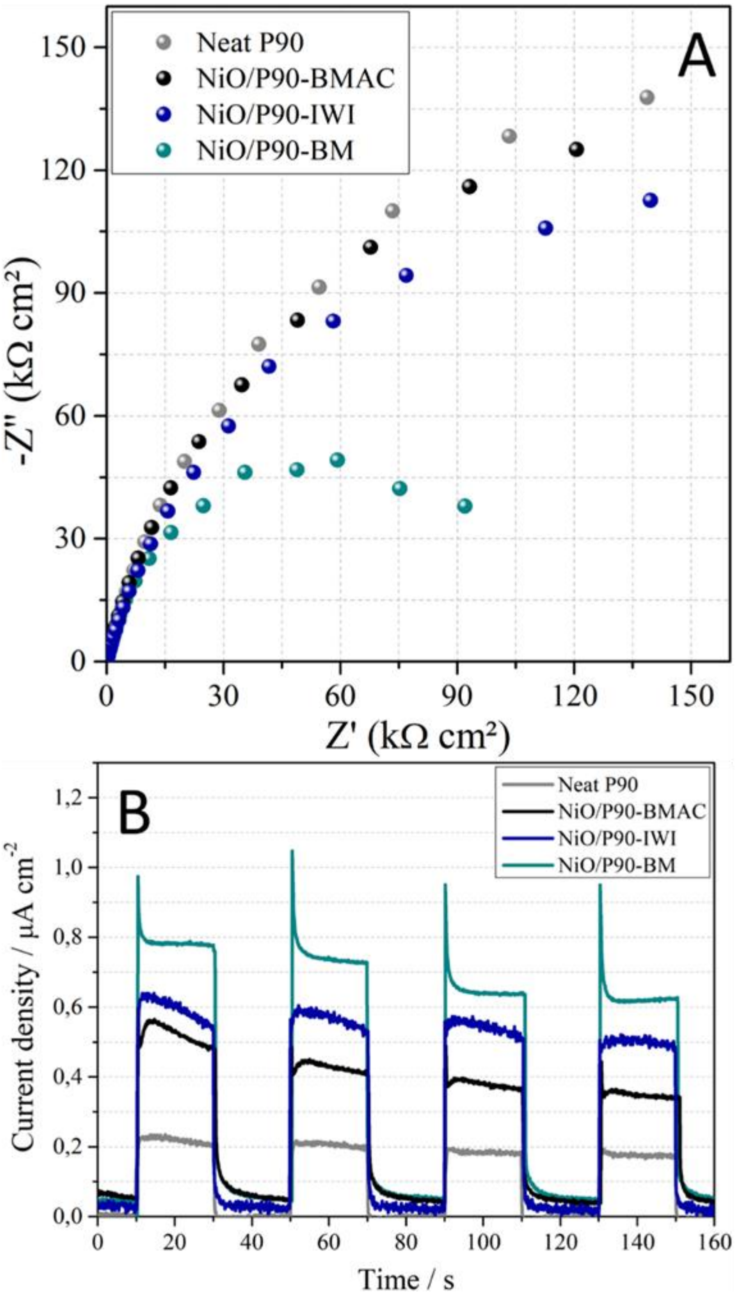

Figure 21: (a) Nyquist diagrams in Na_2SO_4 0.5 mol L^{-1} under UV radiation and (b) Transient photocurrent response in the light on-off processes in Na_2SO_4 0.5 mol L^{-1} of neat P90, NiO/P90-BMAC, NiO/P90-IWI, and NiO/P90-BM samples.

The transient photocurrent (Fig. 21b) reflects what is verified in the Nyquist diagrams (Fig. 21a and Fig. 39a). When subjected to UV radiation, the materials presented a much higher photocurrent than in light absence, with NiO/P90-BM presenting the highest current density. The increase in current density in the samples with NiO indicates that more photogenerated electrons and holes are moving compared to Neat P90, thus showing a reduced recombination rate and resulting in a more photoactive material (Chen *et al.*, 2020a, 2022). Transient photocurrent measurements of NiO/P90-BM and NiO/P90-BMAC samples revealed sharp peaks upon light activation.. These peaks are linked to the discrepancy between the rapid generation of carriers, recombination, and the slow dynamics of the surface reaction (Lian *et al.*, 2020). Another factor contributing to the rise in current density could be the quantity of electrons and/or holes per unit volume of material, which will be assessed utilizing the M-S technique.

The flat band potential (V_{fb}) for all samples was obtained from the extrapolation of the linear region of the M-S plots (Fig. 39b,c) up to the value of $\frac{1}{C^2} = 0$ (Table 2). As it was shown, the addition of NiO onto the TiO_2 support (P90) caused a shift of V_{fb} towards less negative potentials both in the presence or absence of UV radiation. This phenomenon can be explained by the p-n heterojunction formation at the NiO/TiO_2 interface.(Lian *et al.*, 2020).

Table 2: Flat band potential (V_{fb}) and electron carrier density (N_D) calculated for neat P90, NiO/P90-BMAC, NiO/P90-IWI, and NiO/P90-BM samples.

	V_{fb} (V vs Ag/AgCl)		**N_D (cm^{-3}) ($\times 10^{20}$)**	
Sample	**Dark**	**UV**	**Dark**	**UV**
Neat P90	–0.441	–0.393	1.32	1.57
NiO/P90-BM	–0.363	–0.357	1.55	3.80
NiO/P90-BMAC	–0.383	–0.319	1.52	1.65
NiO/P90-IWI	–0.434	–0.386	1.40	2.38

From the angular coefficient of the M-S equation (Eq. 1) the electron carrier density (N_D) was calculated (Table 2), and as can be observed for all materials with NiO addition an increase in $N_{D,}$ both in the absence and mainly in the presence of UV light, was noticed. The increase in N_D followed the same trend both in the presence and absence of UV light, where NiO/P90-BM has the highest electron density, followed by NiO/P90-IWI, and NiO/P90-BMAC. Neat P90 presented the lowest N_D. The findings are consistent with those from both EIS and transient photocurrent analyses, indicating that NiO/P90-BM exhibits superior photoelectrochemical properties. Concerning the conduction band, the addition of NiO consistently shifted the band potential towards less negative values, irrespective of the presence or absence of UV radiation.

For both in the presence and absence of UV light, the N_D value was lower than that of N_c (8.81×10^{20} cm^{-3}), for Neat P90, obtained from Equation 2. Therefore, since $N_D < N_C$, the position of the Fermi level can be considered equal to the V_{fb}.

These results show that the NiO deposition onto Neat P90 was crucial for improving the photoelectrochemical properties of the TiO_2. They brought to light NiO/P90-BM as the best material from both photochemical and electrochemical points of view, presenting the lowest charge transfer resistance, the highest photocurrent signal, and the highest electronic density.

4.3.3.
Photocatalytic H_2 evolution tests

In the previous section (*vide supra* § 3.1), a detailed characterization of theNiO/P90-BMAC, NiO/P90-IWI, and NiO/P90-BM samples was presented. Likewise, a comprehensive discussion of the different characteristics of each sample was conducted to understand their influence on the photocatalytic activity. Specifically, this study investigated the influence of different methods for obtaining NiO supported on TiO_2. Samples were obtained by incipient wetness impregnation (IWI), ball milling (BM), and ball milling followed by air calcination (BMAC).

H_2 photoproduction rates (Fig. 22a) reveal that the preparation methods significantly influence the performance of the NiO/TiO_2 heterojunction. Firstly, it is noticeable that Neat P90 exhibits a negligible H_2 production rate (0.73 mmol h^{-1} g^{-1}) due to the high recombination rate and low sensitivity to the solar light of TiO_2 (Chen *et al.*, 2020a, 2022). On the other hand, the addition of NiO markedly increased the H_2 production rate. Regarding the performance of samples obtained by different methods, the following trend in H_2 photoproduction was observed: NiO/P90-BM (8.85 mmol h^{-1} g^{-1}) > NiO/P90-IWI (6.42 mmol h^{-1} g^{-1}) > NiO/P90-BMAC (3.79 mmol h^{-1} g^{-1}). The obtained η_{LTH} value for the NiO/P90-BM sample was 2,11%, in agreement with some other photocatalytic systems between 1-3% η_{LTH} values (Kim *et al.*, 2019). XAS studies (Fig. 19) demonstrated that the BM sample exhibited a high-spin configuration of Ni^{2+}, which is more favorable for catalytic performance (Ding *et al.*, 2023). The unpaired electrons in a high-spin configuration can migrate more easily, as demonstrated (Ding *et al.*, 2023), and interact more readily with adsorbed molecules at a lower energy cost, boosting the necessary chemical reactions for photocatalysis. For paired electrons, an associated pairing energy is required to leave the orbital and interact with other molecules. On the other hand, the IWI sample showed a significant contribution from the low-spin state with paired electrons, which is less favorable for the material's reactivity during H_2 photoproduction tests.

To summarize physical-chemical properties of the samples with NiO addition, it is showed that the NiO/P90-BM sample presented well-dispersed NiO clusters, maximization of the NiO/TiO_2 interface area which favors photocatalytic activity (Chen *et al.*, 2020a), the most favorable spin state for catalysis applications, the lowest charge transfer resistance, and the most intense photocurrent transient response. These properties together lead to a heterojunction with higher charge separation efficiency and surface reactivity, which are the reasons behind the superior performance of the NiO/P90-BM sample.

Furthermore, we assessed the performance of the NiO/P90-BM sample across multiple cycles (Fig. 22b), long-term tests (Fig. 22c), and in a two-month-old sample (Fig. 22d). Noticeably, the acquired data indicate the potential viability of the NiO/P90-BM sample for practical and large-scale applications. For example, only a slight difference (~ 10%) in H_2 photoproduction rates between the first and last (forth) cycles was observed. As for stability in long-term tests, it can be noted that under irradiation (Fig. 22c) a steady-state H_2 photoproduction was achieved before 24 h. Interestingly, after 2 months of storage under ambient conditions, without any additional care, no observable distinction between the freshly prepared BM sample and the two-month-old sample was found, once again showing that this material has viability for practical and large-scale applications.

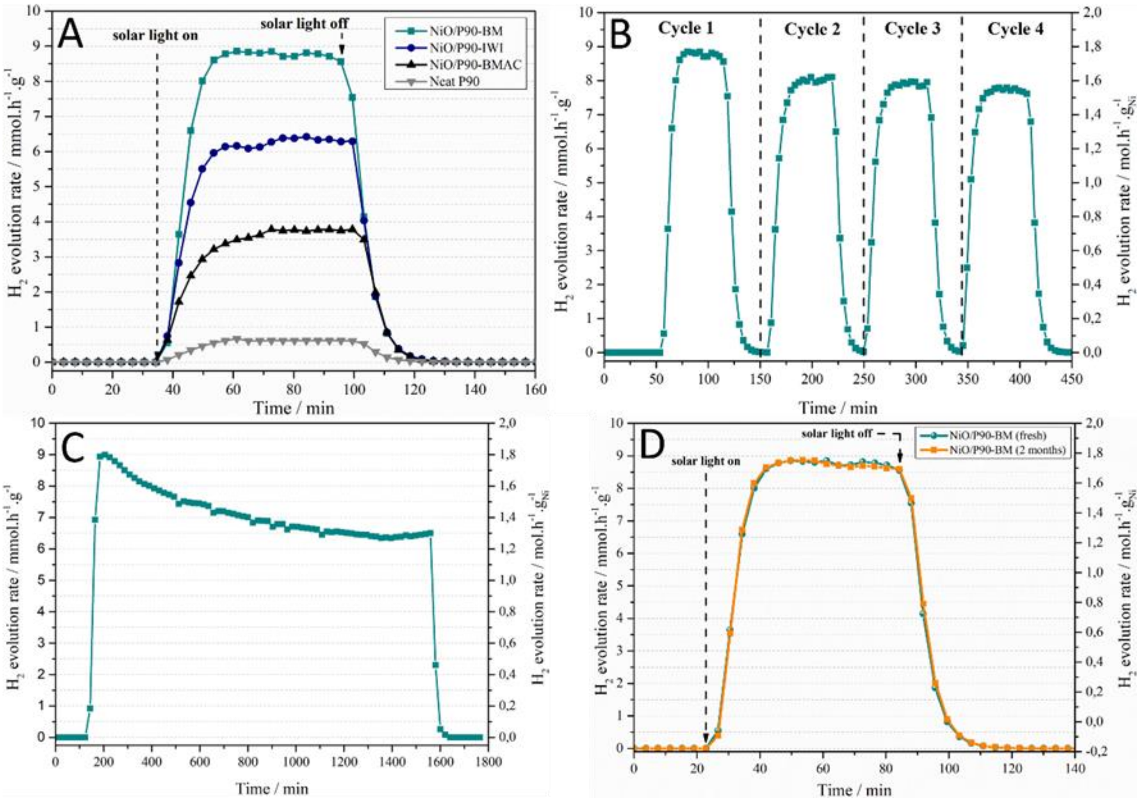

Figure 22: (a) H_2 photoproduction tests of NiO/P90-BM, NiO/P90-IWI, and NiO/P90-BMAC samples, and (b) cycles, (c) long-term, and (d) aging tests of NiO/P90-BM sample.

The photocatalytic mechanism is schematically illustrated in Scheme 1. After interfacial contact, electrons migrate from the n-type TiO_2 to the p-type NiO, driven by the Fermi level difference. In TiO_2, the Fermi level is near the conduction band (CB), while in NiO, it is near the valence band (VB). This electron transfer persists until an equilibrium is reached in the Fermi levels of both materials, leading to the formation of a depletion region named as built-in electric field. This region inhibits further movement of charge carriers across it.

Under irradiation, electron-hole pairs are generated, with electrons being attracted to the positively charged side of the depletion region (TiO_2) and holes accumulating on the negatively charged side (NiO). The accumulated holes then oxidize water and ethanol molecules, releasing H^+ ions. Subsequently, electrons in the conduction band participate in the reduction of H^+ ions to form H_2 molecules.

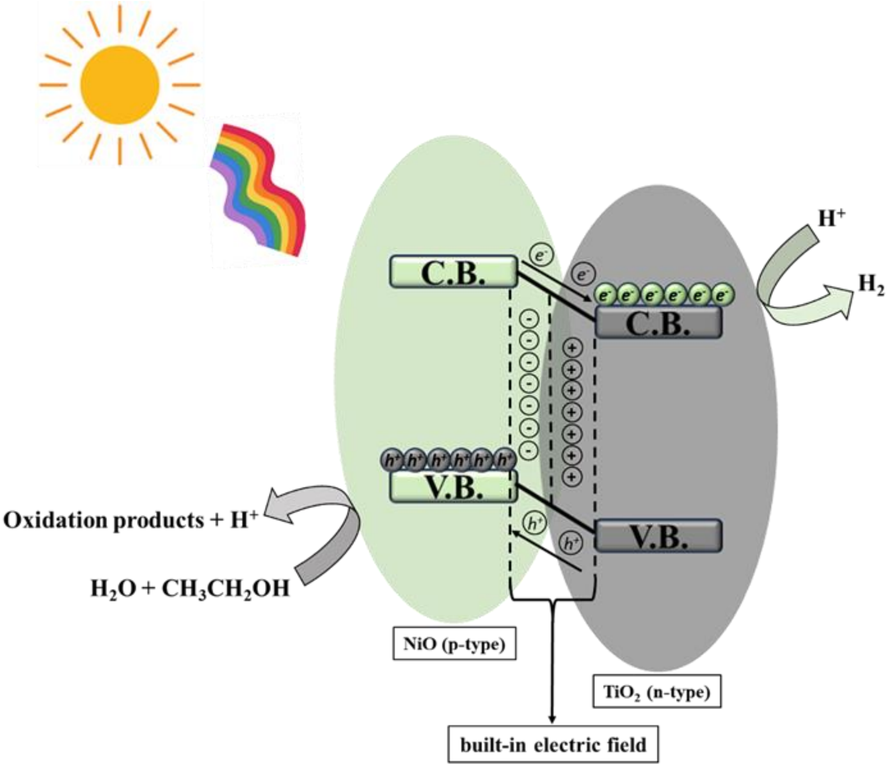

Figure 23: Illustration of H_2 photoproduction mechanism in NiO/TiO_2 p-n heterojunctions. The green and gray balls represent photogenerated electrons and holes, respectively, while the hollow black spheres represent electrons and holes that have migrated upon interfacial contact due to the difference in Fermi levels, forming the built-in electric field.

4.4.
Conclusions

The present work reported a one-step ball milling synthesis towards obtaining a NiO/TiO_2 p-n heterojunction. The BM process proved to be a simple, fast, and environmentally friendly approach that avoids the use of chemicals that can be hazardous to the environment and humans. Meanwhile, the process efficiently achieved a high dispersion of NiO clusters on the TiO_2 support, as revealed by STEM-EDS analysis.

One of the key results, revealed by UV-Vis DRS analysis, is the remarkable enhancement in solar light absorption achieved by incorporating NiO into the TiO_2 support. Thus, the more efficient use of solar energy makes the reported NiO/TiO_2 heterojunction a promising candidate for sunlight-driven H_2 photoproduction. Furthermore, electrochemical impedance spectroscopy and transient photocurrent were used to probe the impedance and charge carrier migration of the prepared samples. Interestingly, the results followed the same trend as those observed in the

H_2 photoproduction rate, showing that the smallest arc radius, directly linked to the lowest charge transfer resistance, was observed for the NiO/P90-BM sample upon incidence of light. Furthermore, the NiO/P90-BM sample exhibited the highest photocurrent response. XAS studies at the Ni L-edge revealed that the preparation method strongly influences the spin configuration of Ni^{2+} in NiO species. The synthesis *via* BM resulted in a dominant high-spin configuration for Ni^{2+} inside NiO species, while the sample obtained by IWI exhibits a more significant contribution from the low spin configuration. This difference markedly influences the photocatalytic activity, as verified in H_2 photoproduction tests.

Consequently, the hydrogen photoproduction rate of NiO/P90-BM (8.85 mmol h^{-1} g^{-1}) was approximately 1.4 times higher than that for NiO/P90-IWI (6.42 mmol h^{-1} g^{-1}) sample, 2.4 times higher than that for NiO/P90-BMAC (3.79 mmol h^{-1} g^{-1}) sample, and 12.2 times higher than that for neat P90 (0.73 mmol h^{-1} g^{-1}) sample. In addition, cycling and long-term stability tests of the NiO/P90-BM photocatalyst demonstrated its stability along different cycles and longtime use (24 h) use and as well as, after long storage times (2 months). This stability reinforces the viability of the NiO/P90-BM photocatalyst for practical and large-scale applications, where consistent and sustained performance is required.

In summary, our findings provide a comprehensive understanding of the mechanochemical synthesis, properties, and performance of the NiO/P90-BM p-n heterojunction for H_2 photoproduction. The reported results seem to represent an important contribution for expanding the knowledge on H_2 photoproduction through efficient, abundant, low-cost, sunlight-sensitive, stable catalysts obtained through direct and easily scalable synthesis routes.

5.
Efficient sunlight-driven photoproduction of superoxide and hydroxyl radicals by mechanochemically synthesized NiO/TiO_2 heterojunction: Insights from EPR/spin trapping

5.1
Background

Heterogeneous photocatalysis is an emerging technology to address environmental issues, such as harmful microorganism inactivation (Matsuura *et al.*, 2021; Nakano *et al.*, 2022), gaseous and liquid pollutants abatement (Almeida *et al.*, 2020; Habran, Krambrock, *et al.*, 2018; Yang *et al.*, 2022) and H_2 production (Chen *et al.*, 2020a, 2022). In this context, TiO_2 is the most widely used material for photocatalytic purposes (Guo *et al.*, 2019; Hashimoto, Irie e Fujishima, 2005; Nunes *et al.*, 2021; Pessanha *et al.*, 2023). Nonetheless, neat TiO_2 photocatalysts exhibit two main shortfalls: the high recombination rate, which limits the quantum efficiency, and the wide band gap, which leads to a low sensitivity to solar radiation (Luo e Lee, 2021; Qutub *et al.*, 2022; Shoneye *et al.*, 2022). One approach to address these shortfalls involves coupling TiO_2 with suitable semiconductors, creating heterostructures with appropriate energy band positions to enhance visible light sensitivity and to promote the separation of photogenerated electrons and holes (Jitan, Al, Palmisano e Garlisi, 2020; Zhao *et al.*, 2024). Particularly, when a p-type semiconductor establishes interfacial contact with TiO_2, which is a n-type semiconductor, a p-n heterojunction will be formed. Due to the Fermi level difference among the two sides of the p-n junction, there is an electron migration from the n-side towards the p-side. Simultaneously, there is a migration of electronic holes from the p-side towards the n-side. Once equilibrium is reached, a depletion zone, also known as a built-in electric field, is formed at the interface between the p-n heterojunction phases. This built-in electric field enhances the separation of photogenerated electron-hole pairs when the p-n heterojunction is irradiated with suitable wavelengths considering the band gap of the formed p-n heterojunction. Due to this enhanced charge separation, the p-n heterojunction generally exhibits better photocatalytic performance compared to the well-known type II heterojunctions (Ruan *et al.*, 2023).

In this regard, NiO/TiO_2 p-n junction systems have attracted considerable interest due to their enhanced properties as photocatalysts. This enhanced performance improvement is associated to significant reduction in the recombination rate of photo-generated electron-hole pairs. Over time, NiO/TiO_2 heterostructures have demonstrated a good capacity to degrade harmful organic compounds in the environment. A literature review of various studies over time reveals advances in the synthesis and performance of these materials.

Yu et al. (2010) (Yu, Wang e Cheng, 2010) explored the synthesis of a NiO/TiO_2 heterostructure with flowerlike morphology, developing a two-step method for their fabrication without the use of templates. They demonstrated that these composite heterojunctions exhibit significantly higher photocatalytic activity for the photocatalytic degradation of an aqueous solution of p-chlorophenol compared to pure TiO_2 and NiO phases prepared under the same experimental conditions. The superior performance of the NiO/TiO_2 heterostructure compared to the pure phases was attributed to several factors. The homogeneous dispersion of TiO_2 nanoparticles in the intermixed nanolayers of NiO flowers favored the light-harvesting process. Additionally, the flowerlike morphology allegedly favored chemical reactions occurring on the material's surface.

Subsequently, Lin et al. (2011) (Lin *et al.*, 2011) investigated the formation of NiO/TiO_2 p-n heterojunctions on TiO_2 nanobelts obtained by a hydrothermal method. Then, NiO nanoparticles were deposited on TiO_2, resulting in heterostructures called NiO-NP/TiO_2 NBs. They observed that these nanojunctions effectively reduce the recombination of electron-hole pairs, leading to the enhancement of the photocatalytic activity of the heterostructure. Also, through acid-assisted treatment, the authors obtained TiO_2 nanobelts with rough surfaces. The coarsened NiO-NP/TiO_2 NBs material demonstrated improved activity compared to the others, achieving 90% degradation of methyl orange (MO) after 40 minutes under UV irradiation.

Chen et al. (2011) (Chen *et al.*, 2011) prepared a series of p-n junction photocatalysts, NiO/TiO_2, by incipient wet impregnation (IWI) with different amounts of NiO. Throughout the study, a significant improvement in photocatalytic activity was demonstrated, ascribed to the inhibition of electron-hole recombination. They proposed a p-n junction mechanism to explain the increased photoactivity and observed that an optimal NiO loading (0.5% wt.%) resulted in the highest degradation efficiency for the degradation of methylene blue (MB) under UV irradiation.

Liu et al. (2018) (Liu *et al.*, 2018a) developed heterojunctions with TiO_2 nanorods (NRs) as support for black NiO nanoparticles with superior efficiency for toluene and MB degradation under simulated solar irradiation. The black color of NiO, resulting from a band gap of 1.42 eV, was obtained by creating defects in its lattice during synthesis. The black NiO/TiO_2 NRs heterojunction showed a degradation rate 7.9 times higher than that of pure TiO_2 NRs. They ascribed this improvement to the effective separation and facilitated transfer of photo-generated charge carriers, along with efficient superoxide ($^{\bullet}O_2^-$) production. Recycling tests demonstrated the good stability of the proposed heterojunction.

More recently, Castaneda et al. (2022) (Castañeda *et al.*, 2022) reported a heterostructure made of fluorinated TiO_2 as support and NiO supported on it via IWI, designated as NiO/TiO_2-F, for the degradation of caffeine under UV irradiation. This heterostructure demonstrated higher efficiency than pure TiO_2, achieving a degradation rate of 88%. Such a result was ascribed to the better separation and transport of charges obtained in the heterostructure. Additionally, the ≡Ti–F species formed on the surface allegedly favored the formation of the hydroxyl ($^{\bullet}OH$) radical, identified as the main responsible for the caffeine photodegradation in this case.

Finally, very recently, Rana and Jeevanandam (2024) (Rana e Jeevanandam, 2024) reported a method for the synthesis of core-shell TiO_2@NiO nanoparticles and evaluated their efficacy in the photocatalytic degradation of rhodamine B (RhB) under solar irradiation. Once again, a dramatic reduction in the recombination rate was ascribed as the main reason behind the improved performance. The TiO_2@NiO-0.5 material exhibited the best performance, degrading 98.3% after 60 minutes, compared to 24.2% and 33.6% for pure NiO and TiO_2, respectively. $^{\bullet}O_2^-$ and $^{\bullet}OH$ radicals were ascribed as responsible for the RhB degradation, as demonstrated through tests using radical scavengers. Using isopropanol (IPA) and p-benzoquinone (BQ) as $^{\bullet}OH$ and $^{\bullet}O_2^-$ scavengers, respectively, a sharp decrease in photocatalytic activity was observed. Strictly speaking, the use of IPA led to a decrease in the RhB degradation rate from 98.3% to 21%, while the use of BQ decreased the degradation rate from 98.3% to 23%.

As demonstrated, advancements in the synthesis and performance of NiO/TiO$_2$ p-n junction materials underscore their promising potential for applications in photocatalysis for environmental remediation endeavors. Notably, the effective generation of reactive oxygen species (ROS) stands out as a crucial aspect influencing the photocatalytic abatement of various pollutants as reported in the literature. Typically, the assessment of ROS production entails the utilization of scavengers. In this study, we investigated the *in-situ* photogeneration of $^{\bullet}O_2^-$ and $^{\bullet}OH$ radicals within the NiO/TiO$_2$ heterostructures, which we recently identified as proficient catalysts for solar-driven hydrogen production [rf]. To our knowledge, this investigation is a pioneering effort examining such phenomena within this specific system. Our findings shed light on the $^{\bullet}O_2^-$ and $^{\bullet}OH$ photogeneration dynamics within these heterostructures and, consequently, offer valuable insights into their potential application across diverse fields and scenarios as highly efficient photocatalytic materials.

5.2.
Experimental

The mechanochemical synthesis was carried out as previously reported (Couto-Pessanha *et al.*, 2024). Typically, 14.5 mg of nickel (II) acetate tetrahydrate ($Ni(OCOCH_3)_2 \cdot 4H_2O$, Sigma-Aldrich, purity ≥ 98%) and 170 mg of P90 were added into a 10 mL stainless-steel vessel. The reagents were ground for 10 min at a frequency of 15 Hz. The sample was named NiO/P90-BM. The BM process was carried out using the FRITSCH® Mini-Mill pulverisette 23. Subsequently, a part of the BM sample was heat treated in static air at 400°C for 2 h, to investigate the effect of calcination on the material's performance. The calcined sample was labeled NiO/P90-BMAC.

To evaluate the efficiency of the synthesis *via* BM in preparing efficient heterostructures towards $^{\bullet}O_2^-$ and $^{\bullet}OH$ generation, a reference sample was also prepared using the incipient wetness impregnation (IWI) method, a benchmark for supported catalysts (Danielis *et al.*, 2021). For the preparation of the sample by IWI, 42.4 mg of nickel acetate was dissolved in absolute ethyl alcohol and kept under magnetic stirring, forming a light green solution. Subsequently, this solution was added dropwise to 500 mg of P90 up to the wetting limit. At this point, the material was placed in an oven at 50°C to dry, and the process was repeated successively until the entire solution was added. Homogenization was carried out using a mortar between drying steps. Finally, the sample was labeled NiO/P90-IWI. The materials obtained *via* BM, IWI, and BMAC routes have been fully characterized, as detailed in our previous work (Couto-Pessanha *et al.*, 2024).

EPR measurements were carried out at room temperature on a Bruker Elexsys (E500) spectrometer operating at X-band (~9.8 GHz) with a DC magnetic field ranging from 336 to 346 mT, an AC magnetic field with a frequency of 100 kHz and modulation amplitude of 1 G, microwave power of 10 mW and 5 scans of 60 s. 2,2,6,6-Tetramethylpiperidine (TEMP) and 5,5-Dimethyl-1-pyrroline N-oxide (DMPO) were used as $^{\bullet}O_2^-$ and $^{\bullet}OH$ trapping agent, respectively. In a typical procedure, 1 mg of the material was suspended in 1 mL of TEMP (100 mM, $C_9H_{19}N$, Sigma-Aldrich, purity ≥ 99%) aqueous solution for $^{\bullet}O_2^-$ probe, and in 1 mL of DMPO (100 mM, $C_6H_{11}NO$, Sigma-Aldrich, purity ≥ 98%) aqueous solution for $^{\bullet}OH$ probe, both in Eppendorf tubes. The suspensions were kept under stirring and irradiated for 10 min by a Xenon lamp (200 W). The experiments were performed at room temperature and after being irradiated for 10 min, 30 µL of the suspensions were placed in a capillary tube and then the tube was inserted into the high-sensitivity (cylindrical) resonant cavity.

The TEMP-($^{\bullet}O_2^-$) and DMPO-($^{\bullet}OH$) adduct identification in aqueous solution was carried out through the EPR spectra simulation using the Easyspin package in MATLAB® software. To characterize the TEMP-($^{\bullet}O_2^-$) adduct, spin Hamiltonian parameters were used considering an electronic spin S = ½ interacting with the nuclear spins of 14N (I = 1), with the hyperfine splitting constant of a_N = 1.479 mT. For the DMPO-($^{\bullet}OH$) adduct, we consider an S = ½ system interacting with the nuclei 1H (I = ½) and 14N (I = 1), with the hyperfine splitting constants being a_N = 1.490 mT and a_H =1.490 mT. The quantification of $^{\bullet}O_2^-$ and $^{\bullet}OH$ radicals was performed by double integration of EPR spectra and comparing them to the 4-Hydroxy-TEMPO (Sigma-Aldrich, purity ≥ 97%) standard.

5.3
Results and discussion

Figure 24 shows the EPR signal, where hyperfine transitions typical for ROS, can be observed. It is possible to observe that in all cases, the heterojunctions exhibit more intense signals in comparison to neat P90, which is directly correlated with an increased production of ROS by these materials. Specifically, the signal displayed in Figure 24a is ascribed to the TEMP-$^{\bullet}O_2^-$ spin adduct (Nardi *et al.*, 2014), whereas the signal in Figure 24b is related to the DMPO-$^{\bullet}OH$ spin adduct (Bačić *et al.*, 2008) both after 10 minutes of irradiation.

The EPR measurements revealed that the BM sample differed from the others, showing an enhanced generation of $^{\bullet}O_2^-$ and $^{\bullet}OH$ radicals. Strictly speaking, the $^{\bullet}OH$ photoproduction of the NiO/P90-BM sample (1.28 µM) was 4-times greater than that of the pure P90 sample (0.32 µM). Additionally, the production of $^{\bullet}O_2^-$ was greatly increased within the heterojunctions, with the NiO/P90-BM sample (110 µM) presenting a concentration of photogenerated $^{\bullet}O_2^-$ 117-times greater than that of the neat P90 sample (0.94 µM). In addition, the spin-trap quantification for the NiO/P90-IWI and NiO/P90-BMAC samples are compiled in Table 3. These results indicate that the architecture obtained for the NiO/TiO_2-BM p-n heterojunction provides optimized conditions for the photogeneration of $^{\bullet}O_2^-$ and $^{\bullet}OH$ radicals. On the other hand, the NiO/P90-IWI and NiO/P90-BMAC samples showed similar performance, between themselves, in the generation of $^{\bullet}O_2^-$ and $^{\bullet}OH$ radicals, indicating that each sample preparation method has advantages and disadvantages. The neat P90 sample consisting only of TiO_2 proved to be less effective in the radical photoproduction compared to the samples containing NiO. This demonstrates that, in all cases, the addition of NiO generated a synergistic effect with TiO_2, reducing the recombination rate and increasing light harvesting in the visible region as demonstrated in our previous work (Couto-Pessanha *et al.*, 2024).

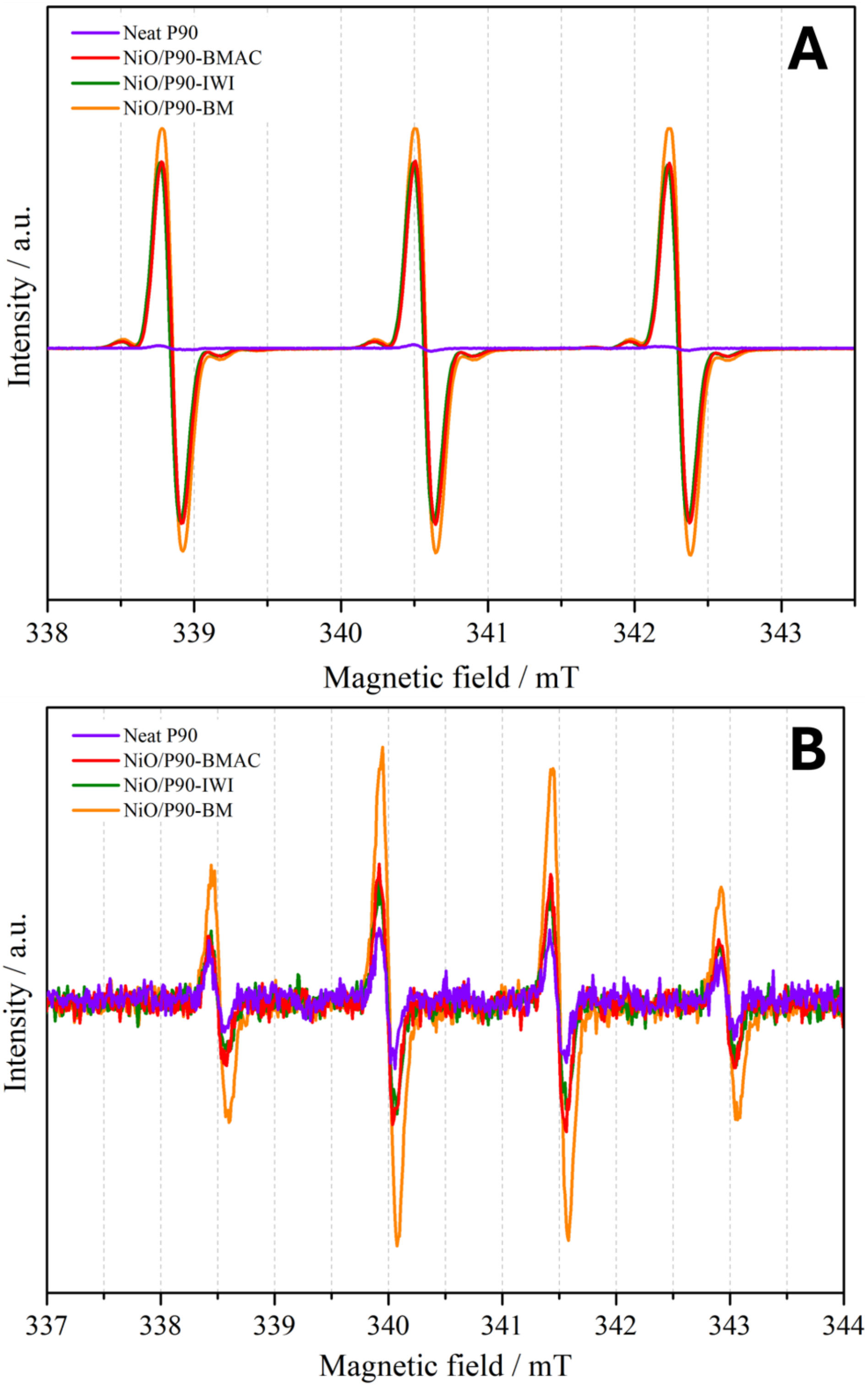

Figure 24: EPR spectra of the (A) TEMP-($\bullet O_2^-$) and (B) DMPO-($\bullet OH$) adducts formed after irradiation for 10 minutes of NiO/P90-BM, NiO/P90-IWI, NiO/P90-BMAC, and neat P90 samples.

Table 3: Quantification of TEMP-($^{\bullet}O_2^-$) and DMPO-($^{\bullet}OH$) adducts formed after irradiation for 10 minutes of NiO/P90-BM, NiO/P90-IWI, NiO/P90-BMAC, and neat P90 samples.

Sample	**TEMP-($^{\bullet}O_2^-$) [μM]**	**DMPO-($^{\bullet}OH$) [μM]**
P90	0.94	0.32
NiO/P90-BM	110	1.28
NiO/P90-IWI	93	0.52
NiO/P90-BMAC	92	0.60

In this previous work (Couto-Pessanha *et al.*, 2024), we conducted a detailed and comprehensive characterization of NiO/TiO_2 heterojunctions synthesized *via* BM, IWI, and ball milling followed by calcination (designated BMAC) using various techniques. Transmission electron microscopy (TEM) analysis revealed a uniform and well-dispersed distribution of NiO clusters (< 2 nm) supported on TiO_2 (P90) in the BM and IWI samples. On the other hand, coarsening of clusters to nanoparticles (< 10 nm) was observed in the BMAC sample, t.

Electrochemical impedance spectroscopy (EIS) measurements demonstrated that, in all cases, the addition of NiO on the surface of TiO_2 favored charge transfer efficiency, *i.e.*, a decrease in charge transfer resistance, along with a reduction in recombination rate and a higher density of charge carriers when irradiated. For the sample obtained by BM, these effects were more significant, showing that mechanochemical synthesis facilitated the formation of a highly active NiO/TiO_2 interface, promoting efficient charge transfer and consequently likely to favor increased ROS generation.

Additionally, in this previous study, X-ray absorption spectroscopy (XAS) was employed at the Ni L-edge to investigate the electronic structure of NiO clusters in NiO/TiO_2 heterojunctions. Interestingly, the analysis revealed that in samples obtained by mechanochemistry, *i.e.*, both BM and BMAC, the high-spin (HS) configuration of Ni^{2+} species in NiO is dominant, whereas in the IWI sample, a more significant contribution of the low-spin (LS) state to these species was observed. The presence of unpaired electrons, generally more reactive, in the *d* orbitals of the HS configuration has been previously reported to favor the reactivity of these electrons. Conversely, in the LS configuration, all electrons in the 3*d* shell are paired. This characteristic demonstrated influence on the activity of different p-n NiO/TiO_2 heterojunctions for H_2 photoproduction. Through the findings reported here, it is likely that the same effects are also significant for the photoproduction of the $^{\bullet}O_2^-$ and $^{\bullet}OH$ radicals.

5.4.
Conclusions

In this study, we explored the efficiency of NiO/TiO_2 heterojunctions synthesized by BM, IWI, and BM followed by calcination (designated as BMAC) as catalysts for the photoproduction of $^{\bullet}O_2^-$ and $^{\bullet}OH$ radicals driven by solar irradiation. The results of *in-situ* detection *via* EPR/Spin trapping demonstrated that the synthesis via BM provides an optimized NiO/TiO_2 architecture for the formation of these radicals compared to the IWI and BMAC approaches. Specifically, the NiO/P90-BM sample exhibited a $^{\bullet}O_2^-$ photogeneration rate of 110 µM and $^{\bullet}OH$ of 1.28 µM, compared to 0.94 µM and 0.32 µM for the neat P90 sample. These data, together with those previously reported by us, reveal that this behavior is likely a result of efficient charge separation provided by the formation of a p-n heterojunction. Additionally, a predominant high-spin (HS) configuration in the BM sample would also enhance the photocatalytic activity of this material. These results demonstrate that mechanochemical synthesis via BM brings not only benefits related to the absence of the use of polluting chemicals and hazardous solvents but also plays a crucial role in optimizing the catalytic properties of NiO/TiO_2 p-n heterojunctions for efficient $^{\bullet}O_2^-$ and $^{\bullet}OH$ photoproduction.

6.
Cu_2O nanocubes/TiO_2 heterostructure and its adsorption and photocatalytic properties for tetracycline removal

Emanuel C. Pessanha, Francine A. F. Menezes, André O. Guimarães, Paula Mendes Jardim, Bojan A. Marinkovic

The results presented in chapter 6 were published in the Journal of Photochemistry and Photobiology A: Chemistry (Elsevier), 2023. DOI: 10.1016/j.jphotochem.2023.114652.

6.1
Background

The presence of active pharmaceutical ingredients (API) in riverbeds is an emerging consequence of several factors, such as the increase in consumption of pharmaceutical products, population concentration in large cities, and inappropriate, or non-existent, sewage and rubbish disposal and treatment (Larsson e Flach, 2021; Wei, Liu e Shangguan, 2020; Wilkinson *et al.*, 2022). Among the APIs antibiotics consist of a large group. Disposal and accumulation of antibiotics in the environment can lead to the emergence of multidrug-resistant (MDR) bacteria, or “superbugs”, which are often reported as a great threat to human health (Gao e Zhang, 2021; Larsson e Flach, 2021; Punia *et al.*, 2021; Zhang *et al.*, 2015; Zhuang *et al.*, 2021). Despite the risk represented by these compounds, conventional wastewater treatment plants are still unable to remove them (Rogowska *et al.*, 2020).

According to contemporary literature, tetracycline (TC) is one of the most widely used classes of antibiotics worldwide. Furthermore, different authors reported that adsorption is an up-to-date, simple, efficient, low cost and relevant interface process for attaining TC removal from aqueous media (Ahmadijokani *et al.*, 2022; Biswal e Balasubramanian, 2022; Ibrahim, Creedon e Gharbia, 2022; Kang *et al.*, 2022; Leichtweis *et al.*, 2022). Cuprous oxide (Cu_2O) is pointed out as an efficient adsorbent of different aqueous and gaseous pollutants (Liao e Wang, 2018; Ma e Cao, 2021; Shu *et al.*, 2015). However, the large-scale application of pure Cu_2O for this purpose is not feasible due to its poor stability in the presence of moisture, tending to oxidize, *i.e.*, to form cupric oxide (CuO) (Janczarek e Kowalska, 2017; Li, X. *et al.*, 2019). Among the strategies to increase the stability of Cu_2O is the design of heterojunctions adding a wider band gap semiconductor (Janczarek e Kowalska, 2017; Li, X. *et al.*, 2019; Paracchino *et al.*, 2011). Therefore, TiO_2 is an appropriate candidate to form a heterojunction with Cu_2O due to its wider band gap, low cost, high stability, and non-toxicity (Li *et al.*, 2022).

Hence, a Cu_2O NCs/TiO_2 heterostructure with an efficient TC adsorption, attained *via* a simple and fast route, is presented in this work.

In addition, another successful strategy to achieve aqueous and gaseous pollutants removal is heterogeneous photocatalysis (Almeida *et al.*, 2020, 2022b; Ariza-Tarazona *et al.*, 2019; Habran, Krambrock, *et al.*, 2018; Khalid *et al.*, 2017). Heterostructures combining Cu_2O and TiO_2 are widely used also in the context of heterogeneous photocatalysis (Janczarek e Kowalska, 2017; Sekar *et al.*, 2021; Sharma *et al.*, 2022; Wang, Y. *et al.*, 2017; Xing *et al.*, 2021b; Yan *et al.*, 2020). Strictly speaking, in the case of Cu_2O NCs, there is a divergence in the literature on its feasibility as a photocatalyst. *Cao et al*. (Cao *et al.*, 2014) reported a route for Cu_2O NCs synthesis with tunable size and considered them as a good visible light photocatalyst for methyl orange (MO) degradation. Likewise, Messaadia *et al*. (Messaadia *et al.*, 2023), reported a Cu_2O/TiO_2 heterostructure, obtained by physical mixing of Cu_2O, allegedly having NCs morphology, and TiO_2, as a good photocatalyst for Rhodamine B degradation. According to them, the best performance for Rhodamine B photodegradation was achieved for a mass ratio of 1:1 for Cu_2O NCs and TiO_2. In the opposite direction, *Chu* and *Huang* (Chu e Huang, 2017) analyzed different Cu_2O crystal shapes and examined their relationship with MO degradation ability using a Xenon lamp as the light source. They pointed out that Cu_2O NCs were photocatalytically inactive. In addition, few other studies reported that even when forming a heterostructure with Au (Yuan *et al.*, 2016) or ZnO (Wu, Tan e Huang, 2017), Cu_2O NCs continued to be photocatalytically inactive.

Considering this, in addition to the adsorption tests, photocatalytic tests were performed to analyze Cu_2O NCs/TiO_2 photocatalytic activity for TC degradation. As the authors are aware, Cu_2O NCs photocatalytic activity with the grafted TiO_2 was not assessed before.

The main goals of this study were to: I) report a simple and fast route for the synthesis of Cu_2O NCs/TiO_2 heterostructure; II) evaluate and understand the TC removal ability of the Cu_2O NCs/TiO_2 heterostructure by adsorption; III) evaluate and understand the photocatalytic (in)activity of Cu_2O NCs/TiO_2 heterostructure towards TC degradation.

6.2.
Experimental

6.2.1.
Synthesis of Cu_2O NCs/TiO_2 heterostructure

All the chemicals and reagents were of analytical grade and were used without any further treatment.

For Cu_2O NCs/TiO_2 preparation, the Cu_2O NCs were first synthesized as previously reported (Chang *et al.*, 2013). Typically, 0.5292 g of trisodium citrate dihydrate ($C_6H_5Na_3O_7$. $2H_2O$, Sigma-Aldrich, purity $\geq$ 99%) was added to 800 mL deionized (DI) water and maintained under continuous stirring at room temperature. After 20 min, 2 mL of 1.2 M copper (II) sulfate pentahydrate ($CuSO_4$.5 H_2O, Sigma-Aldrich, purity $\geq$ 98%) solution was added. After 5 min, 2 mL of 4.8 M sodium hydroxide (NaOH, Sigma-Aldrich, purity $\geq$ 99%) solution was added. Finally, after another 5 min, 2 mL of 1.2 M of ascorbic acid ($C_6H_8O_6$, Sigma-Aldrich, purity $\geq$ 99%) solution was added and the solution was kept under stirring for an additional 30 min. The resultant product was rinsed several times with DI water and absolute ethanol.

Meanwhile, 150 mg of TiO_2 P25 (Evonik®) was suspended under sonication for 30 min in ethanol to achieve a 1:1 TiO_2/Cu_2O mass ratio. The previously prepared Cu_2O NCs were added to TiO_2 P25 suspension to achieve Cu_2O NCs/TiO_2 heterostructure. Afterward, the resultant suspension was kept under stirring at 50 °C until complete ethanol vaporization.

6.2.2.
Synthesis of reference Cu_2O/TiO_2 heterostructure

Commercial Cu_2O (Dinâmica®) and TiO_2 P25 (Evonik®) were used to prepare a reference adsorbent material. This material was obtained by adding commercial Cu_2O powder into the TiO_2 P25 ethanol suspension, keeping a 1:1 mass ratio. Afterward, the suspension was kept under stirring at 50 °C until complete ethanol vaporization. The reference adsorbent was labeled as Cu_2O/TiO_2.

6.2.3.
Characterization of Cu_2O NCs/TiO_2 heterostructure

XRPD was accomplished in a Bruker D8 Advance diffractometer with CuK_α radiation ($\lambda = 1.5418$ Å) to determine the phase composition of the sample. The data were obtained at room temperature, in the 2θ range from 20° to 90°, with a step size of 0.02° and acquiring time of 1 s per step. The average crystallite sizes of the Cu_2O and anatase (the predominant TiO_2 phase in P25 material) were estimated by means of the Le Bail method, considering the Integral Breadth (IB) of diffraction lines. The phase mass fraction was estimated by quantitative Rietveld analysis, using Topas 4.2 software (Bruker, Billerica, MA, USA). The specific surface areas were calculated from N_2 adsorption isotherms by Brunauer-Emmmett-Teller (BET) approach.

To evaluate the morphology and perform semiquantitative chemical analysis of the Cu_2O NCs/TiO_2 heterostructure, TEM images, EDS mapping, and SAED patterns were acquired on a JEM-2100F operating at 200 kV. Previously, a small amount of powder was ultrasonically dispersed in isopropyl alcohol for 30 min and then dropped onto a holey carbon film supported by a copper grid.

The diffuse reflectance spectroscopy (DRS) analyses were performed through a Perkin-Elmer Lambda 650 UV/Vis spectrophotometer (Perkin-Elmer, Waltham, MA, USA), applying spectralon® as blank reference. The DRS data were used as input for the Kubelka-Mulk function to estimate band-gap energies through linear fitting using the Origin 9.0 software.

6.2.4.
Measurement of the TC adsorption removal efficiency

The TC adsorption tests were carried out using 50 $mg.L^{-1}$ of Cu_2O NCs/TiO_2, Cu_2O/TiO_2, TiO_2 P25, and Cu_2O NCs, the different samples tested as adsorbent, and 10 $mg.L^{-1}$ of TC. The attenuation of the absorbance intensities of the characteristic bands of TC at 276 nm and 358 nm was measured as an indication of the adsorption process. At given time intervals 5 mL aliquots of supernatant were acquired and then filtered and analyzed in a UV-Vis spectrophotometer (Agilent, model 8453).

In a typical test, the TC was added to a beaker containing 1 L of DI water and kept under vigorous stirring for 10 min. Then, the adsorbent material was added and the system was kept under stirring for additional 10 min. At that time an aliquot was acquired and labeled as 0’. Afterward, other aliquots were subsequently acquired and labeled according to the acquisition time regarding point 0’. The tests were carried out at room temperature and in dark.

The FTIR spectroscopy was performed on the Cu_2O NCs/TiO_2 heterostructure, before and after the adsorption process, using Bruker ALPHA II Platinum-ATR spectrometer. Spectra were recorded from 400 cm^{-1} to 4000 cm^{-1}, with a resolution of 4 cm^{-1} and 32 scans.

The TGA and differential scanning calorimetry (DSC) analysis were carried out on the Cu_2O NCs/TiO_2 heterostructure, before and after the adsorption process was completed, using a Perkin-Elmer Simultaneous Thermal Analyzer, STA 6000 (Perkin-Elmer, Waltham, MA, USA), under synthetic air flow (20 mL min^{-1}), at a heating rate of 10 ºC.min^{-1} in the temperature range of 30 - 800 ºC.

6.2.5.
Measurement of the TC photocatalytic efficiency

The photocatalytic test of TC abatement was carried out through a previously defined methodology (Almeida *et al.*, 2022b) using a DULUX D/E 26 W residential fluorescent lamp as the light source. The aliquots were acquired at the same time intervals as for the adsorption test (section 2.4).

To gain more insights on the ROS production by the Cu_2O NCs/TiO_2 heterostructure and, therefore, its photochemical activity, EPR measurements were carried out at room temperature on a Bruker Elexsys (E500) spectrometer operating at X-band (~9.8 GHz) with a DC magnetic field ranging from 3360 to 3460 G, an AC magnetic field with a frequency of 100 kHz and modulation amplitude of 1 G. In a typical procedure, 1 mg of the material was suspended into 1 mL of a 25 mM DMPO (Sigma-Aldrich) aqueous solution in an Eppendorf and then the suspension was kept under stirring and irradiated for 10 min by a Xenon lamp (200 W) with an FGL400 transmission filter ($\lambda < 400$ nm cut edge). After being irradiated, 30 µL of the suspension was placed in a capillary tube and then the tube was inserted into the high-sensitivity (cylindrical) resonant cavity, with a microwave power of 5 mW. As a prototype ROS system, the Fenton reaction with 0.1 mM FeSO4 and 30% H_2O_2 (Synth) was used to produce hydroxyl radicals.

6.3
Results

6.3.1.
Characterization of Cu_2O NCs/TiO_2 heterostructure

Figure 25 shows Rietveld refinement of the experimental XRPD pattern of the Cu_2O NCs/TiO_2 heterostructure. The diffraction peaks were indexed to the TiO_2-anatase (PDF-2: 21-1272), TiO_2-rutile (PDF-2: 21-1276) and Cu_2O (PDF-2: 05-0667). Quantitative phase analysis by the Rietveld method (see Supplementary Material) revealed 48.7 wt.%, 6.4 wt.%, and 44.9 wt.% for anatase, rutile, and cuprite, respectively. The average crystallite sizes of TiO_2-anatase and Cu_2O-cuprite were estimated to be 33 nm and 86 nm, respectively. The nitrogen adsorption/desorption tests following the BET approach revealed a surface area of 69 $m^2.g^{-1}$ for the Cu_2O NCs/TiO_2 sample and 25 $m^2.g^{-1}$ for the reference Cu_2O/TiO_2 sample. In addition, Figure 41a-c shows the XRPD patterns for reference Cu_2O/TiO_2 heterostructure, TiO_2 P25, and commercial Cu_2O, respectively.

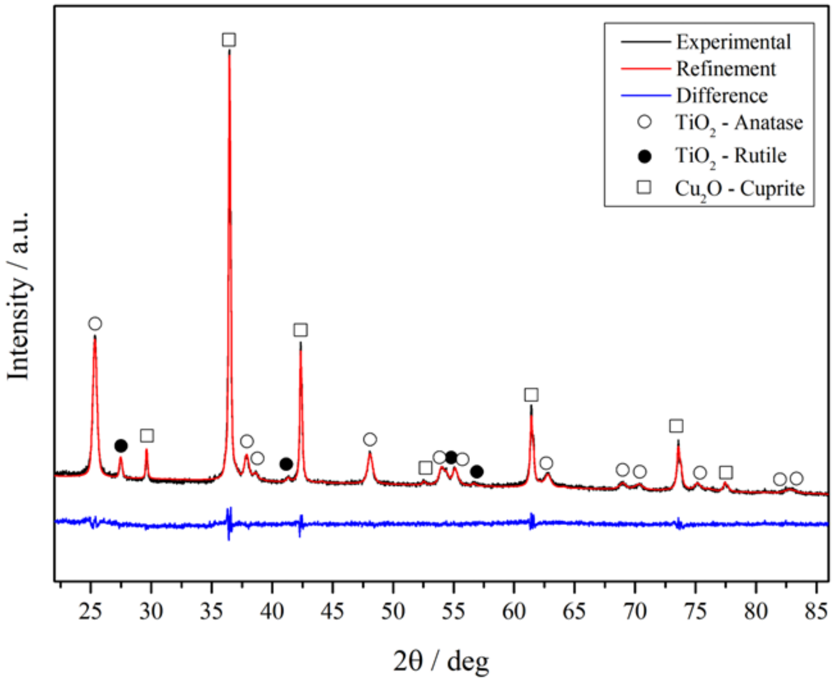

Figure 25: Experimental XRPD patterns refined by the Rietveld method for Cu_2O NCs/TiO_2 heterostructure. The black line corresponds to the experimental pattern and the red line corresponds to the calculated pattern, whereas the difference plot is blue.

A representative TEM image (Fig. 26-a) shows that TiO_2 nanoparticles are in contact with Cu_2O NCs. The primary particle size estimated from TEM images for TiO_2 and Cu_2O (Fig. 26-a) corroborates the average crystallite size calculated by the Le Bail method for anatase and Cu_2O in Cu_2O NCs/TiO_2 heterostructure. Furthermore, EDS maps (Fig. 26-b) confirm that the nanocubes are composed of Cu and O and that the smaller nanoparticles are composed of Ti and O. These results along with the XRPD patterns (Fig. 25) allow to affirm that our facile synthesis route successfully achieved the Cu_2O NCs/TiO_2 heterostructure.

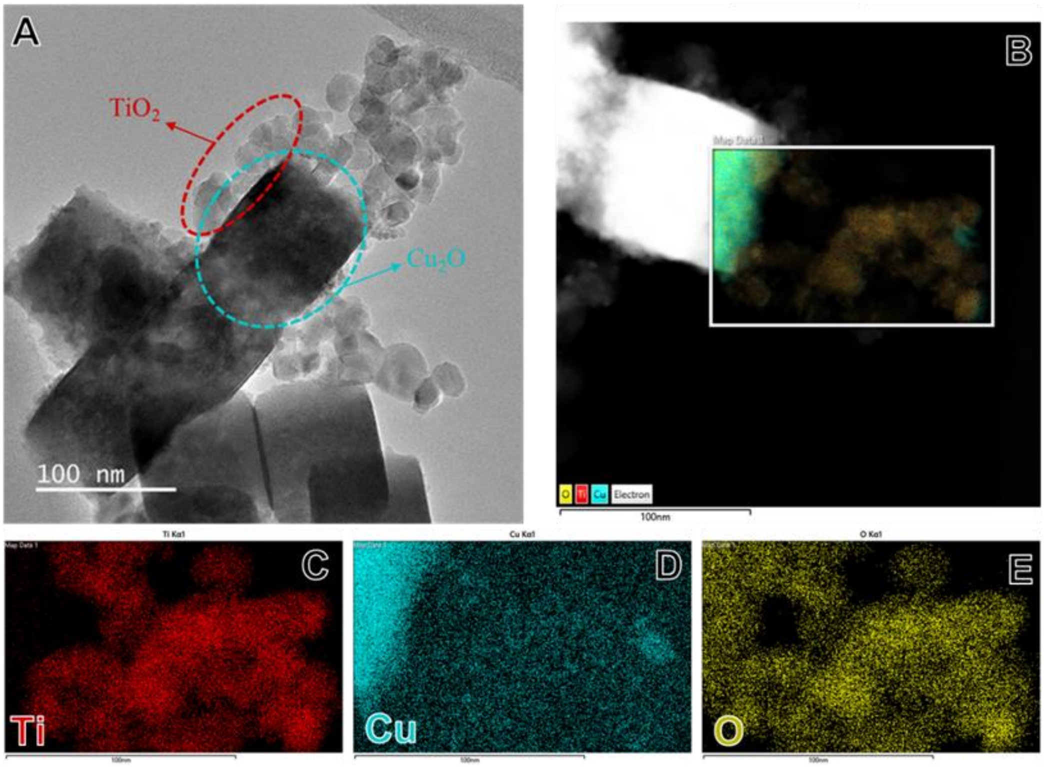

Figure 26: (a) TEM image of the Cu_2O NCs/TiO_2 heterostructure, (b) the image of the area mapped by EDS (b), (c-e) and titanium, copper, and oxygen elemental maps.

Figure 27-a shows a single-crystalline SAED pattern from the isolated Cu_2O cube, presented in Figure 27-b. In addition, noteworthy, the SAED pattern demonstrated that the facets of Cu_2O cubes are made from {100} planes. Figure 42 shows details of (SAED) patterns acquisition and indexing.

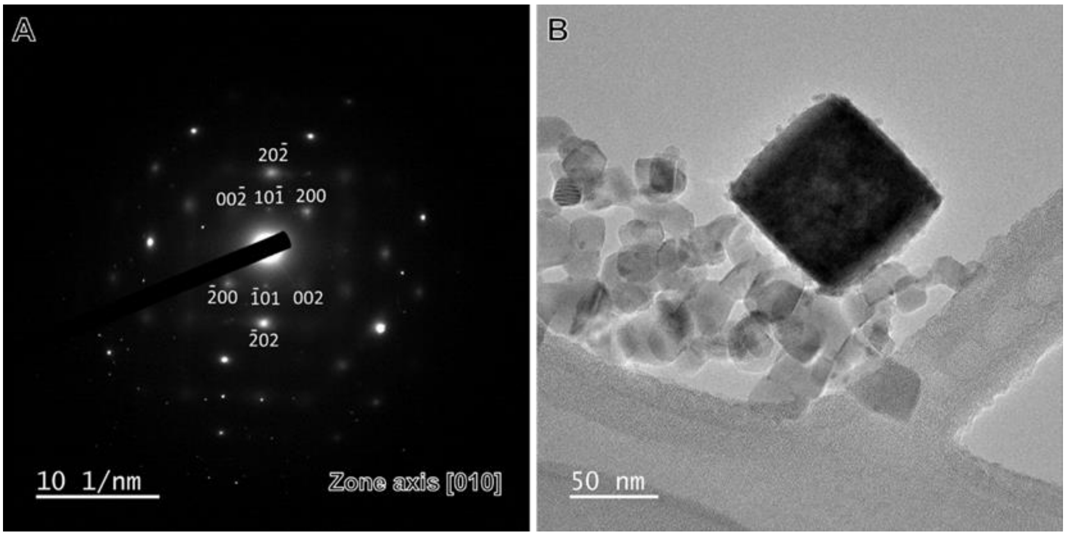

Figure 27: (a) SAED pattern along [010] zone axis taken from the single-crystalline Cu_2O cube (b) TEM image of a single-crystalline Cu_2O cube with {100} facets.

The band gap values were calculated considering the linear portion of reflectance spectra (Fig. 43-a) converted by the Kubelka-Munk function (Fig. 28). The obtained values, 3.15 eV and 2.10 eV, are in accordance with those reported for TiO_2-anatase (Ruan *et al.*, 2022) and Cu_2O (Bayat e Sheibani, 2022), respectively.

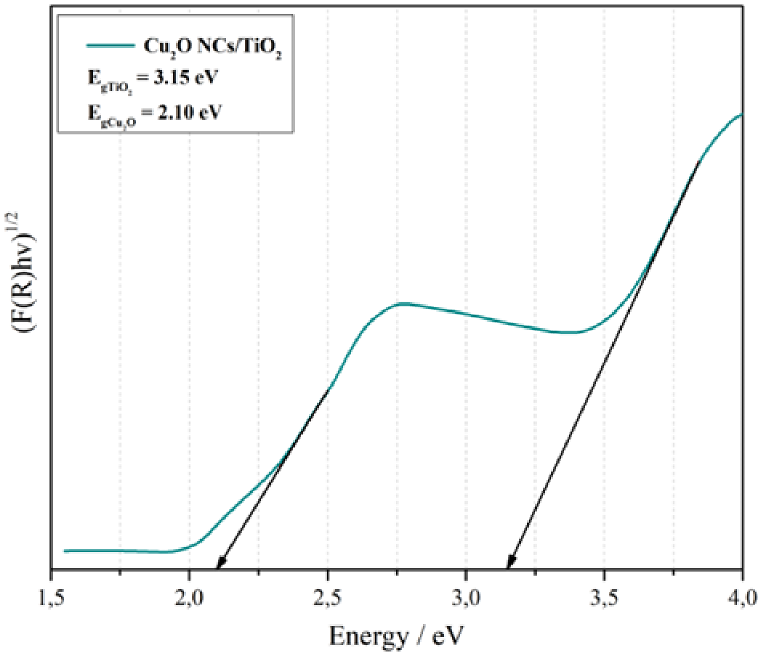

Figure 28: Tauc plot of Cu_2O NCs/ TiO_2 heterostructure and apparent bandgaps for anatase (TiO_2) and cuprite (Cu_2O) phases.

6.3.2.

TC adsorption removal efficiency of the Cu_2O NCs/TiO_2 heterostructure

The adsorption efficiency of the Cu_2O NCs/TiO_2 heterostructure was assessed by the TC removal from an aqueous solution of TC in DI water (10 mg.L^{-1}). Figure 29-a shows the absorbance spectra of the TC after different time periods. The TC was completely removed by adsorption from the solution by the Cu_2O NCs/TiO_2 heterostructure, reaching the 100 % removal rate after 110 min (Fig. 29-b). In contrast, after the same 110 min, the reference Cu_2O/TiO_2 sample reached only 30% of TC removal Fig. 29-b). For the sake of comparison, TC adsorption tests were carried out separately for neat TiO_2 P25 and neat Cu_2O NCs phases (Fig. 44), used for preparation of the Cu_2O NCs/TiO_2 heterostructure, following the very same procedure described in section 2.4.

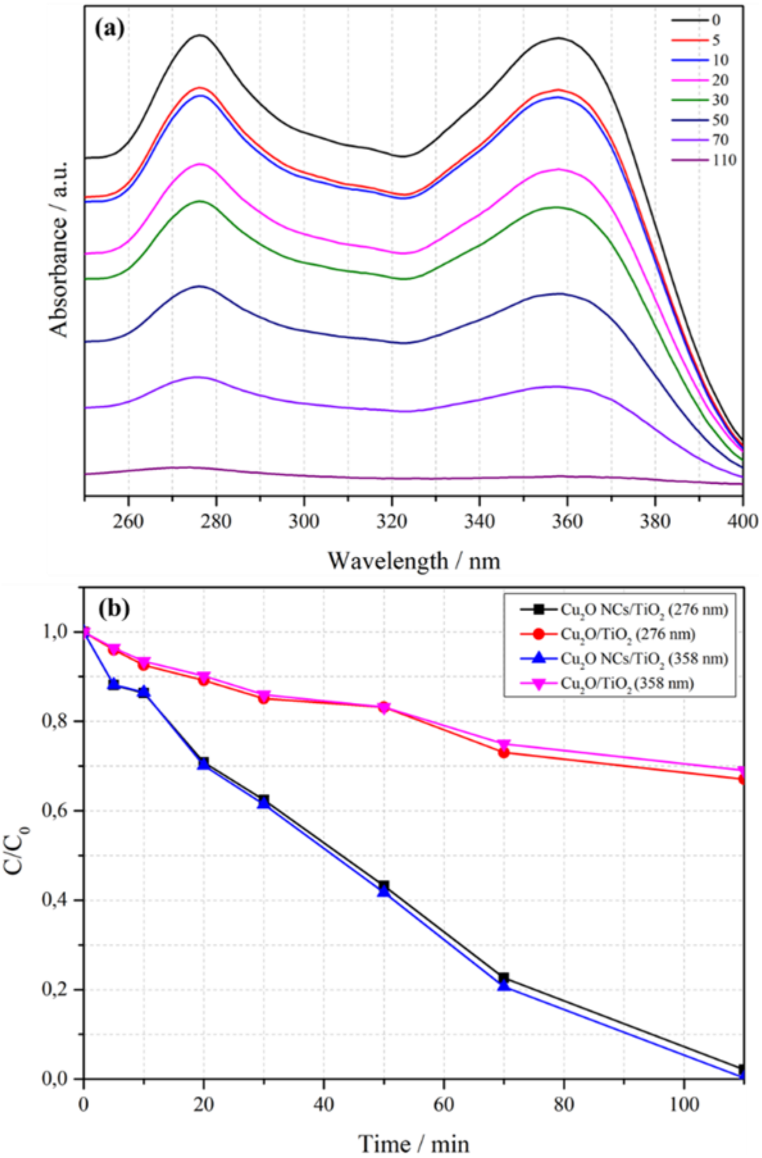

Figure 29: (a) Absorbance spectra of the TC at different periods of time after Cu_2O NCs/TiO_2 addition and (b) TC fraction as a function of time, monitored through the main absorption peaks of TC, situated at 276 nm and 358 nm, in the presence of Cu_2O NCs/TiO_2 and Cu_2O/TiO_2 reference samples as adsorbents.

The FTIR analysis was carried out to verify the presence of TC molecules adsorbed on Cu_2O NCs/TiO_2 heterostructure surface. After the procedure described in section 2.4, the aqueous reaction media was centrifuged, and the obtained powder was dried at room temperature and then analyzed. Figure 30 shows the FTIR spectra for Cu_2O NCs/TiO_2 heterostructure before and after this process.

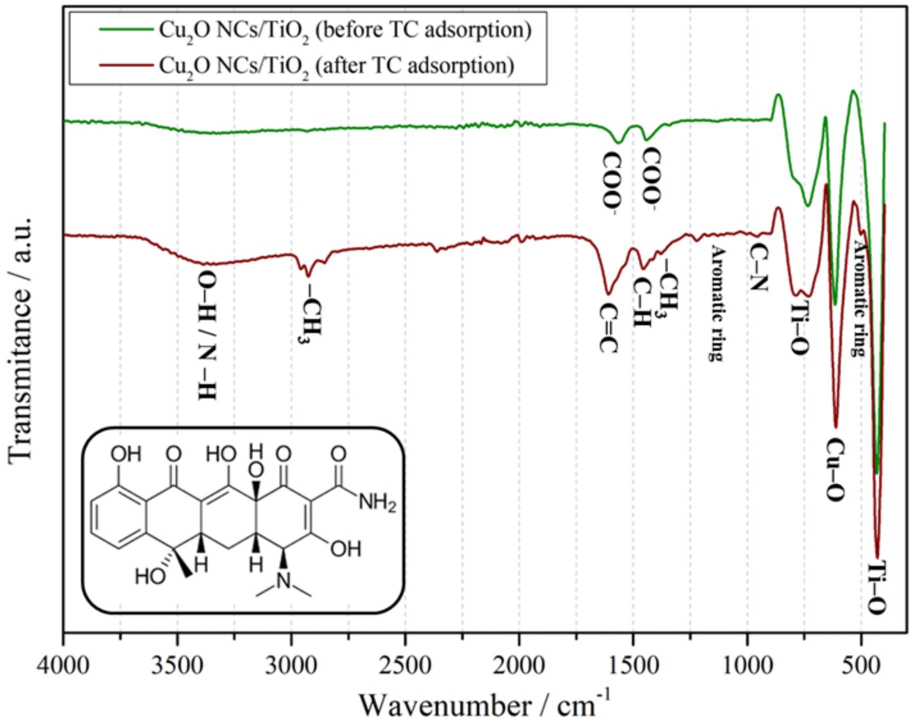

Figure 30: Fourier-transform infrared (FTIR) spectra of Cu_2O NCs/TiO_2 heterostructure before and after the TC adsorption process. The inset shows TC structural formula.

The sharp bands located in both samples at 463 cm^{-1} and 610 cm^{-1} can be ascribed to Ti–O and Cu–O stretching vibration modes of TiO_2 (anatase) [39,40] and Cu_2O (cuprite) [41], respectively. Besides, the band near 730 cm^{-1} is assigned to Ti–O–Ti bonds vibrations modes in TiO_2. In both spectra, the occurrence of the peaks around 1400 cm^{-1} and 1600 cm^{-1} can be ascribed to symmetric and asymmetric stretching, respectively, of the COO^- group of trisodium citrate molecules [42,43], which was not totally removed during the rising process.

The appearance of characteristic peaks of TC in the spectrum after the adsorption process demonstrates the presence of TC on Cu_2O NCs/TiO_2 surface. The vibrational peak around 965 cm^{-1} can be ascribed to the C–N bond stretching of amide [44]. The peaks in the range 570 - 500 cm^{-1} and 1250 - 1000 cm^{-1} are ascribed to the out-plane and in-plane aromatic ring deformation, respectively [44]. The bond bending peaks of $–CH_3$ and C–H bonds in the aromatic ring are around 1360 cm^{-1} and 1460 cm^{-1}, respectively [44–46]. Lastly, the band in the range 1650 - 1580 cm^{-1} is attributed to the C=C bonds vibration of TC benzene ring, whereas the peaks in the range 2995 - 2860 cm^{-1} are assigned to C–H bonds stretching on –CH_3 radical [44].

The presence of a weak and wide band in the range 3500 - 3000 cm^{-1} in both spectra can be ascribed to O–H bond stretching, due to the presence of moisture in the sample surface [47]. However, it is possible to verify an intensity increase in this region after the TC adsorption due to the overlapping of N–H bond absorption peak, which is located at 3340 - 3329 cm^{-1} [44].

The TGA is presented in Fig. 31-a. Interestingly, in the range from room temperature up to 250 ºC a two-fold mass loss is observed for Cu_2O NCs/TiO_2 after TC adsorption compared to Cu_2O NCs/TiO_2 before TC adsorption. This greater mass loss after the adsorption process may be linked to the thermal decomposition or desorption of TC adsorbed on the surface. According to the literature, the mass loss up to this temperature is assigned to the process of desorption of organic molecules from the material surface. [48,49]. This allows affirming that TC was adsorbed on Cu_2O NCs/TiO_2 surface. Before adsorption, 1% of mass loss is recorded up to 230 ºC. Up to ~ 100 ºC the mass loss is ascribed to water loss. On the other hand, the mass loss above this temperature and up to 230 ºC could be ascribed to the decomposition of some citrate remaining on the surface, as evidenced by the FTIR spectrum before adsorption (Figure 30). Furthermore, both Cu_2O NCs/TiO_2 before and after TC adsorption show a mass increase in the range of 220 – 350 ºC, which is ascribed to Cu_2O oxidation [50].

The DSC curve (Fig. 31-b) for Cu_2O NCs/TiO_2 after TC adsorption shows a more intense endothermic peak in comparison to Cu_2O NCs/TiO_2 before TC adsorption. This feature can be assigned to the desorbing process of TC adsorbed onto Cu_2O NCs/TiO_2 heterostructure surface.

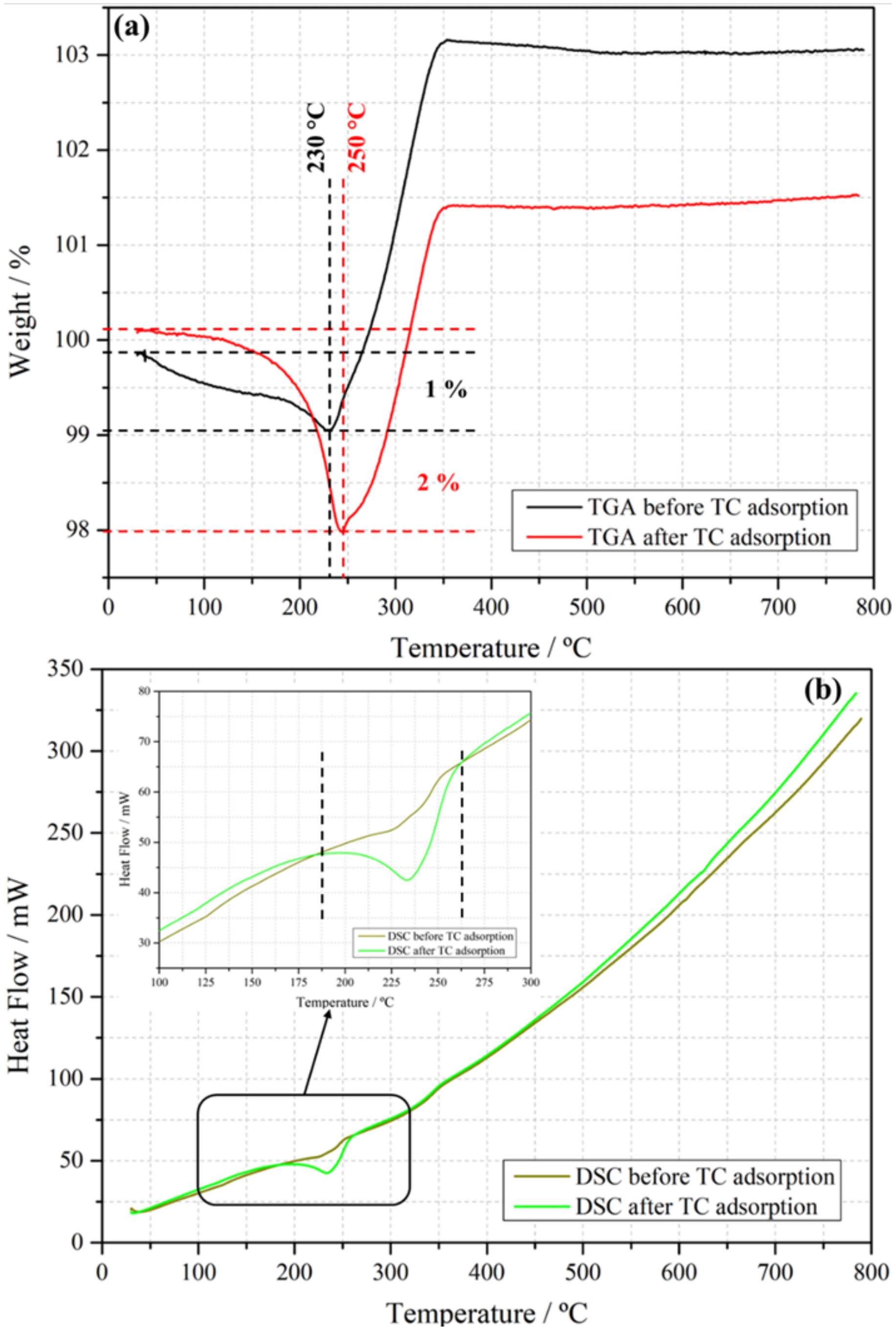

Figure 31: (a) TGA and (b) DSC curves of Cu_2O NCs/ TiO_2 heterostructure before and after the TC adsorption process.

6.3.3.

Photocatalytic efficiency of Cu_2O NCs/TiO_2 heterostructure for TC degradation

TC removal from an aqueous solution by Cu_2O NCs/TiO_2 heterostructure was carried out under visible light and in the dark to compare the resultant removal and to indirectly assess the feasibility of the material as a visible light-sensitive photocatalyst. Under visible light, the Cu_2O NCs/TiO_2 heterostructure took roughly the same time interval, as in dark conditions, to achieve a removal of 100% (Fig. 32), which suggested photocatalytic inactivity of Cu_2O NCs/TiO_2 for TC removal.

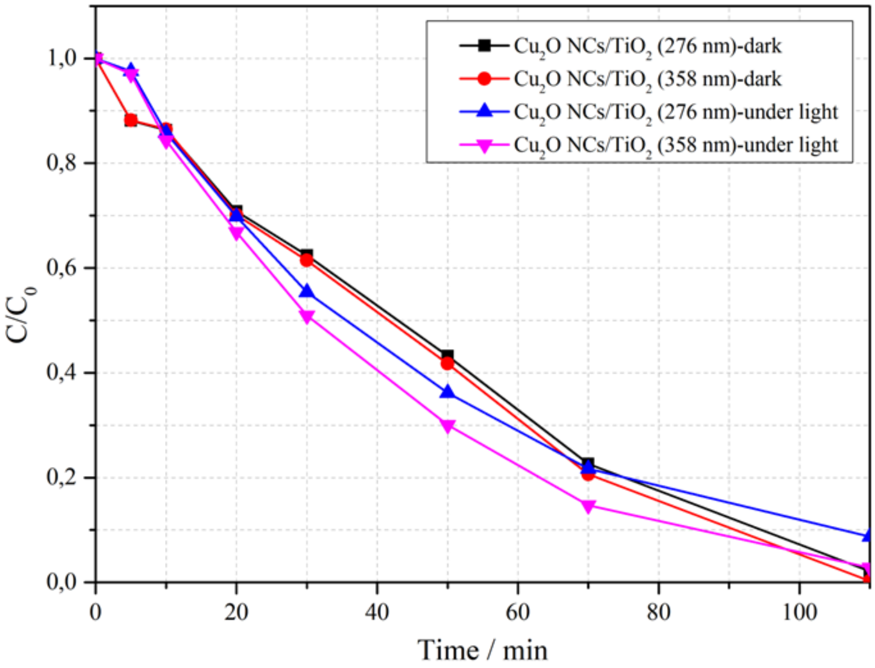

Figure 32: TC fraction as a function of time, monitored through the main absorption peaks of TC, situated at 276 nm and 358 nm, in the presence of Cu_2O NCs/TiO_2 sample under visible light and in the dark.

Furthermore, the spin trapping technique was carried out by EPR spectroscopy using DMPO as the trapping agent to investigate ROS generation by the Cu_2O NCs/TiO_2 heterostructure.

The EPR signal of the Cu_2O NCs/TiO_2 sample, suspended in a 25 mM DMPO aqueous solution, is shown in Figure 33 (blue spectrum). Interestingly, no detectable spin adducts related to ROS were identified, which corroborates the photocatalytic inactivity of Cu_2O NCs/TiO_2. To validate the methodology, Figure 33 also shows the spectrum (black spectrum) for trapped hydroxyl radicals (DMPO-OH adducts), generated by the Fenton reaction, using the very same experimental conditions for data acquisition. This spectrum is due to the interaction of the unpaired electron with one nitrogen and one hydrogen nucleus. The simulation (red spectrum), using EasySpin package (5.2.35), yields the hyperfine splitting constants a_N = 15.6 G and a_H = 15.0 G, confirming the detection of DMPO-OH adducts (Villamena, Hadad e Zweier, 2003).

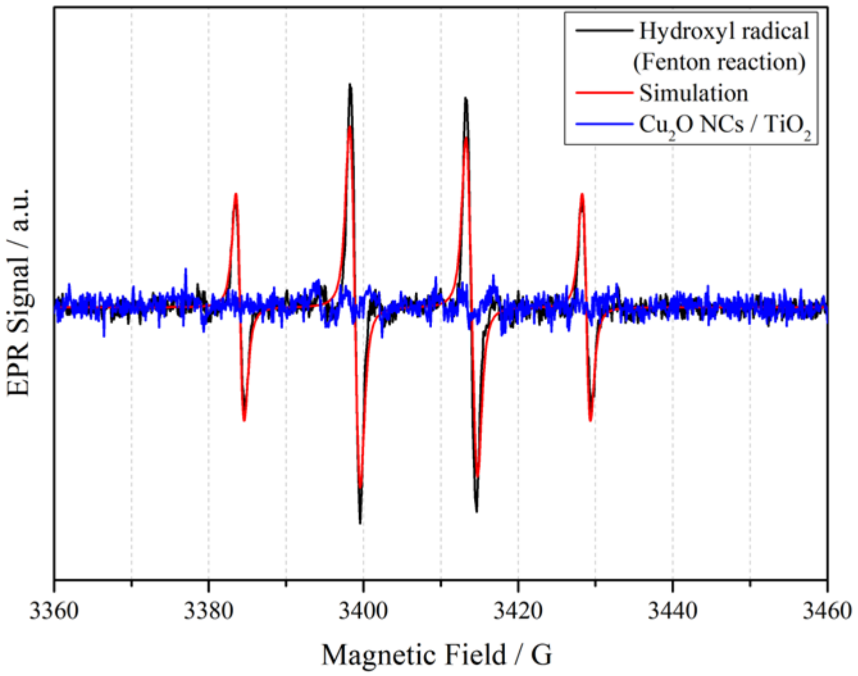

Figure 33: EPR spectrum of Cu_2O NCs/TiO_2 sample suspended in DMPO spin trap solution (blue). Experimental (black) and simulated (red) EPR spectra for DMPO-OH adducts generated by the Fenton reaction.

6.4.
Discussion

Among the main goals of this work, was achieving an efficient TC adsorbent by a simple and easily reproducible synthetic route. Our results, such as the absorbance in dark, FTIR, and TGA (Figures 29, 30, and 31) show that the goal was achieved.

A surface area of 69 $m^2.g^{-1}$ was presented by Cu_2O NCs/TiO_2 heterostructure, whilst a surface area of 25 $m^2.g^{-1}$ was exhibited by reference Cu_2O/TiO_2 sample. A higher surface area leads to a larger amount of dangling bonds per gram of material *i.e.*, more available active sites for the adsorption process on the surface (Al-Ghouti e Da’ana, 2020; Li *et al.*, 2020). In view of that, higher surface area could be identified as one of the promoters of the efficient adsorption exhibited by Cu_2O NCs/TiO_2 sample compared to the Cu_2O/TiO_2 reference sample.

Furthermore, *Wang et al.* (Wang *et al.*, 2021) have suggested that the adsorption capacity of Cu_2O for TC can be explained by the high chemical interaction between Cu(I) and the NH_2 group from TC, being the Cu(I) atoms the TC adsorption sites. Thus, since Cu_2O NCs {100} facets (Fig. 45-b) are Cu(I)-

terminated only (Sun *et al.*, 2018), the efficient TC adsorption by Cu_2O NCs/TiO_2 heterostructure would also be due to the {100} facet effect.

In addition, among the low-index facets of Cu_2O crystals, *Ferrer et al.* (Ferrer *et al.*, 2019) have demonstrated that {100} facets have the highest theoretical surface energy of 1.26 $J.m^{-2}$, relative to the 1.04 $J.m^{-2}$ and 0.76 $J.m^{-2}$ for {110} and {111} facets, respectively. Furthermore, they found that {100} Cu_2O facet is the most unsaturated low-index facet, which corroborates the verified highest surface energy. The number of dangling bonds per unit cell area of $0.21x10^{-10}$ m^2 was calculated for {100} Cu_2O facets, whereas $0.15x10^{-10}$ m^2 and 0.11 $x10^{-10}$ m^2 dangling bonds were calculated for {110} and {111} facets, respectively (Ferrer *et al.*, 2019). Our hypothesis is that both the highest surface energy and, therefore, the highest number of Cu(I) dangling bonds for {100} Cu_2O facets strongly contribute to the TC efficient adsorption by Cu_2O NCs/TiO_2 heterostructures. In comparison, the Cu_2O phase in Cu_2O/TiO_2 reference sample does not show clearly defined facets that could be attributed solely to the {100} family (Fig. 46).

Regarding the TC removal pathways, photocatalysis is more commonly reported in the literature. For the sake of comparison, *Almeida et al.* (Almeida *et al.*, 2022b) and *Gil-Londoño et al.* (Gil-Londoño, Krambrock, *et al.*, 2023) have reported a TiO_2−Acetylacetone Charge-Transfer Complex as a visible light-sensitive photocatalyst for TC degradation. They used a sample-to-pollutant ratio (SPR) of 40 and 10, respectively. Both reported ~70% of TC removal after 6 h, under visible light, for the best samples. Moreover, Shi *et al.* (Shi *et al.*, 2016) reported a Palygorskite-Supported Cu_2O-TiO_2 heterostructure for TC photodegradation. They reported ~89% of TC removal after 4 h, under visible light, using an SPR of ~33. In the present work, ~100% of TC removal after 110 min was accomplished with the reported Cu_2O NCs/TiO_2 heterostructure using an SPR of only 5. Finally, from the comparative analysis of Figures 29 and 44, the benefit of using Cu_2O NCs/TiO_2 heterostructures for the TC removal by adsorption, instead of neat Cu_2O and TiO_2, is clear.

Another important goal of the present work was to evaluate and understand the photocatalytic properties of the Cu_2O NCs/TiO_2 heterostructure, considering the disagreement in the literature on the efficient generation of charge carriers by Cu_2O cubes (Cao *et al.*, 2014; Chu e Huang, 2017; Wu, Tan e Huang, 2017; Yuan *et al.*, 2016). In this regard, we suggest that the Cu_2O NCs/TiO_2 heterostructure is photocatalytically inactive since there was no difference between TC removal under visible light and in the dark (Figure 29). As a proof-of-concept, we have also carried out EPR. The spin-trap concentration of 25 mM for the DMPO solution was used as recommended by *Pirozzi et al.* (Pirozzi *et al.*, 2020). No detectable spin adducts related to ROS were identified, which corroborates and brings new arguments to affirm the Cu_2O cubes' photocatalytic inactivity under visible light. These results are consistent with different studies (Chu e Huang, 2017; Wu, Tan e Huang, 2017; Wu *et al.*, 2019; Yuan *et al.*, 2016).

Since the Cu_2O NCs/TiO_2 heterostructure is visible light sensitive, as indicated by the Tauc plot (Fig. 28), most likely the observed photocatalytic inactivity is directly related to {100} facets. This might be explained by the hypothesis put forward by *Wu et al.* (Wu, Tan e Huang, 2017), that the photogenerated charge carriers (e^-/h^+) cannot reach the Cu_2O cube facets due to a large energetic barrier created by {100} facets. This barrier hinders the photogenerated charge carriers from reaching the surface and generating ROS and detectable photocatalytic activity. Also, according to *Su et al.* (Su *et al.*, 2017), this is linked to a high energy barrier that Cu_2O cubes' holes should surpass to reach the surface, resulting in the verified Cu_2O cubes' photocatalytic inactivity. According to *Chu* and *Huang* (Chu e Huang, 2017) the observed photocatalytic inactivity for Cu_2O cubes can be understood as a consequence of pronounced band bending near the surface caused by the {100} facets. Thus, the band gap near the surface layer of Cu_2O cubes is much larger than in the volume of Cu_2O. Furthermore, *Tan et al.* (Tan *et al.*, 2015) have shown that under the same voltage {111} Cu_2O octahedra crystals generate an electric current 244 times higher than {100} Cu_2O cubes. For photocatalytic purposes, it was demonstrated that the facility of electric charge generation and movement is directly linked to photocatalytic efficiency (Chen *et al.*, 2020b). Therefore, this may also corroborate the observed photocatalytic inactivity for Cu_2O cubes (Chu e Huang, 2017).

Cu_2O either with exposed facets other than {100} (Li, G. *et al.*, 2019) or non-defined shapes (Sekar *et al.*, 2021; Sharma *et al.*, 2022; Xing *et al.*, 2021b) was previously reported as an excellent narrow band gap semiconductor forming a heterostructure with TiO_2 resulting in outstanding photocatalysts. Thus, these findings highlighted that it is possible to completely change the behavior and the application of a compound through crystal shape control. Regarding the studies that have reported good photocatalytic activity for Cu_2O NCs (Cao *et al.*, 2014; Messaadia *et al.*, 2023), an incomplete control of the final morphology of Cu_2O might have led to misunderstandings on the photocatalytic activity of the Cu_2O cubes. Furthermore, dyes degradation under visible or solar light were the criteria used to assess the Cu_2O NCs or a Cu_2O NCs/TiO_2 heterostructure as a good photocatalyst. However, as pointed out by Rochkind *et al.* (Rochkind, Pasternak e Paz, 2015) and by *Sannino et al.* (Sannino *et al.*, 2015), dye degradation should not be used to assess a photocatalyst in visible light range due to sensitization phenomenon *i.e.*, the electronic transition between the highest occupied molecular orbital (HOMO) and the lowest unoccupied molecular orbital (LUMO) of adsorbed dye molecules and the subsequent injection of these electrons into the CB of the semiconductor. These electrons could promote ROS formation and then attack the dye molecule, which is a kind of ‘autophagy’ dye degradation.

6.5.
Conclusions

The current work has reported a facile, one-step, soft-chemical route for Cu_2O NCs/TiO_2 heterostructure synthesis.

FTIR and TGA/DSC analyses as well as adsorption tests for TC removal demonstrated a high adsorption efficiency of Cu_2O NCs/TiO_2. This adsorption efficiency of Cu_2O NCs/TiO_2 heterostructure, three times higher than shown by Cu_2O/TiO_2 reference, is partially ascribed to the difference among samples’ surface areas. Besides, Cu_2O nanocubes are composed of the most unsaturated low-index facets {100}, with the highest number of Cu(I) dangling bonds. Cu(I) sites were previously shown to be the active site for TC adsorption on Cu_2O. Therefore, the shape of Cu_2O in Cu_2O NCs/TiO_2 heterostructure also contributed to the efficiency of TC adsorption.

Concerning the photocatalytic tests, despite the visible light absorption provided by the Cu_2O NCs as evidenced by DRS, the Cu_2O NCs/TiO_2 heterostructure was found to be photocatalytically inactive for TC removal. This is a consequence of {100} Cu_2O facet effect that hinders the photogenerated charge carriers from reaching the Cu_2O NCs surface. Therefore, Cu_2O NCs/TiO_2 heterostructure is not capable to generate ROS under visible light, as evidenced by

EPR. Therefore, it can be inferred that Cu_2O NCs are inactive under visible light, even after grafting TiO_2 nanoparticles on their surface.

Finally, considering that the Cu_2O NCs/TiO_2 heterostructure exhibited a high TC adsorption capacity under the reported conditions, further research should be carried out to evaluate adsorption efficiency after many cycles of adsorption and for different adsorbent-to-TC ratios, aiming practical and large-scale applications in water treatment plants.

7.
General conclusions and prospects for future works

Throughout this study, different NiO/TiO_2 heterojunctions obtained by mechanochemical approach *via* BM and by a widely used conventional route, the IWI, were investigated. Additionally, a heterojunction between Cu_2O with {100} exposed facets and TiO_2, was investigated.

In the first study, it was found that the NiO/TiO_2 sample obtained by BM exhibited a predominant high-spin (HS) configuration of Ni^{2+} in NiO that proved to be particularly reactive, ultimately, with increased solar H_2 photoproduction efficiency.

Subsequent study using the EPR/spin trapping technique revealed that the sample obtained via BM also has the highest efficiency in superoxide and hydroxyl photogeneration, which are principal ROS. Thus, this study shed light on the NiO/TiO_2 p-n heterojunction obtained via BM as a potential catalyst with increased efficiency also for photodegradation of emerging organic pollutants.

Finally, the Cu_2O NCs/TiO_2 heterojunction demonstrated inactivity for tetracycline photodegradation. This feature was unveiled through tests in the presence and absence of visible light and in-situ ROS detection studies through EPR/spin-trapping. However, interestingly, due to a strong interaction of Cu(I) sites with the NH_2 group of the tetracycline molecule, the Cu_2O NCs/TiO_2 heterojunction demonstrated high efficiency in adsorptive removal of tetracycline.

Based on the results presented and discussed in the previous chapters and the general conclusions, the following suggestions emerge for future work:

- Investigation using the resonant inelastic X-ray scattering (RIXS) technique to gain further insights and deepen the understanding of the electronic transitions that influence the optical properties of NiO/TiO_2 heterojunctions;
- Through first principles studies, investigate the dynamics and mechanisms behind the generation of ROS (Reactive Oxygen Species) by NiO/TiO_2 heterojunctions;
- Conduct photodegradation tests on emerging organic pollutants, such as the drugs tetracycline and ibuprofen, as the results of EPR/spin-trapping suggest the NiO/TiO_2 heterojunctions reported here as an efficient source of superoxide and hydroxyl radicals;

- Controlled synthesis of tailored crystals with other low-index facets of Cu_2O, namely {111} and {101}, for experimental studies and first principles investigations of tetracycline removal by photodegradation and adsorption.

8.
References

ABUL-MAGD, A. A.; MORSHIDY, H. Y.; ABDEL-GHANY, A. M. The role of NiO on the structural and optical properties of sodium zinc borate glasses. **Optical Materials**, v. 109, 1 nov. 2020.

ADEYEMI, J. O.; AJIBOYE, T.; ONWUDIWE, D. C. Mineralization of Antibiotics in Wastewater Via Photocatalysis. **Water, Air, & Soil Pollution**, v. 232, n. 5, p. 219, 16 maio 2021.

AHMADIJOKANI, F.; MOLAVI, H.; TAJAHMADI, S.; REZAKAZEMI, M.; AMINI, M.; KAMKAR, M.; ROJAS, O. J.; ARJMAND, M. Coordination chemistry of metal–organic frameworks: Detection, adsorption, and photodegradation of tetracycline antibiotics and beyond. **Coordination Chemistry Reviews**, v. 464, p. 214562, 2022.

AL-GHOUTI, M. A.; DA’ANA, D. A. **Guidelines for the use and interpretation of adsorption isotherm models: A reviewJournal of Hazardous Materials**Elsevier B.V., , 5 jul. 2020.

ALMEIDA, L. A.; DOSEN, A.; VIOL, J.; MARINKOVIC, B. A. TiO2-Acetylacetone as an Efficient Source of Superoxide Radicals under Reduced Power Visible Light: Photocatalytic Degradation of Chlorophenol and Tetracycline. **Catalysts**, v. 12, n. 2, 2022a.

___. TiO2-Acetylacetone as an Efficient Source of Superoxide Radicals under Reduced Power Visible Light: Photocatalytic Degradation of Chlorophenol and Tetracycline. **Catalysts**, v. 12, n. 2, p. 116, 19 jan. 2022b.

ALMEIDA, L. A.; HABRAN, M.; SANTOS CARVALHO, R. DOS; MAIA DA COSTA, M. E. H.; CREMONA, M.; SILVA, B. C.; KRAMBROCK, K.; GINOBLE PANDOLI, O.; MORGADO JR., E.; MARINKOVIC, B. A. The Influence of Calcination Temperature on Photocatalytic Activity of TiO2-Acetylacetone Charge Transfer Complex towards Degradation of NOx under Visible Light. **Catalysts**, v. 10, n. 12, p. 1463, 14 dez. 2020.

AL-SAEEDI, S. I.; AL-SENANI, G. M.; ABD-ELKADER, O. H.; DERAZ, N. M. One pot synthesis, surface and magnetic properties of cu2o/cu and cu2o/cuo nanocomposites. **Crystals**, v. 11, n. 7, 1 jul. 2021.

ANSARI, S. A.; KHAN, M. M.; ANSARI, M. O.; CHO, M. H. Nitrogen-doped titanium dioxide (N-doped TiO2) for visible light photocatalysis. **New Journal of Chemistry**, v. 40, n. 4, p. 3000–3009, 2016.

ARENHOLZ, E.; LAAN, G. VAN DER; NOLTING, F. Magnetic structure near the CoNiO (001) interface. **Applied Physics Letters**, v. 93, n. 16, 2008.

ARIZA-TARAZONA, M. C.; VILLARREAL-CHIU, J. F.; BARBIERI, V.; SILIGARDI, C.; CEDILLO-GONZÁLEZ, E. I. New strategy for microplastic degradation: Green photocatalysis using a protein-based porous N-TiO 2 semiconductor. **Ceramics International**, v. 45, n. 7, p. 9618–9624, 2019.

ARMAROLI, N.; BALZANI, V. **The hydrogen issueChemSusChem**Wiley-VCH Verlag, , 17 jan. 2011.

ASAHI, R.; TAGA, Y.; MANNSTADT, W. Electronic and optical properties of anatase TiO2. **Physical Review B - Condensed Matter and Materials Physics**, v. 61, n. 11, p. 7459–7465, 2000.

ATKINS, P.; OVERTON, T.; ROURKE, J.; WELLER, M.; ARMSTRONG, F.; HAGERMAN, M. **Inorganic Chemistry**. Fifth ed. [s.l.] W.H. Freeman and Company, 2010.

BAČIĆ, G.; SPASOJEVIĆ, I.; ŠEĆEROV, B.; MOJOVIĆ, M. Spin-trapping of oxygen free radicals in chemical and biological systems: New traps, radicals and possibilities. **Spectrochimica Acta Part A: Molecular and Biomolecular Spectroscopy**, v. 69, n. 5, p. 1354–1366, maio 2008.

BAI, S.; WANG, L.; LI, Z.; XIONG, Y. Facet-Engineered Surface and Interface Design of Photocatalytic Materials. **Advanced Science**, v. 4, n. 1, 17 jan. 2017.

BASAVARAJAPPA, P. S.; PATIL, S. B.; GANGANAGAPPA, N.; REDDY, K. R.; RAGHU, A. V.; REDDY, C. V. Recent progress in metal-doped TiO2, non-metal doped/codoped TiO2 and TiO2 nanostructured hybrids for enhanced photocatalysis. **International Journal of Hydrogen Energy**, v. 45, n. 13, p. 7764–7778, mar. 2020.

BAYAT, F.; SHEIBANI, S. Enhancement of photocatalytic activity of CuO-Cu2O heterostructures through the controlled content of Cu2O. **Materials Research Bulletin**, v. 145, n. April 2021, p. 111561, 2022.

BISWAL, B. K.; BALASUBRAMANIAN, R. Adsorptive removal of sulfonamides, tetracyclines and quinolones from wastewater and water using carbon-based materials: Recent developments and future directions. **Journal of Cleaner Production**, v. 349, n. February, p. 131421, 2022.

BOLDYREV, V. V.; TKÁČOVÁ, K. Mechanochemistry of solids: Past, present, and prospects. **Journal of Materials Synthesis and Processing**, v. 8, n. 3–4, p. 121–132, 2000.

BRAGA, A.; ARMENGOL-PROFITÓS, M.; PASCUA-SOLÉ, L.; VENDRELL, X.; SOLER, L.; SERRANO, I.; VILLAR-GARCIA, I. J.; PÉREZ-DIESTE, V.; DIVINS, N. J.; LLORCA, J. Bimetallic NiFe Nanoparticles Supported on CeO2 as Catalysts for Methane Steam Reforming. **ACS Applied Nano Materials**, v. 6, n. 9, p. 7173–7185, 12 maio 2023.

BRASLAVSKY, S. E. Glossary of terms used in photochemistry 3rd edition: (IUPAC Recommendations 2006). **Pure and Applied Chemistry**, v. 79, n. 3, p. 293–465, 2007.

BRITO, J. F. DE; TAVELLA, F.; GENOVESE, C.; AMPELLI, C.; ZANONI, M. V. B.; CENTI, G.; PERATHONER, S. Role of CuO in the modification of the photocatalytic water splitting behavior of TiO2 nanotube thin films. **Applied Catalysis B: Environmental**, v. 224, p. 136–145, 1 maio 2018.

BURGHERR, P. In-depth analysis of accidental oil spills from tankers in the context of global spill trends from all sources. **Journal of Hazardous Materials**, v. 140, n. 1–2, p. 245–256, fev. 2007.

CAI, Y.; SHEN, S.; FAN, J. Enhanced degradation of tetracycline by Cu(II) complexation in the FeS/sulfite system. **Journal of Hazardous Materials**, v. 421, 5 jan. 2022.

CAO, Y.; XU, Y.; HAO, H.; ZHANG, G. Room temperature additive-free synthesis of uniform Cu2O nanocubes with tunable size from 20 nm to 500 nm and photocatalytic property. **Materials Letters**, v. 114, p. 88–91, 2014.

CARLA DE SANTANA DE LIMA, K.; MAGNO PAIVA, V.; GUSTAVO ARAUJO SCHWARZ, M.; MARTINS BOMFIM BARRETO, N.; PERRONE, D.; D'ELIA, E. The role of soybean meal extracts proteins in the inhibition of mild steel acid corrosion. **Sustainable Chemistry and Pharmacy**, v. 35, 1 out. 2023.

CASTAÑEDA, C.; MARTÍNEZ, J. J.; SANTOS, L.; ROJAS, H.; OSMAN, S. M.; GÓMEZ, R.; LUQUE, R. Caffeine photocatalytic degradation using composites of NiO/TiO2–F and CuO/TiO2–F under UV irradiation. **Chemosphere**, v. 288, p. 132506, fev. 2022.

CHANG, I. C.; CHEN, P. C.; TSAI, M. C.; CHEN, T. T.; YANG, M. H.; CHIU, H. T.; LEE, C. Y. Large-scale synthesis of uniform Cu2O nanocubes with tunable sizes by in-situ nucleation. **CrystEngComm**, v. 15, n. 13, p. 2363–2366, 7 abr. 2013.

CHEN, C.-J.; LIAO, C.-H.; HSU, K.-C.; WU, Y.-T.; WU, J. C. S. P–N junction mechanism on improved NiO/TiO2 photocatalyst. **Catalysis Communications**, v. 12, n. 14, p. 1307–1310, ago. 2011.

CHEN, X.; MAO, S. S. Titanium dioxide nanomaterials: Synthesis, properties, modifications and applications. **Chemical Reviews**, v. 107, n. 7, p. 2891–2959, 2007.

CHEN, X.; SHEN, S.; GUO, L.; MAO, S. S. Semiconductor-based photocatalytic hydrogen generation. **Chemical Reviews**, v. 110, n. 11, p. 6503–6570, 2010.

CHEN, Y.; SOLER, L.; ARMENGOL-PROFITÓS, M.; XIE, C.; CRESPO, D.; LLORCA, J. Enhanced photoproduction of hydrogen on Pd/TiO2 prepared by mechanochemistry. **Applied Catalysis B: Environmental**, v. 309, 2022.

CHEN, Y.; SOLER, L.; CAZORLA, C.; OLIVERAS, J.; BASTÚS, N. G.; PUNTES, V. F.; LLORCA, J. Facet-engineered TiO2 drives photocatalytic activity and stability of supported noble metal clusters during H2 evolution. **Nature Communications**, v. 14, n. 1, p. 6165, 3 out. 2023.

CHEN, Y.; SOLER, L.; XIE, C.; VENDRELL, X.; SERAFIN, J.; CRESPO, D.; LLORCA, J. A straightforward method to prepare supported Au clusters by mechanochemistry and its application in photocatalysis. **Applied Materials Today**, v. 21, p. 100873, 2020a.

___. A straightforward method to prepare supported Au clusters by mechanochemistry and its application in photocatalysis. **Applied Materials Today**, v. 21, p. 100873, 2020b.

CHEN, Z.; MU, D.; CHEN, F.; TAN, N. NiFe2O4@ nitrogen-doped carbon hollow spheres with highly efficient and recyclable adsorption of tetracycline. **RSC Advances**, v. 9, n. 19, p. 10445–10453, 2019.

CHENG, X.-M.; ZHAO, J.; SUN, W.-Y. Facet-Engineering of Materials for Photocatalytic Application: Status and Future Prospects. **EnergyChem**, v. 4, n. 5, p. 100084, set. 2022.

CHU, C. Y.; HUANG, M. H. Facet-dependent photocatalytic properties of Cu2O crystals probed by using electron, hole and radical scavengers. **Journal of Materials Chemistry A**, v. 5, n. 29, p. 15116–15123, 2017.

COLMENARES, J.; XU, Y.-J. **Heterogeneous Photocatalysis: From Fundamentals to Green Applications**. [s.l.] Springer, 2016.

COLÓN, G. Towards the hydrogen production by photocatalysis. **Applied Catalysis A: General**, v. 518, p. 48–59, 2016.

COUTO-PESSANHA, E.; PAIVA, V.; MORI, T.; SOLER, L.; CANABARRO, B.; JARDIM, P.; D'ELIA, E.; LLORCA, J.; MARINKOVIC, B. **Mechanochemical approach towards optimized Ni2+ spin configuration in NiO/TiO2 heterojunction with enhanced solar-driven H2 photoproduction**, 2024.

DAMBOURNET, D.; BELHAROUAK, I.; AMINE, K. Tailored preparation methods of TiO2 anatase, rutile, brookite: Mechanism of formation and electrochemical properties. **Chemistry of Materials**, v. 22, n. 3, p. 1173–1179, 2010.

DANIELIS, M.; BETANCOURT, L. E.; OROZCO, I.; DIVINS, N. J.; LLORCA, J.; RODRÍGUEZ, J. A.; SENANAYAKE, S. D.; COLUSSI, S.; TROVARELLI, A. Methane oxidation activity and nanoscale characterization of Pd/CeO2 catalysts prepared by dry milling Pd acetate and ceria. **Applied Catalysis B: Environmental**, v. 282, 1 mar. 2021.

DANIELIS, M.; COLUSSI, S.; DIVINS, N. J.; SOLER, L.; TROVARELLI, A.; LLORCA, J. Mechanochemistry: A Green and Fast Method to Prepare A New Generation of Metal Supported Catalysts. **Johnson Matthey Technology Review**, 2023.

DANIELIS, M.; COLUSSI, S.; LEITENBURG, C. DE; SOLER, L.; LLORCA, J.; TROVARELLI, A. Outstanding Methane Oxidation Performance of Palladium-Embedded Ceria Catalysts Prepared by a One-Step Dry Ball-Milling Method. **Angewandte Chemie - International Edition**, v. 57, n. 32, p. 10212–10216, 6 ago. 2018.

DELL'EDERA, M.; PORTO, C. LO; PASQUALE, I. DE; PETRONELLA, F.; CURRI, M. L.; AGOSTIANO, A.; COMPARELLI, R. Photocatalytic TiO2-based coatings for environmental applications. **Catalysis Today**, v. 380, n. May, p. 62–83, 2021.

DENG, J.; LV, X.; LIU, J.; ZHANG, H.; NIE, K.; HONG, C.; WANG, J.; SUN, X.; ZHONG, J.; LEE, S. T. Thin-layer Fe2TiO5 on hematite for efficient solar water oxidation. **ACS Nano**, v. 9, n. 5, p. 5348–5356, 26 maio 2015.

DING, J. *et al.* Atomic high-spin cobalt(II) center for highly selective electrochemical CO reduction to CH3OH. **Nature Communications**, v. 14, n. 1, 1 dez. 2023.

DING, Y.; WANG, MENGYING; MEI, Z.; LIU, L.; YANG, J.; ZHONG, X.; WANG, MEI; DIAO, X. Electrochromic Adaptability of NiOx Films Modified by Substrate Temperature in Aqueous and Non-Aqueous Electrolytes. **Advanced Materials Interfaces**, v. 9, n. 17, 1 jun. 2022.

DÖRR, T. S.; DEILMANN, L.; HASELMANN, G.; CHEREVAN, A.; ZHANG, P.; BLAHA, P.; OLIVEIRA, P. W. DE; KRAUS, T.; EDER, D. Ordered Mesoporous TiO2 Gyroids: Effects of Pore Architecture and Nb-Doping on Photocatalytic Hydrogen Evolution under UV and Visible Irradiation. **Advanced Energy Materials**, v. 8, n. 36, 27 dez. 2018.

DURANGO-CORDERO, J.; SAQALLI, M.; LAPLANCHE, C.; LOCQUET, M.; ELGER, A. Spatial Analysis of Accidental Oil Spills Using Heterogeneous Data: A Case Study from the North-Eastern Ecuadorian Amazon. **Sustainability**, v. 10, n. 12, p. 4719, 11 dez. 2018.

DUTTA, S. **Review on Solar Hydrogen: Its Prospects and LimitationsEnergy and Fuels**American Chemical Society, , 5 ago. 2021.

EABORN, C. Compendium of chemical Terminology: IUPAC Recommendations. **Journal of Organometallic Chemistry**, v. 356, n. 2, p. C76–C77, 1988.

EGBO, K. O.; LIU, C. P.; EKUMA, C. E.; YU, K. M. Vacancy defects induced changes in the electronic and optical properties of NiO studied by spectroscopic ellipsometry and first-principles calculations. **Journal of Applied Physics**, v. 128, n. 13, 7 out. 2020.

EISAPOUR, M.; ZHAO, H.; ZHAO, J.; ROOSTAEI, T.; LI, Z.; OMIDKAR, A.; HU, J.; CHEN, Z. p-n heterojunction of nickel oxide on titanium dioxide nanosheets for hydrogen and value-added chemicals coproduction from glycerol photoreforming. **Journal of Colloid and Interface Science**, v. 647, p. 255–263, 1 out. 2023.

FAISAL, M.; HARRAZ, F. A.; ISMAIL, A. A.; EL-TONI, A. M.; AL-SAYARI, S. A.; AL-HAJRY, A.; AL-ASSIRI, M. S. Novel mesoporous NiO/TiO2 nanocomposites with enhanced photocatalytic activity under visible light illumination. **Ceramics International**, v. 44, n. 6, p. 7047–7056, 15 abr. 2018.

FARCY, A.; MAHY, J. G.; ALIÉ, C.; CAUCHETEUX, J.; POELMAN, D.; YANG, Z.; ELOY, P.; BODY, N.; HERMANS, S.; HEINRICHS, B.; LAMBERT, S. D. Kinetic study of p-nitrophenol degradation with zinc oxide nanoparticles prepared by sol–gel methods. **Journal of Photochemistry and Photobiology A: Chemistry**, v. 456, p. 115804, nov. 2024.

FAZLIKESHTELI, S.; VENDRELL, X.; LLORCA, J. Bimetallic Ru–Pd supported on CeO2 for the catalytic partial oxidation of methane into syngas. **Fuel**, v. 334, 15 fev. 2023a.

___. Low-temperature partial oxidation of methane over Pd–Ni bimetallic catalysts supported on CeO2. **International Journal of Hydrogen Energy**, v. 48, n. 32, p. 12024–12035, 15 abr. 2023b.

FELIU, S. **Electrochemical impedance spectroscopy for the measurement of the corrosion rate of magnesium alloys: Brief review and challengesMetals**MDPI AG, , 1 jun. 2020.

FERREIRA, R. M. *et al.* Facile Gram-Scale Synthesis of NiO Nanoflowers for Highly Selective and Sensitive Electrocatalytic Detection of Hydrazine. **ACS Omega**, v. 8, n. 13, p. 11978–11986, 4 abr. 2023.

FERRER, M. M.; FABRIS, G. S. L.; FARIA, B. V. DE; MARTINS, J. B. L.; MOREIRA, M. L.; SAMBRANO, J. R. Quantitative evaluation of the surface stability and morphological changes of Cu2O particles. **Heliyon**, v. 5, n. 10, 1 out. 2019.

FUENTES, S.; TAPIA, A.; POZO, P. Synthesis, characterization, and antibacterial activity evaluation of Cu@TiO2 nanocomposites. **Materials Letters**, v. 296, p. 129885, 2021.

FUJISHIMA, A.; HONDA, K. Electrochemical photolysis of water at a semiconductor electrode. **Nature**, v. 238, p. 37–38, 1972.

FUJISHIMA, A.; HONDA, K. Electrochemical Photolysis of Water at a Semiconductor Electrode. **Nature**, v. 238, n. 5358, p. 37–38, jul. 1972.

FUJISHIMA, A.; ZHANG, X.; TRYK, D. A. TiO2 photocatalysis and related surface phenomena. **Surface Science Reports**, v. 63, n. 12, p. 515–582, 2008.

GAO, L.; PANG, C.; HE, D.; SHEN, L.; GUPTA, A.; BAO, N. Synthesis of Hierarchical Nanoporous Microstructures via the Kirkendall Effect in Chemical Reduction Process. **Scientific Reports**, v. 5, 10 nov. 2015.

GAO, W.; ZHANG, L. Nanomaterials arising amid antibiotic resistance. **Nature Reviews Microbiology**, v. 19, n. 1, p. 5–6, 2021.

GARCÍA-LÓPEZ, E.; PALMISANO, L. **Materials Science in Photocatalysis**. 1st. ed. Amsterdam: Elsevier, 2021.

GE, S.; CHEN, Y.; GUO, Y.; LLORCA, J.; SOLER, L. Mechanochemically activated Au/CeO2 for enhanced CO oxidation and COPrOx reaction. **Applied Materials Today**, v. 33, 1 ago. 2023.

GIL-LONDOÑO, J.; CREMONA, M.; KRAMBROCK, K.; COSTA, M. E. H. M. DA; ALMEIDA, L. A.; MARINKOVIC, B. A. Functionalization of anatase nanoparticles with Glutaric acid and their photochemical and photocatalytic properties under visible light. **Ceramics International**, fev. 2023.

GIL-LONDOÑO, J.; KRAMBROCK, K.; OLIVEIRA, R. DE; CREMONA, M.; MAIA DA COSTA, M. E. H.; MARINKOVIC, B. A. Extrinsic Point Defects in TiO2-Acetylacetone Charge-Transfer Complex and Their Effects on Optical and Photochemical Properties. **Inorganic Chemistry**, 2022.

GIL-LONDOÑO, J.; KRAMBROCK, K.; OLIVEIRA, R. DE; CREMONA, M.; MAIA DA COSTA, M. E. H.; MARINKOVIC, B. A. Extrinsic Point Defects in TiO2 –Acetylacetone Charge-Transfer Complex and Their Effects on Optical and Photochemical Properties. **Inorganic Chemistry**, v. 62, n. 5, p. 2273–2288, 6 fev. 2023.

GIROLAMO, D. DI; GIACOMO, F. DI; MATTEOCCI, F.; MARRANI, A. G.; DINI, D.; ABATE, A. **Progress, highlights and perspectives on NiO in perovskite photovoltaicsChemical Science**Royal Society of Chemistry, , 14 ago. 2020.

GOMOLLÓN-BEL, F. Ten Chemical Innovations That Will Change Our World. **Chemistry International**, v. 42, n. 4, p. 3–9, 2020.

GONDAL, M. A.; SALEH, T. A.; DRMOSH, Q. A. Synthesis of nickel oxide nanoparticles using pulsed laser ablation in liquids and their optical characterization. **Applied Surface Science**, v. 258, n. 18, p. 6982–6986, jul. 2012.

GONG, Y.; ZHANG, S.; GAO, H.; MA, Z.; HU, S.; TAN, Z. **Recent advances and comprehensive insights on nickel oxide in emerging**

optoelectronic devicesSustainable Energy and Fuels Royal Society of Chemistry, , 1 set. 2020.

GROOT, F. DE. Multiplet effects in X-ray spectroscopy. **Coordination Chemistry Reviews**, v. 249, n. 1–2, p. 31–63, jan. 2005.

GROOT, F. DE; KOTANI, A. **Core Level Spectroscopy of Solids**. [s.l.] CRC Press, 2008.

GROOT, F. M. F. DE *et al.* **2p x-ray absorption spectroscopy of 3d transition metal systemsJournal of Electron Spectroscopy and Related Phenomena**Elsevier B.V., , 1 maio 2021.

GUO, Q.; ZHOU, C.; MA, Z.; YANG, X. Fundamentals of TiO2 Photocatalysis: Concepts, Mechanisms, and Challenges. **Advanced Materials**, v. 31, n. 50, p. 1–26, 2019.

HABIBI-YANGJEH, A.; ASADZADEH-KHANEGHAH, S.; FEIZPOOR, S.; ROUHI, A. Review on heterogeneous photocatalytic disinfection of waterborne, airborne, and foodborne viruses: Can we win against pathogenic viruses? **Journal of Colloid and Interface Science**, v. 580, p. 503–514, 2020.

HABRAN, M.; KRAMBROCK, K.; MAIA DA COSTA, M. E. H.; MORGADO, E.; MARINKOVIC, B. A. TiO2 anatase nanorods with non-equilibrium crystallographic {001} facets and their coatings exhibiting high photo-oxidation of NO gas. **Environmental Technology (United Kingdom)**, v. 39, n. 2, p. 231–239, 2018.

HABRAN, M.; PONTÓN, P. I.; MANCIC, L.; PANDOLI, O.; KRAMBROCK, K.; COSTA, M. E. H. M. DA; LETICHEVSKY, S.; COSTA, A. M. L. M.; MORGADO, E.; MARINKOVIC, B. A. Visible light sensitive mesoporous nanohybrids of lepidocrocite-like ferrititanate coupled to a charge transfer complex: Synthesis, characterization and photocatalytic degradation of NO. **Journal of Photochemistry and Photobiology A: Chemistry**, v. 365, p. 133–144, 1 out. 2018.

HASHIMOTO, K.; IRIE, H.; FUJISHIMA, A. TiO2 photocatalysis: A historical overview and future prospects. **Japanese Journal of Applied Physics, Part 1: Regular Papers and Short Notes and Review Papers**, v. 44, n. 12, p. 8269–8285, 2005.

HAVERKORT, M. W.; ZWIERZYCKI, M.; ANDERSEN, O. K. Multiplet ligand-field theory using Wannier orbitals. **Physical Review B - Condensed Matter and Materials Physics**, v. 85, n. 16, 9 abr. 2012.

HISATOMI, T.; KUBOTA, J.; DOMEN, K. **Recent advances in semiconductors for photocatalytic and photoelectrochemical water splittingChemical Society Reviews**Royal Society of Chemistry, , 21 nov. 2014.

HOLDER, C. F.; SCHAAK, R. E. **Tutorial on Powder X-ray Diffraction for Characterizing Nanoscale MaterialsACS Nano**American Chemical Society, , 23 jul. 2019.

HÖÖK, M.; TANG, X. Depletion of fossil fuels and anthropogenic climate change-A review. **Energy Policy**, v. 52, p. 797–809, jan. 2013.

HOU, L.; LI, S.; LIN, Y.; WANG, D.; XIE, T. Photogenerated charges transfer across the interface between NiO and TiO2 nanotube arrays for photocatalytic degradation: A surface photovoltage study. **Journal of Colloid and Interface Science**, v. 464, p. 96–102, 15 fev. 2016.

HU, Y.; LI, B.; YU, C.; FANG, H.; LI, Z. Mechanochemical preparation of single atom catalysts for versatile catalytic applications: A perspective review. **Materials Today**, v. 63, p. 288–312, mar. 2023.

HUSSEIN, G. A. M.; NOHMAN, A. K. H.; ATTYIA, K. M. A. Characterization of the decomposition course of nickel acetate tetrahydrate in air. **Journal of Thermal Analysis**, v. 42, n. 6, p. 1155–1165, dez. 1994.

IBRAHIM, Q.; CREEDON, L.; GHARBIA, S. A Literature Review of Modelling and Experimental Studies of Water Treatment by Adsorption Processes on Nanomaterials. **Membranes**, v. 12, n. 4, 2022.

ITALIANO, C.; LLORCA, J.; PINO, L.; FERRARO, M.; ANTONUCCI, V.; VITA, A. CO and CO2 methanation over Ni catalysts supported on CeO2, Al2O3 and Y2O3 oxides. **Applied Catalysis B: Environmental**, v. 264, 5 maio 2020.

JAMES, S. L. *et al.* Mechanochemistry: opportunities for new and cleaner synthesis. **Chemical Society Reviews**, v. 41, n. 1, p. 413–447, 2012.

JANCZAREK, M.; KOWALSKA, E. On the origin of enhanced photocatalytic activity of copper-modified titania in the oxidative reaction systems. **Catalysts**, v. 7, n. 11, 2017.

JASIM, M. M.; AZEEZ DAKHIL, O. A.; ABDULLAH, H. I. Synthesis of NiO/TNTs p-n junction for highly photocatalysis activity under sunlight irradiation. **Solid State Sciences**, v. 107, 1 set. 2020.

JIANG, C.; MONIZ, S. J. A.; WANG, A.; ZHANG, T.; TANG, J. **Photoelectrochemical devices for solar water splitting-materials and challengesChemical Society Reviews**Royal Society of Chemistry, , 7 ago. 2017.

JITAN, S. AL; PALMISANO, G.; GARLISI, C. Synthesis and Surface Modification of TiO2-Based Photocatalysts for the Conversion of CO2. **Catalysts**, v. 10, n. 2, p. 227, 14 fev. 2020.

KABIR, E.; KUMAR, P.; KUMAR, S.; ADELODUN, A. A.; KIM, K. H. **Solar energy: Potential and future prospectsRenewable and Sustainable Energy Reviews**Elsevier Ltd, , 2018.

KANG, Z.; JIA, X.; ZHANG, Y.; KANG, X.; GE, M.; LIU, D.; WANG, C.; HE, Z. A Review on Application of Biochar in the Removal of Pharmaceutical Pollutants through Adsorption and Persulfate-Based AOPs. **Sustainability**, v. 14, n. 16, p. 10128, 2022.

KHALID, N. R.; MAJID, A.; TAHIR, M. B.; NIAZ, N. A.; KHALID, S. Carbonaceous-TiO2 nanomaterials for photocatalytic degradation of pollutants: A review. **Ceramics International**, v. 43, n. 17, p. 14552–14571, 2017.

KIM, J. H.; HANSORA, D.; SHARMA, P.; JANG, J. W.; LEE, J. S. **Toward practical solar hydrogen production-an artificial photosynthetic leaf-to-farm challengeChemical Society Reviews**Royal Society of Chemistry, , 7 abr. 2019.

KIM, J.; YU, J.; LEE, S.; TAHMASEBI, A.; JEON, C. H.; LUCAS, J. **Advances in catalytic hydrogen combustion research: Catalysts, mechanism, kinetics, and reactor designsInternational Journal of Hydrogen Energy**Elsevier Ltd, , 18 nov. 2021.

KISCH, H.; MACYK, W. Visible-Light Photocatalysis by Modified Titania. **ChemPhysChem**, v. 3, n. 5, p. 399, 17 maio 2002.

KITCHAMSETTI, N.; RAMTEKE, M. S.; RONDIYA, S. R.; MULANI, S. R.; PATIL, M. S.; CROSS, R. W.; DZADE, N. Y.; DEVAN, R. S. DFT and experimental investigations on the photocatalytic activities of NiO nanobelts for removal of organic pollutants. **Journal of Alloys and Compounds**, v. 855, 25 fev. 2021.

KOHTANI, S.; KAWASHIMA, A.; MIYABE, H. Reactivity of trapped and accumulated electrons in titanium dioxide photocatalysis. **Catalysts**, v. 7, n. 10, 2017.

KROL, R.; GRÄTZEL, M. **Photoelectrochemical Hydrogen Production**. [s.l: s.n.].

KRONAWITTER, C. X.; KAPILASHRAMI, M.; BAKKE, J. R.; BENT, S. F.; CHUANG, C. H.; PONG, W. F.; GUO, J.; VAYSSIERES, L.; MAO, S. S. TiO 2-SnO 2:F interfacial electronic structure investigated by soft x-ray absorption spectroscopy. **Physical Review B - Condensed Matter and Materials Physics**, v. 85, n. 12, 9 mar. 2012.

KUCHEYEV, S. O.; BUUREN, T. VAN; BAUMANN, T. F.; SATCHER, J. H.; WILLEY, T. M.; MEULENBERG, R. W.; FELTER, T. E.; POCO, J. F.; GAMMON, S. A.; TERMINELLO, L. J. Electronic structure of titania aerogels from soft x-ray absorption spectroscopy. **Physical Review B - Condensed Matter and Materials Physics**, v. 69, n. 24, jun. 2004.

KUMAR TRIVEDI, M. Spectroscopic Characterization of Chloramphenicol and Tetracycline: An Impact of Biofield Treatment. **Pharmaceutica Analytica Acta**, v. 06, n. 07, 2015.

LAAN, G. VAN DER. **Polaronic satellites in x-ray-absorption spectraPHYSICAL REVIEW B**. [s.l: s.n.].

LAAN, G. VAN DER; ZAANEN, J.; SAWATZKY, G. A.; KARNATAK, R.; ESTEVA, J.-M. **Comparison of x-ray absorption with x-ray photoemission of nickel dihalides and NioPHYSICAL REVIE%**. [s.l: s.n.].

LAN, D.; PANG, F.; GE, J. Enhanced Charge Separation in NiO and Pd Co-Modified TiO2Photocatalysts for Efficient and Selective Photoreduction of CO2. **ACS Applied Energy Materials**, 2021.

LARSSON, D. G. J.; FLACH, C. F. Antibiotic resistance in the environment. **Nature Reviews Microbiology**, v. 20, n. May, p. 257–269, 2021.

LEE, S. F.; JIMENEZ-RELINQUE, E.; MARTINEZ, I.; CASTELLOTE, M. Effects of Mott–Schottky Frequency Selection and Other Controlling Factors on Flat-Band Potential and Band-Edge Position Determination of TiO2. **Catalysts**, v. 13, n. 6, 1 jun. 2023.

LEI, Y. *et al.* Engineering defect-rich Fe-doped NiO coupled Ni cluster nanotube arrays with excellent oxygen evolution activity. **Applied Catalysis B: Environmental**, v. 285, 15 maio 2021.

LEICHTWEIS, J.; VIEIRA, Y.; WELTER, N.; SILVESTRI, S.; DOTTO, G. L.; CARISSIMI, E. A review of the occurrence, disposal, determination, toxicity and remediation technologies of the tetracycline antibiotic. **Process Safety and Environmental Protection**, v. 160, p. 25–40, 2022.

LETTIERI, S.; PAVONE, M.; FIORAVANTI, A.; AMATO, L. S.; MADDALENA, P. Charge carrier processes and optical properties in TiO2 and TiO2-based heterojunction photocatalysts: A review. **Materials**, v. 14, n. 7, 2021.

LI, G.; HUANG, J.; CHEN, J.; DENG, Z.; HUANG, Q.; LIU, Z.; GUO, W.; CAO, R. Highly Active Photocatalyst of Cu 2 O/TiO 2 Octahedron for Hydrogen Generation. **ACS Omega**, v. 4, n. 2, p. 3392–3397, 14 fev. 2019.

LI, G.; ZHANG, H.; HAN, Y. **Applications of Transmission Electron Microscopy in Phase Engineering of NanomaterialsChemical reviews**NLM (Medline), , 13 set. 2023.

LI, H.; ZHOU, Y.; TU, W.; YE, J.; ZOU, Z. State-of-the-art progress in diverse heterostructured photocatalysts toward promoting photocatalytic performance. **Advanced Functional Materials**, v. 25, n. 7, p. 998–1013, 2015.

LI, N.-B.; SUN, S.-J.; BAI, H.-Y.; -, AL; MA, M.; MANSOUR, A. N.; KO, J. K. **Ti 2p X-ray absorption in titanium dioxides (TiO 2): the influence of the cation site environmentJ. Phys.: Condens. Matter**. [s.l: s.n.].

LI, S. *et al.* Tuning the Selectivity of Catalytic Carbon Dioxide Hydrogenation over Iridium/Cerium Oxide Catalysts with a Strong Metal–Support Interaction. **Angewandte Chemie - International Edition**, v. 56, n. 36, p. 10761–10765, 28 ago. 2017.

LI, X.; YU, J.; JARONIEC, M.; CHEN, X. Cocatalysts for selective photoreduction of CO2 into solar fuels. **Chemical Reviews**, v. 119, n. 6, p. 3962–4179, 2019.

LI, X.; ZHANG, L.; YANG, Z.; WANG, P.; YAN, Y.; RAN, J. Adsorption materials for volatile organic compounds (VOCs) and the key factors for VOCs adsorption process: A review. **Separation and Purification Technology**, v. 235, 18 mar. 2020.

LI, ZILIANG; LI, ZIQING; ZUO, C.; FANG, X. Application of Nanostructured TiO2 in UV Photodetectors: A Review. **Advanced Materials**, v. 34, n. 28, p. 1–43, 2022.

LIAN, Z.; TAO, Y.; LIU, Y.; ZHANG, Y.; ZHU, Q.; LI, G.; LI, H. Efficient Self-Driving Photoelectrocatalytic Reactor for Synergistic Water Purification and H2Evolution. **ACS Applied Materials and Interfaces**, v. 12, n. 40, p. 44731–44742, 7 out. 2020.

LIAO, H.; WANG, Z. Adsorption removal of amaranth by nanoparticles-composed Cu2O microspheres. **Journal of Alloys and Compounds**, v. 769, p. 1088–1095, 2018.

LIN, J.; SHEN, J.; WANG, R.; CUI, J.; ZHOU, W.; HU, P.; LIU, D.; LIU, H.; WANG, J.; BOUGHTON, R. I.; YUE, Y. Nano-p–n junctions on surface-coarsened TiO2 nanobelts with enhanced photocatalytic activity. **Journal of Materials Chemistry**, v. 21, n. 13, p. 5106, 2011.

LIU, J.; LI, Y.; KE, J.; WANG, S.; WANG, L.; XIAO, H. Black NiO-TiO2 nanorods for solar photocatalysis: Recognition of electronic structure and reaction mechanism. **Applied Catalysis B: Environmental**, v. 224, p. 705–714, maio 2018a.

___. Black NiO-TiO2 nanorods for solar photocatalysis: Recognition of electronic structure and reaction mechanism. **Applied Catalysis B: Environmental**, v. 224, p. 705–714, 1 maio 2018b.

LIU, L.; JI, Z.; ZOU, W.; GU, X.; DENG, Y.; GAO, F.; TANG, C.; DONG, L. In situ loading transition metal oxide clusters on TiO2 nanosheets as co-catalysts for exceptional high photoactivity. **ACS Catalysis**, v. 3, n. 9, p. 2052–2061, 6 set. 2013.

LÓPEZ-FONSECA, R.; JIMÉNEZ-GONZÁLEZ, C.; RIVAS, B. DE; GUTIÉRREZ-ORTIZ, J. I. Partial oxidation of methane to syngas on bulk NiAl 2O 4 catalyst. Comparison with alumina supported nickel, platinum and rhodium catalysts. **Applied Catalysis A: General**, v. 437–438, p. 53–62, 26 set. 2012.

LOW, J.; YU, J.; JARONIEC, M.; WAGEH, S.; AL-GHAMDI, A. A. Heterojunction Photocatalysts. **Advanced Materials**, v. 29, n. 20, 2017.

LUCENTINI, I.; CASANOVAS, A.; LLORCA, J. Catalytic ammonia decomposition for hydrogen production on Ni, Ru and Ni[sbnd]Ru supported on

CeO2. **International Journal of Hydrogen Energy**, v. 44, n. 25, p. 12693–12707, 17 maio 2019.

LUO, Y.; LEE, H. Present and Future of Phase-Selectively Disordered Blue TiO2 for Energy and Society Sustainability. **Nano-Micro Letters**, v. 13, n. 1, p. 1–13, 2021.

LUTTRELL, T.; HALPEGAMAGE, S.; TAO, J.; KRAMER, A.; SUTTER, E.; BATZILL, M. Why is anatase a better photocatalyst than rutile? - Model studies on epitaxial TiO2 films. **Scientific Reports**, v. 4, p. 1–8, 2015.

MA, D.; CAO, Z. Adsorption and Decomposition of Sarin on Dry and Wet Cu2O(111) and CuO(111) Surfaces: Insight from First-Principles Calculations. **Journal of Physical Chemistry C**, v. 125, n. 44, p. 24396–24405, 2021.

MA, Y.; WANG, X.; JIA, Y.; CHEN, X.; HAN, H.; LI, C. Titanium dioxide-based nanomaterials for photocatalytic fuel generations. **Chemical Reviews**, v. 114, n. 19, p. 9987–10043, 2014.

MANNAA, M. A.; QASIM, K. F.; ALSHORIFI, F. T.; EL-BAHY, S. M.; SALAMA, R. S. Role of NiO Nanoparticles in Enhancing Structure Properties of TiO2and Its Applications in Photodegradation and Hydrogen Evolution. **ACS Omega**, v. 6, n. 45, p. 30386–30400, 16 nov. 2021.

MANNU, A.; PIETRO, M. E. DI; MELE, A. Band-gap energies of choline chloride and triphenylmethylphosphoniumbromide-based systems. **Molecules**, v. 25, n. 7, p. 1–11, 2020.

MARTINS, P. M.; FERREIRA, C. G.; SILVA, A. R.; MAGALHÃES, B.; ALVES, M. M.; PEREIRA, L.; MARQUES, P. A. A. P.; MELLE-FRANCO, M.; LANCEROS-MÉNDEZ, S. TiO2/graphene and TiO2/graphene oxide nanocomposites for photocatalytic applications: A computer modeling and experimental study. **Composites Part B: Engineering**, v. 145, n. November 2017, p. 39–46, 2018.

MATSUURA, R. *et al.* SARS-CoV-2 Disinfection of Air and Surface Contamination by TiO2 Photocatalyst-Mediated Damage to Viral Morphology, RNA, and Protein. **Viruses**, v. 13, n. 5, p. 942, 20 maio 2021.

MAZURKÓW, J. M.; KUSIOR, A.; RADECKA, M. Electrochemical Characterization of Modified Glassy Carbon Electrodes for Non-Enzymatic Glucose Sensors. **Sensors**, v. 21, n. 23, p. 7928, 27 nov. 2021.

MESSAADIA, L.; KIAMOUCHE, S.; LAHMAR, H.; MASMOUDI, R.; BOULAHBEL, H.; TRARI, M.; BENAMIRA, M. Solar photodegradation of Rhodamine B dye by Cu2O/TiO2 heterostructure: experimental and computational studies of degradation and toxicity. **Journal of Molecular Modeling**, v. 29, n. 2, 1 fev. 2023.

MIESSLER, G.; FISCHER, P.; TARR, D. **Inorganic chemistry**. Fifth ed. [s.l.] PEARSON, 2014.

MOJET, B. L.; EBBESEN, S. D.; LEFFERTS, L. Light at the interface: the potential of attenuated total reflection infrared spectroscopy for understanding heterogeneous catalysis in water. **Chemical Society Reviews**, v. 39, n. 12, p. 4643, 2010a.

___. Light at the interface: The potential of attenuated total reflection infrared spectroscopy for understanding heterogeneous catalysis in water. **Chemical Society Reviews**, v. 39, n. 12, p. 4643–4655, 16 nov. 2010b.

MOORES, A. **Bottom up, solid-phase syntheses of inorganic nanomaterials by mechanochemistry and agingCurrent Opinion in Green and Sustainable Chemistry**Elsevier B.V., , 1 ago. 2018.

MORGADO, E.; MARINKOVIC, B. A.; JARDIM, P. M.; ABREU, M. A. S. DE; RIZZO, F. C. Characterization and thermal stability of cobalt-modified 1-D nanostructured trititanates. **Journal of Solid State Chemistry**, v. 182, n. 1, p. 172–181, jan. 2009.

MOSSANEK, R. J. O.; PREDA, I.; ABBATE, M.; RUBIO-ZUAZO, J.; CASTRO, G. R.; VOLLMER, A.; GUTIÉRREZ, A.; SORIANO, L. Investigation of surface and non-local screening effects in the Ni 2p core level photoemission spectra of NiO. **Chemical Physics Letters**, v. 501, n. 4–6, p. 437–441, 7 jan. 2011.

NAH, Y. C.; PARAMASIVAM, I.; SCHMUKI, P. Doped TiO2 and TiO2 nanotubes: Synthesis and applications. **ChemPhysChem**, v. 11, n. 13, p. 2698–2713, 2010.

NAKANO, R.; YAMAGUCHI, A.; SUNADA, K.; NAGAI, T.; NAKANO, A.; SUZUKI, Y.; YANO, H.; ISHIGURO, H.; MIYAUCHI, M. Inactivation of various variant types of SARS-CoV-2 by indoor-light-sensitive TiO2-based photocatalyst. **Scientific Reports**, v. 12, n. 1, p. 1–10, 2022.

NAKATA, K.; FUJISHIMA, A. TiO2 photocatalysis: Design and applications. **Journal of Photochemistry and Photobiology C: Photochemistry Reviews**, v. 13, n. 3, p. 169–189, 2012.

NARDI, G.; MANET, I.; MONTI, S.; MIRANDA, M. A.; LHIAUBET-VALLET, V. Scope and limitations of the TEMPO/EPR method for singlet oxygen detection: the misleading role of electron transfer. **Free Radical Biology and Medicine**, v. 77, p. 64–70, dez. 2014.

NAVIDPOUR, A. H.; ABBASI, S.; LI, D.; MOJIRI, A.; ZHOU, J. L. **Investigation of Advanced Oxidation Process in the Presence of TiO2 Semiconductor as Photocatalyst: Property, Principle, Kinetic Analysis, and Photocatalytic ActivityCatalysts**MDPI, , 1 fev. 2023.

NUNES, D.; PIMENTEL, A.; BRANQUINHO, R.; FORTUNATO, E.; MARTINS, R. Metal oxide-based photocatalytic paper: A green alternative for environmental remediation. **Catalysts**, v. 11, n. 4, 2021.

OLIVEIRA, P. F. M. DE; TORRESI, R. M.; EMMERLING, F.; CAMARGO, P. H. C. Challenges and opportunities in the bottom-up mechanochemical synthesis of noble metal nanoparticles. **Journal of Materials Chemistry A**, v. 8, n. 32, p. 16114–16141, 2020.

PANWAR, N. L.; KAUSHIK, S. C.; KOTHARI, S. Role of renewable energy sources in environmental protection: A review. **Renewable and Sustainable Energy Reviews**, v. 15, n. 3, p. 1513–1524, abr. 2011.

PARACCHINO, A.; LAPORTE, V.; SIVULA, K.; GRÄTZEL, M.; THIMSEN, E. Highly active oxide photocathode for photoelectrochemical water reduction. **Nature Materials**, v. 10, n. 6, p. 456–461, 8 jun. 2011.

PASQUALE, I. DE; PORTO, C. LO; DELL’EDERA, M.; CURRI, M. L.; COMPARELLI, R. TiO2-based nanomaterials assisted photocatalytic treatment for virus inactivation: perspectives and applications. **Current Opinion in Chemical Engineering**, v. 34, 2021.

PASQUALE, I. DE; PORTO, C. LO; EDERA, M. D.; PETRONELLA, F.; AGOSTIANO, A.; CURRI, M. L.; COMPARELLI, R. Photocatalytic TiO2-Based Nanostructured Materials for Microbial Inactivation. **Catalysts**, v. 10, n. November, 2020.

PENG, C.; FAN, W.; LI, Q.; HAN, W.; CHEN, X.; ZHANG, G.; YAN, Y.; GU, Q.; WANG, C.; ZHANG, H.; ZHANG, P. **Boosting photocatalytic activity**

through tuning electron spin states and external magnetic fieldsJournal of Materials Science and Technology Chinese Society of Metals, , 10 jul. 2022.

PESSANHA, E. C.; A. F. MENEZES, F.; GUIMARÃES, A. O.; MENDES JARDIM, P.; MARINKOVIC, B. A. Cu2O nanocubes/TiO2 heterostructure and its adsorption and photocatalytic properties for tetracycline removal. **Journal of Photochemistry and Photobiology A: Chemistry**, v. 440, n. December 2022, p. 114652, mar. 2023.

PIROZZI, D.; IMPARATO, C.; D'ERRICO, G.; VITIELLO, G.; ARONNE, A.; SANNINO, F. Three-year lifetime and regeneration of superoxide radicals on the surface of hybrid TiO2 materials exposed to air. **Journal of Hazardous Materials**, v. 387, n. September 2019, p. 121716, 2020.

POLISHCHUK, I.; BIANCO-STEIN, N.; LANG, A.; KURASHVILI, M.; CASPARY TOROKER, M.; KATSMAN, A.; FELDMANN, J.; POKROY, B. Strong Band Gap Blueshift in Copper (I) Oxide Semiconductor via Bioinspired Route. **Advanced Functional Materials**, v. 30, n. 13, 1 mar. 2020.

PRAVEEN, P.; VIRUTHAGIRI, G.; MUGUNDAN, S.; SHANMUGAM, N. Structural, optical and morphological analyses of pristine titanium di-oxide nanoparticles - Synthesized via sol-gel route. **Spectrochimica Acta - Part A: Molecular and Biomolecular Spectroscopy**, v. 117, p. 622–629, 2014.

PREDA, I.; MOSSANEK, R. J. O.; ABBATE, M.; ALVAREZ, L.; MÉNDEZ, J.; GUTIÉRREZ, A.; SORIANO, L. Surface contributions to the XPS spectra of nanostructured NiO deposited on HOPG. **Surface Science**, v. 606, n. 17–18, p. 1426–1430, set. 2012.

PUNIA, P.; BHARTI, M. K.; CHALIA, S.; DHAR, R.; RAVELO, B.; THAKUR, P.; THAKUR, A. Recent advances in synthesis, characterization, and applications of nanoparticles for contaminated water treatment- A review. **Ceramics International**, v. 47, n. 2, p. 1526–1550, 2021.

QIU, X.; MIYAUCHI, M.; SUNADA, K.; MINOSHIMA, M.; LIU, M.; LU, Y.; LI, D.; SHIMODAIRA, Y.; HOSOGI, Y.; KURODA, Y.; HASHIMOTO, K. Hybrid CuxO/TiO2 Nanocomposites As Risk-Reduction Materials in Indoor Environments. **ACS Nano**, v. 6, n. 2, p. 1609–1618, 28 fev. 2012.

QUTUB, N.; SINGH, P.; SABIR, S.; SAGADEVAN, S.; OH, W.-C. Enhanced photocatalytic degradation of Acid Blue dye using CdS/TiO2 nanocomposite. **Scientific Reports**, v. 12, n. 1, p. 1–18, 2022.

RANA, P.; JEEVANANDAM, P. A Facile Synthetic Approach for TiO $_2$ @NiO Core-shell Nanoparticles using TiO $_2$ @Ni(OH) $_2$ Precursors and their Photocatalytic Application. **ChemNanoMat**, v. 10, n. 3, 12 mar. 2024.

RESÉNDIZ-RAMÍREZ, R.; RODRÍGUEZ-LÓPEZ, A.; DÍAZ-REAL, J. A.; DELGADO-ARENAS, H. F.; OSORNIO-VILLA, A.; HERNÁNDEZ-LEOS, R.; VIVIER, V.; ANTAÑO-LÓPEZ, R. Reaction Mechanisms of the Electrosynthesis of Magnetite Nanoparticles Studied by Electrochemical Impedance Spectroscopy. **ACS Omega**, v. 7, n. 1, p. 761–772, 11 jan. 2022.

ROCHKIND, M.; PASTERNAK, S.; PAZ, Y. **Using dyes for evaluating photocatalytic properties: A critical reviewMolecules**MDPI AG, , 1 jan. 2015.

ROGOWSKA, J.; CIESZYNSKA-SEMENOWICZ, M.; RATAJCZYK, W.; WOLSKA, L. Micropollutants in treated wastewater. **Ambio**, v. 49, n. 2, p. 487–503, 2020.

RUAN, X. *et al.* Favorable Energy Band Alignment of TiO2 Anatase/Rutile Heterophase Homojunctions Yields Photocatalytic Hydrogen Evolution with Quantum Efficiency Exceeding 45.6%. **Advanced Energy Materials**, v. 12, n. 16, p. 1–9, 2022.

RUAN, X.; LI, S.; HUANG, C.; ZHENG, W.; CUI, X.; RAVI, S. K. Catalyzing Artificial Photosynthesis with TiO $_2$ Heterostructures and Hybrids: Emerging Trends in a Classical yet Contemporary Photocatalyst. **Advanced Materials**, 6 dez. 2023.

RUUS, R.; KIKAS, A.; SAAR, A.; AUSMEESB E NDMMISTE, O. A.; AARIK, J.; AIDLA, A.; UUSTARED, T. **Ti 2p AND 0 1s X-RAY ABSORPTION OF TiOz POLYMORPHSSolid State Communications**. [s.l: s.n.].

SAMARAI, M. AL; HAHN, A. W.; BEHESHTI ASKARI, A.; CUI, Y. T.; YAMAZOE, K.; MIYAWAKI, J.; HARADA, Y.; RÜDIGER, O.; DEBEER, S. Elucidation of Structure-Activity Correlations in a Nickel Manganese Oxide Oxygen Evolution Reaction Catalyst by Operando Ni L-Edge X-ray Absorption Spectroscopy and 2p3d Resonant Inelastic X-ray Scattering. **ACS Applied Materials and Interfaces**, v. 11, n. 42, p. 38595–38605, 23 out. 2019.

SANGWICHIEN, C.; ARANOVICH, G. **Density functional theory predictions of adsorption isotherms with hysteresis loopsColloids and Surfaces A: Physicochemical and Engineering Aspects**. [s.l: s.n.]. Disponível em: <www.elsevier.com/locate/colsurfa>.

SANNINO, F.; PERNICE, P.; IMPARATO, C.; ARONNE, A.; D’ERRICO, G.; MINIERI, L.; PERFETTI, M.; PIROZZI, D. Hybrid TiO2-acetylacetonate amorphous gel-derived material with stably adsorbed superoxide radical active in oxidative degradation of organic pollutants. **RSC Advances**, v. 5, n. 114, p. 93831–93839, 2015.

SARKER, A. K.; AZAD, A. K.; RASUL, M. G.; DOPPALAPUDI, A. T. **Prospect of Green Hydrogen Generation from Hybrid Renewable Energy Sources: A ReviewEnergies**MDPI, , 1 fev. 2023.

SEKAR, K.; CHUAICHAM, C.; VELLAICHAMY, B.; LI, W.; ZHUANG, W.; LU, X.; OHTANI, B.; SASAKI, K. Cubic Cu2O nanoparticles decorated on TiO2 nanofiber heterostructure as an excellent synergistic photocatalyst for H2 production and sulfamethoxazole degradation. **Applied Catalysis B: Environmental**, v. 294, 5 out. 2021.

SERPONE, N.; EMELINE, A. V. Suggested terms and definitions in photocatalysis and radiocatalysis. **International Journal of Photoenergy**, v. 4, n. 3, p. 93–131, 2002.

SHAHBAZI, N.; ZARE-DORABEI, R. A Facile Colorimetric and Spectrophotometric Method for Sensitive Determination of Metformin in Human Serum Based on Citrate-Capped Gold Nanoparticles: Central Composite Design Optimization. **ACS Omega**, v. 4, n. 17, p. 17519–17526, 22 out. 2019.

SHARMA, M.; MANDAL, M. K.; PANDEY, S.; KUMAR, R.; DUBEY, K. K. Visible-Light-Driven Photocatalytic Degradation of Tetracycline Using Heterostructured Cu2O-TiO2Nanotubes, Kinetics, and Toxicity Evaluation of Degraded Products on Cell Lines. **ACS Omega**, v. 7, n. 37, p. 33572–33586, 20 set. 2022.

SHARMA, P. K.; SINGH, M. K.; SHARMA, G. D.; AGRAWAL, A. NiO nanoparticles: Facile route synthesis, characterization and potential towards third generation solar cell. **Materials Today: Proceedings**, v. 43, p. 3061–3065, 2021.

SHI, Y.; YANG, Z.; WANG, B.; AN, H.; CHEN, Z.; CUI, H. Adsorption and photocatalytic degradation of tetracycline hydrochloride using a palygorskite-supported Cu2O-TiO2 composite. **Applied Clay Science**, v. 119, p. 311–320, 1 jan. 2016.

SHIRAZI, M.; FUINHAS, J. A. Portfolio decisions of primary energy sources and economic complexity: The world’s large energy user evidence. **Renewable Energy**, v. 202, p. 347–361, jan. 2023.

SHONEYE, A.; CHANG, J. SEN; CHONG, M. N.; TANG, J. Recent progress in photocatalytic degradation of chlorinated phenols and reduction of heavy metal ions in water by TiO2-based catalysts. **International Materials Reviews**, v. 67, n. 1, p. 47–64, 2022.

SHU, J.; WANG, Z.; HUANG, Y.; HUANG, N.; REN, C.; ZHANG, W. Adsorption removal of Congo red from aqueous solution by polyhedral Cu2O nanoparticles: Kinetics, isotherms, thermodynamics and mechanism analysis. **Journal of Alloys and Compounds**, v. 633, p. 338–346, 2015.

SOEDER, D. J. Fossil Fuels and Climate Change. *Em*: **Fracking and the Environment**. Cham: Springer International Publishing, 2021. p. 155–185.

SOPICKA-LIZER, M. **High-energy ball milling**. [s.l: s.n.].

SORIANO ’, L.; ABBATE, M.; VOGEL, J.; FUGGLE ’, J. C.; FERNTIDEZ, A.; GO&LEZ-ELIPE, A. R.; SACCHI, M.; SANZ, J. M. **The electronic structure of mesoscopic NiO particles**. [s.l: s.n.].

SPEK, M. VAN DER *et al.* Perspective on the hydrogen economy as a pathway to reach net-zero CO2 emissions in Europe†. **Energy and Environmental Science**, v. 15, n. 3, p. 1034–1077, 2 fev. 2022.

SU, Y.; LI, H.; MA, H.; ROBERTSON, J.; NATHAN, A. Controlling Surface Termination and Facet Orientation in Cu2O Nanoparticles for High Photocatalytic Activity: A Combined Experimental and Density Functional Theory Study. **ACS Applied Materials and Interfaces**, v. 9, n. 9, p. 8100–8106, 8 mar. 2017.

SUN, B.; ZHOU, G.; GAO, T.; ZHANG, H.; YU, H. NiO nanosheet/TiO 2 nanorod-constructed p-n heterostructures for improved photocatalytic activity. **Applied Surface Science**, v. 364, p. 322–331, 28 fev. 2016.

SUN, S.; ZHANG, XIAOJING; YANG, Q.; LIANG, S.; ZHANG, XIAOZHE; YANG, Z. **Cuprous oxide (Cu2O) crystals with tailored architectures: A comprehensive review on synthesis, fundamental properties, functional modifications and applicationsProgress in Materials Science**Elsevier Ltd, , 1 jul. 2018.

TAN, C. S.; HSU, S. C.; KE, W. H.; CHEN, L. J.; HUANG, M. H. Facet-dependent electrical conductivity properties of Cu2O crystals. **Nano Letters**, v. 15, n. 3, p. 2155–2160, 11 mar. 2015.

TAUDUL, B.; TIELENS, F.; CALATAYUD, M. On the Origin of Raman Activity in Anatase TiO2 (Nano)Materials: An Ab Initio Investigation of Surface and Size Effects. **Nanomaterials**, v. 13, n. 12, p. 1856, 14 jun. 2023.

THOMAS, A. G. *et al.* Comparison of the electronic structure of anatase and rutile TiO2 single-crystal surfaces using resonant photoemission and x-ray absorption spectroscopy. **Physical Review B - Condensed Matter and Materials Physics**, v. 75, n. 3, p. 1–12, 2007.

THOMMES, M.; KANEKO, K.; NEIMARK, A. V.; OLIVIER, J. P.; RODRIGUEZ-REINOSO, F.; ROUQUEROL, J.; SING, K. S. W. Physisorption of gases, with special reference to the evaluation of surface area and pore size distribution (IUPAC Technical Report). **Pure and Applied Chemistry**, v. 87, n. 9–10, p. 1051–1069, 1 out. 2015.

TOIT, M. H. DU; AVDEENKOV, A. V.; BESSARABOV, D. **Reviewing H2 Combustion: A Case Study for Non-Fuel-Cell Power Systems and Safety in Passive Autocatalytic RecombinersEnergy and Fuels**American Chemical Society, , 21 jun. 2018.

TSUZUKI, T. Mechanochemical synthesis of metal oxide nanoparticles. **Communications Chemistry**, v. 4, n. 1, 2021.

TU, W.; GUO, W.; HU, J.; HE, H.; LI, H.; LI, Z.; LUO, W.; ZHOU, Y.; ZOU, Z. State-of-the-art advancements of crystal facet-exposed photocatalysts beyond TiO2: Design and dependent performance for solar energy conversion and environment applications. **Materials Today**, v. 33, p. 75–86, mar. 2020.

VALENTIN, C. DI; FINAZZI, E.; PACCHIONI, G.; SELLONI, A.; LIVRAGHI, S.; PAGANINI, M. C.; GIAMELLO, E. N-doped TiO2: Theory and experiment. **Chemical Physics**, v. 339, n. 1–3, p. 44–56, 2007.

VÁZQUEZ-LÓPEZ, A.; MAESTRE, D.; MARTÍNEZ-CASADO, R.; RAMÍREZ-CASTELLANOS, J.; PÍŠ, I.; NAPPINI, S.; CREMADES, A. Unravelling the role of lithium and nickel doping on the defect structure and phase transition of anatase TiO2 nanoparticles. **Journal of Materials Science**, v. 57, n. 14, p. 7191–7207, 1 abr. 2022.

VILLAMAYOR, A.; POMONE, T.; PERERO, S.; FERRARIS, M.; BARRIO, V. L.; G-BERASATEGUI, E.; KELLY, P. Development of photocatalytic nanostructured TiO2 and NiO/TiO2 coatings by DC magnetron sputtering for photocatalytic applications. **Ceramics International**, v. 49, n. 11, p. 19309–19317, 1 jun. 2023.

VILLAMENA, F. A.; HADAD, C. M.; ZWEIER, J. L. Kinetic study and theoretical analysis of hydroxyl radical trapping and spin adduct decay of alkoxycarbonyl and dialkoxyphosphoryl nitrones in aqueous media. **Journal of Physical Chemistry A**, v. 107, n. 22, p. 4407–4414, 5 jun. 2003.

WANG, H. *et al.* Nickel L-edge soft X-ray spectroscopy of nickel-iron hydrogenases and model compounds - Evidence for high-spin nickel(II) in the active enzyme. **Journal of the American Chemical Society**, v. 122, n. 43, p. 10544–10552, 1 nov. 2000.

WANG, H.; BUTORIN, S. M.; YOUNG, A. T.; GUO, J. Nickel oxidation states and spin states of bioinorganic complexes from nickel L-edge X-ray absorption and resonant inelastic X-ray scattering. **Journal of Physical Chemistry C**, v. 117, n. 47, p. 24767–24772, 27 nov. 2013.

WANG, M.; HU, Y.; HAN, J.; GUO, R.; XIONG, H.; YIN, Y. TiO2/NiO hybrid shells: P-n junction photocatalysts with enhanced activity under visible light. **Journal of Materials Chemistry A**, v. 3, n. 41, p. 20727–20735, 2015.

WANG, P.; TIAN, Y.; WANG, H.; ZHANG, J.; KONG, L.; ZUO, W.; LI, D.; YIN, L. Strong adsorption of tetracycline on octahedral Cu2O nanocrystals exposed with {111} facets: Adsorption behavior and mechanism insight. **Applied Surface Science**, v. 542, 15 mar. 2021.

WANG, T. T.; RAGHUNATH, P.; LIN, Y. G.; LIN, M. C. Synergistic Effect of Hydrogenation and Thiocyanate Treatments on Ag-Loaded TiO2 Nanoparticles for Solar-to-Hydrogen Conversion. **Journal of Physical Chemistry C**, v. 121, n. 18, p. 9681–9690, 11 maio 2017.

WANG, T. TE; CHIANG, C. L.; LIN, Y. C.; SRINIVASADESIKAN, V.; LIN, M. C.; LIN, Y. G. KSCN-activation of hydrogenated NiO/TiO2 for enhanced photocatalytic hydrogen evolution. **Applied Surface Science**, v. 511, 1 maio 2020.

WANG, Y.; TAO, J.; WANG, X.; WANG, Z.; ZHANG, M.; HE, G.; SUN, Z. A unique Cu2O/TiO2 nanocomposite with enhanced photocatalytic performance under visible light irradiation. **Ceramics International**, v. 43, n. 6, p. 4866–4872, 2017.

WEI, B.; YANG, N.; PANG, F.; GE, J. Cu2O-CuO hollow nanospheres as a heterogeneous catalyst for synergetic oxidation of CO. **Journal of Physical Chemistry C**, v. 122, n. 34, p. 19524–19531, 30 ago. 2018.

WEI, Z.; LIU, J.; SHANGGUAN, W. A review on photocatalysis in antibiotic wastewater: Pollutant degradation and hydrogen production. **Chinese Journal of Catalysis**, v. 41, n. 10, p. 1440–1450, 2020.

WEN, M.; MORI, K.; KUWAHARA, Y.; AN, T.; YAMASHITA, H. **Design and architecture of metal organic frameworks for visible light enhanced hydrogen productionApplied Catalysis B: Environmental**Elsevier B.V., , 2017.

WEST, A. **Solid State Chemistry and its applications**. Second ed. [s.l.] WILEY, 2014.

WILKINSON, J. L. *et al.* Pharmaceutical pollution of the world's rivers. **Proceedings of the National Academy of Sciences**, v. 119, n. 8, p. 1–10, 22 fev. 2022.

WU, S. C.; TAN, C. S.; HUANG, M. H. Strong Facet Effects on Interfacial Charge Transfer Revealed through the Examination of Photocatalytic Activities of Various Cu2O–ZnO Heterostructures. **Advanced Functional Materials**, v. 27, n. 9, 2017.

WU, Y. A. *et al.* Facet-dependent active sites of a single Cu2O particle photocatalyst for CO2 reduction to methanol. **Nature Energy**, v. 4, n. 11, p. 957–968, 1 nov. 2019.

WULANDARI, P.; NAGAHIRO, T.; FUKADA, N.; KIMURA, Y.; NIWANO, M.; TAMADA, K. Characterization of citrates on gold and silver nanoparticles. **Journal of Colloid and Interface Science**, v. 438, p. 244–248, 5 jan. 2015.

XIA, C.; HONG CHUONG NGUYEN, T.; CUONG NGUYEN, X.; YOUNG KIM, S.; NGUYEN, D. L. T.; RAIZADA, P.; SINGH, P.; NGUYEN, V. H.; CHIEN NGUYEN, C.; CHINH HOANG, V.; LE, Q. VAN. Emerging cocatalysts in TiO2-based photocatalysts for light-driven catalytic hydrogen evolution: Progress and perspectives. **Fuel**, v. 307, n. August 2021, p. 121745, 2022.

XING, C.; ZHANG, Y.; LIU, Y.; WANG, X.; LI, J.; MARTÍNEZ-ALANIS, P. R.; SPADARO, M. C.; GUARDIA, P.; ARBIOL, J.; LLORCA, J.; CABOT, A.

Photodehydrogenation of Ethanol over Cu2O/TiO2 Heterostructures. **Nanomaterials**, v. 11, n. 6, p. 1–15, 2021a.

___. Photodehydrogenation of Ethanol over Cu2O/TiO2 Heterostructures. **Nanomaterials**, v. 11, n. 6, p. 1–15, 2021b.

YAN, L.; YANG, F.; TAO, C. Y.; LUO, X.; ZHANG, L. Highly efficient and stable Cu2O–TiO2 intermediate photocatalytic water splitting. **Ceramics International**, v. 46, n. 7, p. 9455–9463, 2020.

YANG, Y.; ZHENG, X.; REN, W.; LIU, J.; FU, X.; MENG, S.; CHEN, S.; CAI, C. Recent advances in special morphologic photocatalysts for NOx removal. **Frontiers of Environmental Science and Engineering**, v. 16, n. 11, p. 1–15, 2022.

YEN, H.; SEO, Y.; KALIAGUINE, S.; KLEITZ, F. Role of Metal-Support Interactions, Particle Size, and Metal-Metal Synergy in CuNi Nanocatalysts for H2 Generation. **ACS Catalysis**, v. 5, n. 9, p. 5505–5511, 7 ago. 2015.

YOO, I. HAN; KALANUR, S. S.; SEO, H. A nanoscale p–n junction photoelectrode consisting of an NiOx layer on a TiO2/CdS nanorod core-shell structure for highly efficient solar water splitting. **Applied Catalysis B: Environmental**, v. 250, p. 200–212, 5 ago. 2019.

YU, C.; LI, M.; YANG, D.; PAN, K.; YANG, F.; XU, Y.; YUAN, L.; QU, Y.; ZHOU, W. NiO nanoparticles dotted TiO2 nanosheets assembled nanotubes P-N heterojunctions for efficient interface charge separation and photocatalytic hydrogen evolution. **Applied Surface Science**, v. 568, 1 dez. 2021.

YU, J.; WANG, W.; CHENG, B. Synthesis and Enhanced Photocatalytic Activity of a Hierarchical Porous Flowerlike *p–n* Junction NiO/TiO_2 Photocatalyst. **Chemistry – An Asian Journal**, v. 5, n. 12, p. 2499–2506, 3 dez. 2010.

YUAN, G. Z.; HSIA, C. F.; LIN, Z. W.; CHIANG, C.; CHIANG, Y. W.; HUANG, M. H. Highly Facet-Dependent Photocatalytic Properties of Cu2O Crystals Established through the Formation of Au-Decorated Cu2O Heterostructures. **Chemistry - A European Journal**, v. 22, n. 35, p. 12548–12556, 2016.

ZALESKA, A. Doped-TiO 2 : A Review. **Recent Patents on Engineering**, n. 1, p. 157–164, 2008.

ZENG, Y.; XUE, J.; HE, M.; LI, C.; ZHU, W.; LI, S. Investigation of interfacial charge transfer in CuxO@TiO2 heterojunction nanowire arrays towards highly efficient solar water splitting. **Electrochimica Acta**, v. 367, 20 jan. 2021a.

___. Investigation of interfacial charge transfer in CuxO@TiO2 heterojunction nanowire arrays towards highly efficient solar water splitting. **Electrochimica Acta**, v. 367, 20 jan. 2021b.

ZHANG, J.; ZHOU, P.; LIU, J.; YU, J. New understanding of the difference of photocatalytic activity among anatase, rutile and brookite TiO2. **Physical Chemistry Chemical Physics**, v. 16, n. 38, p. 20382–20386, 2014.

ZHANG, Q. Q.; YING, G. G.; PAN, C. G.; LIU, Y. S.; ZHAO, J. L. Comprehensive evaluation of antibiotics emission and fate in the river basins of China: Source analysis, multimedia modeling, and linkage to bacterial resistance. **Environmental Science and Technology**, v. 49, n. 11, p. 6772–6782, 2015.

ZHANG, W.; HE, H.; LI, H.; DUAN, L.; ZU, L.; ZHAI, Y.; LI, W.; WANG, L.; FU, H.; ZHAO, D. **Visible-Light Responsive TiO2-Based Materials for Efficient Solar Energy UtilizationAdvanced Energy Materials**John Wiley and Sons Inc, , 1 abr. 2021.

ZHANG, Y. *et al.* Mechanochemical synthesis of nanostructured and composite oxide ceramics: From mechanisms to tailored properties. **International Journal of Applied Ceramic Technology**, v. 21, n. 2, p. 616–654, 13 mar. 2024.

ZHAO, Y.; SHU, Y.; LINGHU, X.; LIU, W.; DI, M.; ZHANG, C.; SHAN, D.; YI, R.; WANG, B. Modification engineering of TiO2-based nanoheterojunction photocatalysts. **Chemosphere**, v. 346, p. 140595, jan. 2024.

ZHENG, D.; ZHAO, H.; WANG, S.; HU, J.; CHEN, Z. Nio-tio2 p-n heterojunction for solar hydrogen generation. **Catalysts**, v. 11, n. 12, 1 dez. 2021.

ZHUANG, M.; ACHMON, Y.; CAO, Y.; LIANG, X.; CHEN, L.; WANG, H.; SIAME, B. A.; LEUNG, K. Y. Distribution of antibiotic resistance genes in the environment. **Environmental Pollution**, v. 285, p. 117402, 2021.

9.
Appendix A: Supplementary material to support Chapter 4

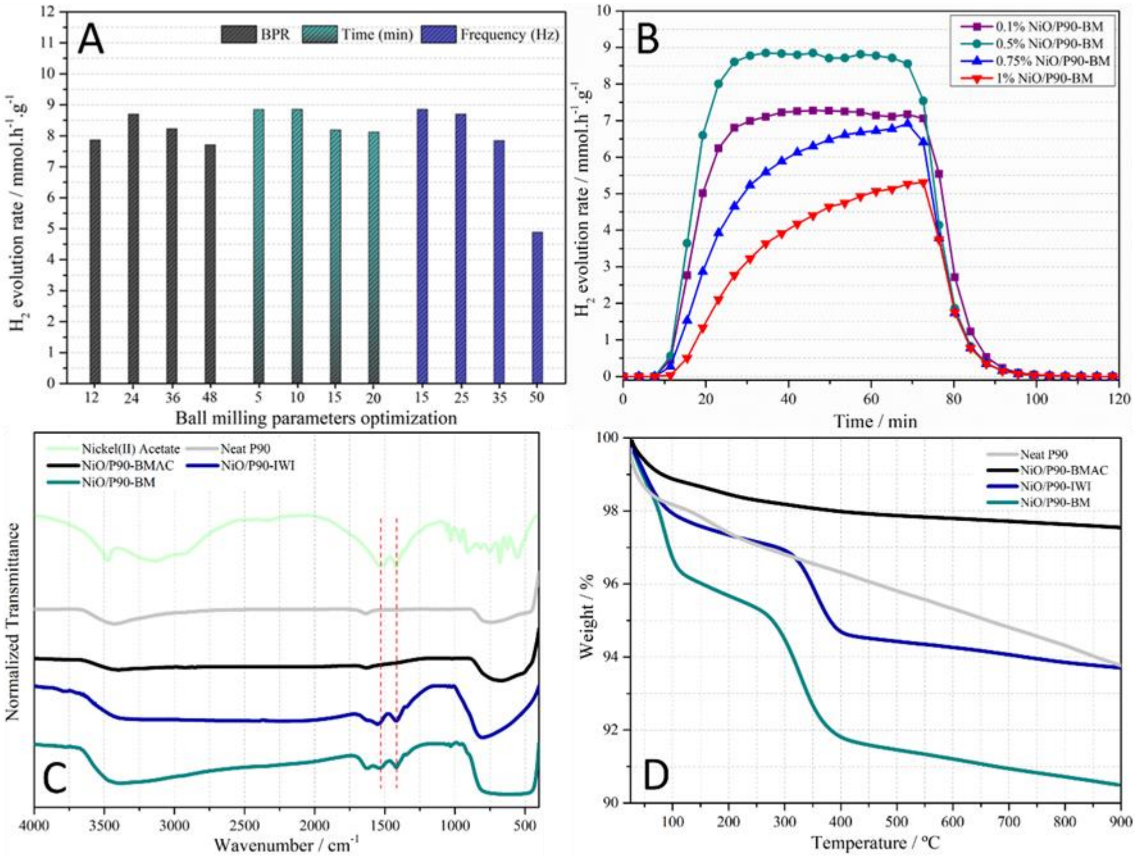

Figure 34: (a) Ball milling process optimization BM sample (0.5 wt.% Ni), (b) analysis of the influence of Ni content in the photocatalytic activity (BPR of 24, 10 min, and 15 Hz), (c) FTIR spectra, and (d) TGA curves of Neat P90, NiO/P90-BM, NiO/P90-IWI, and NiO/P90-BMAC samples (2 wt.% Ni).

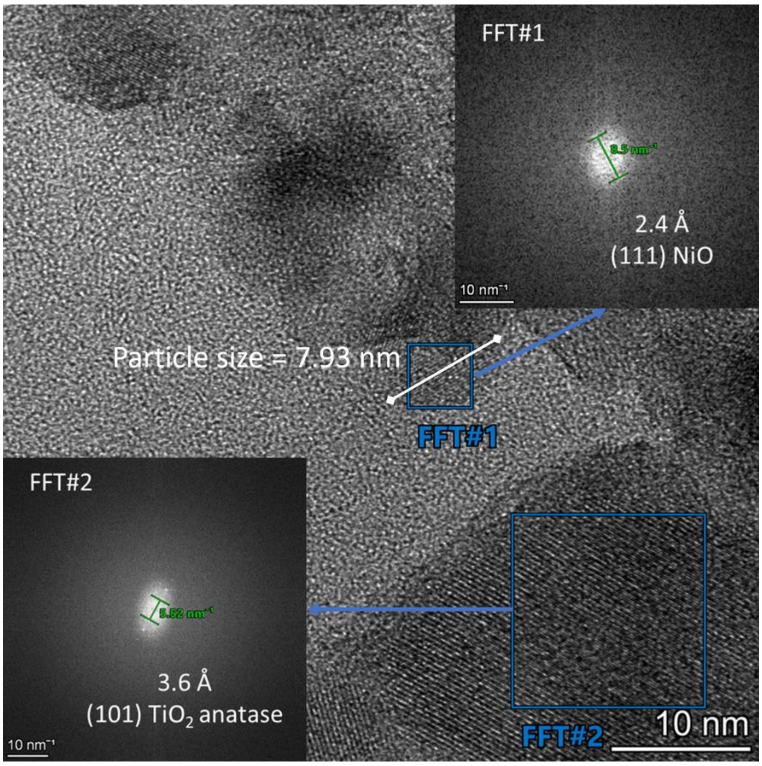

Figure 35: HRTEM image of NiO/P90-BMAC sample and insets of fast Fourier transform (FFT) of the crystal planes of NiO and TiO_2 (anatase) phases.

Table 4: Elemental nickel content comparison in a small and large areas measured for NiO/P90-BM (Fig. 17a), NiO/P90-IWI (Fig. 17b), and NiO/P90-BMAC (Fig. 17c) samples. The small areas are marked with yellow squares, while the large areas constitute entire field of micrographs in Figure 17.

Sample	**Selected area (wt%)**	**Total area (wt%)**
NiO/P90-BM	7.6 ± 1.5	2.0 ± 0.3
NiO/P90-IWI	7.6 ± 1.3	2.8 ± 0.4
NiO/P90-BMAC	65.3 ± 3.3	29 ± 3

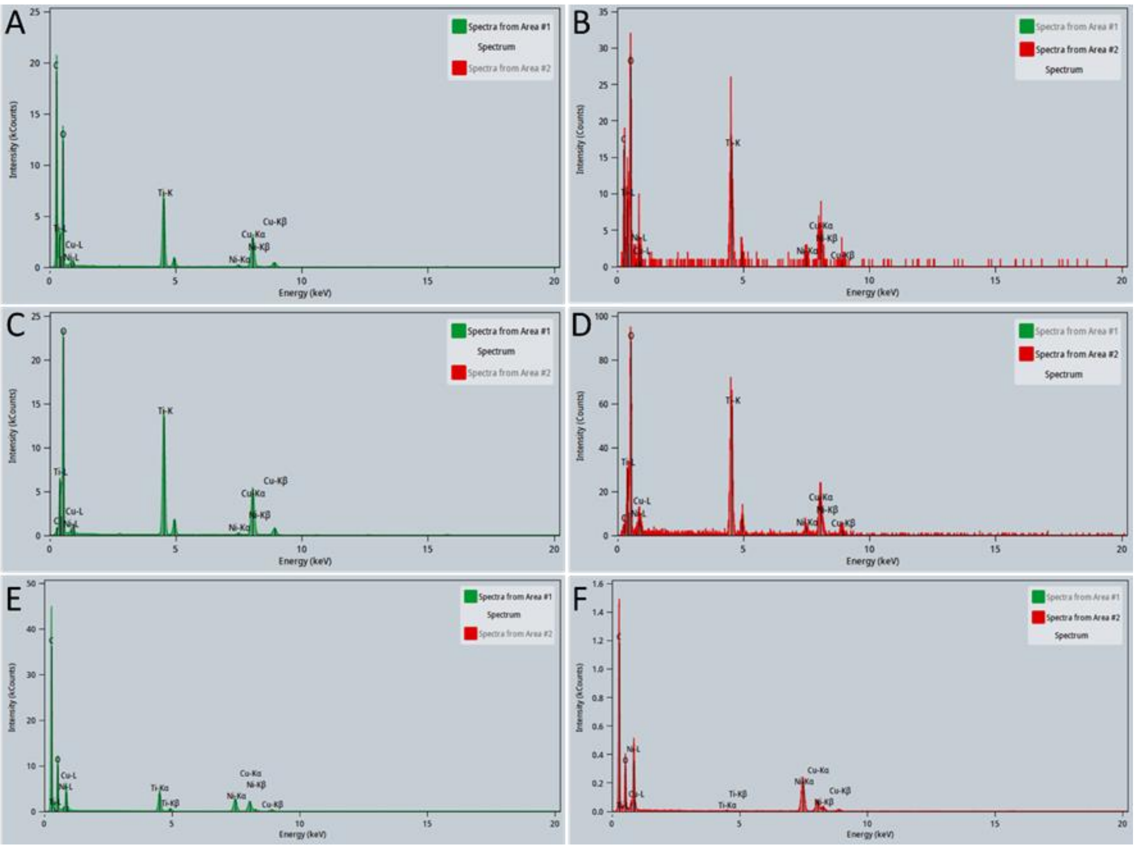

Figure 36: EDS spectra acquired in the area 1 (the whole areas in Fig. 17) and in the selected area 2 (the small selected areas in Fig. 17) of (a,b) NiO/P90-BM, (c,d) NiO/P90-IWI, and (e,f) NiO/P90-BMAC samples.

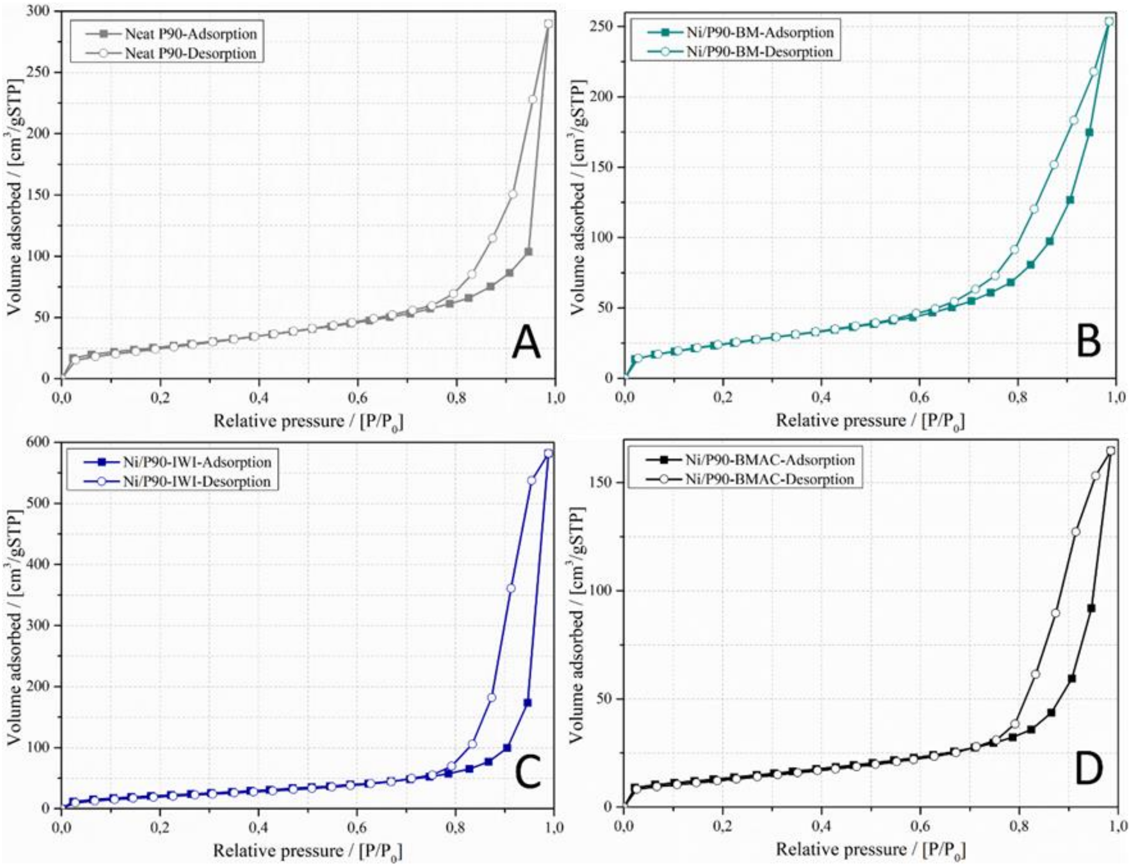

Figure 37: N_2 adsorption-desorption isotherms of (a) Neat P90, (b) NiO/P90-BM, (c) NiO/P90-IWI, and (d) NiO/P90-BMAC samples.

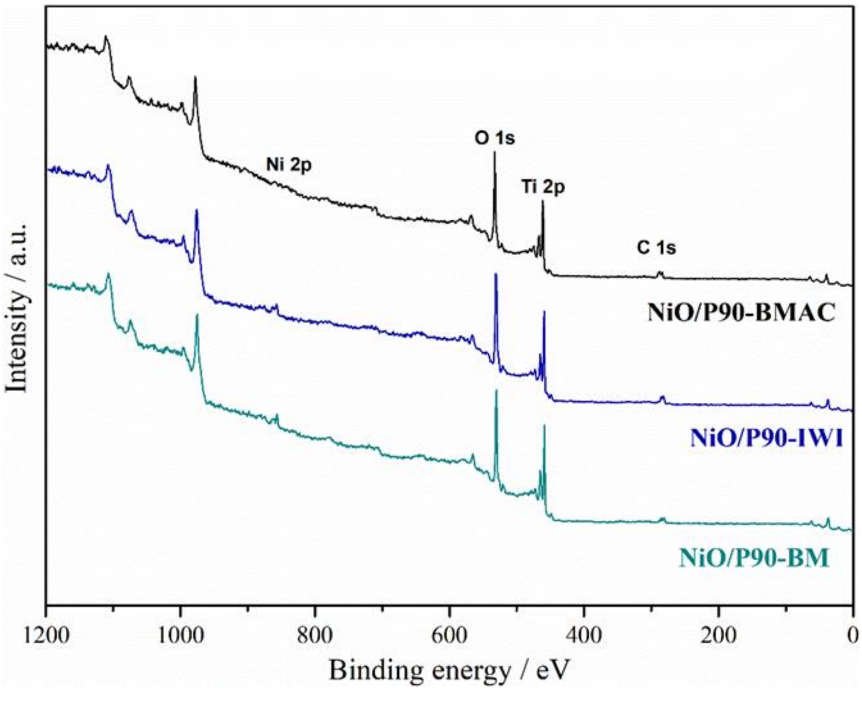

Figure 38: Survey XPS spectra of NiO/P90-BM, NiO/P90-IWI, and NiO/P90-BMAC samples.

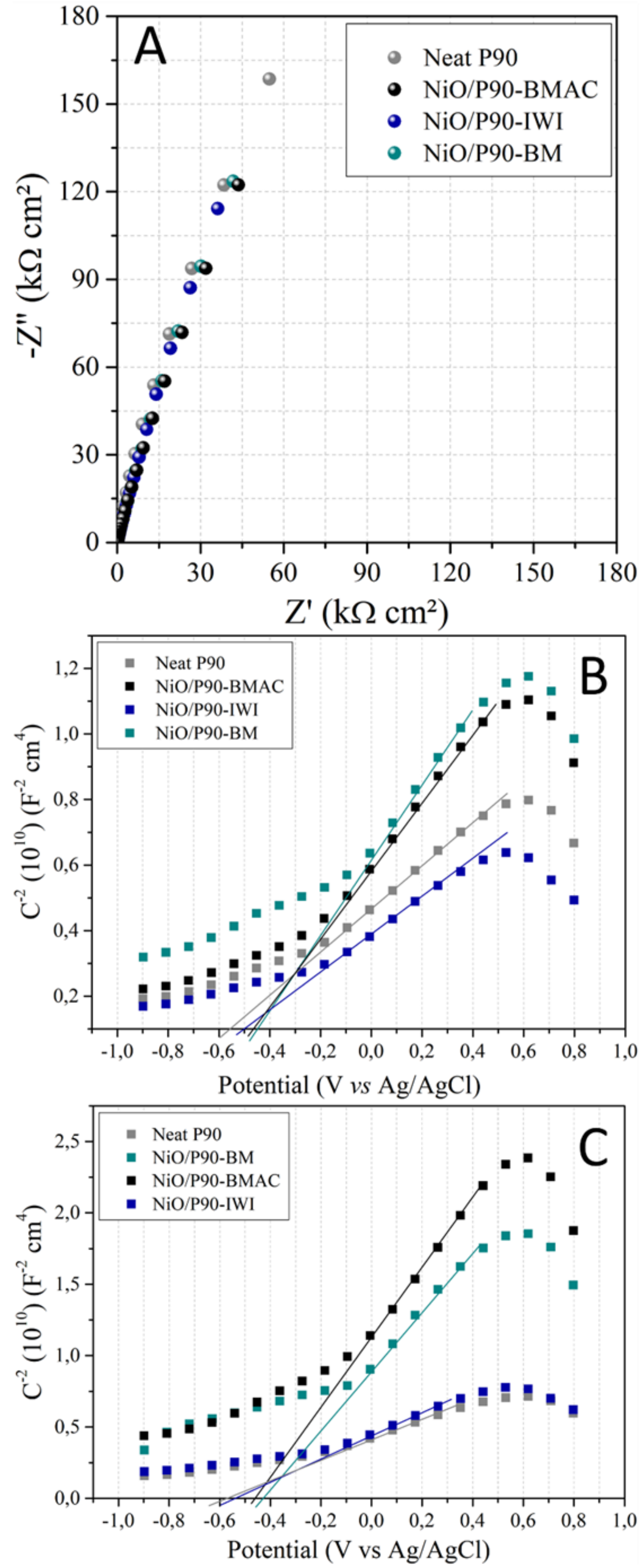

Figure 39: (a) Nyquist diagrams and M-S plots (b) under dark condition and (c) under UV radiation of neat P90, NiO/P90-BMAC, NiO/P90-IWI, and NiO/P90-BM samples.

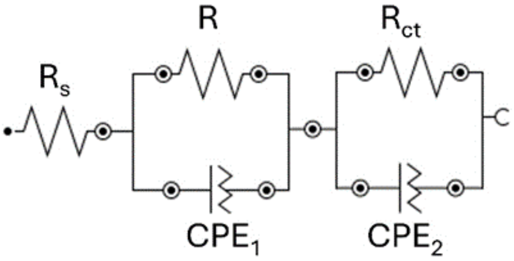

Figure 40: The equivalent circuit for the photoelectrochemical analysis of the Neat P90, NiO/P90-BM, NiO/P90-IWI, and NiO/P90-BMAC in the presence and absence of UV light.

Table 5: Electrochemical parameters from Nyquist diagram of the Neat P90, NiO/P90-BM, NiO/P90-IWI, and NiO/P90-BMAC in the presence and absence of UV light.

	Dark		**UV**	
Sample	R_{ct} (kΩ cm^{-2})	χ2	R_{ct} (kΩ cm^{-2})	χ2
Neat P90	1058	0.0002	340.5	0.001
NiO/P90-IWI	1702	0.0009	288.5	0.0005
NiO/P90-BMAC	1307	0.0007	333.9	0.0006
NiO/P90-BM	1468	0.0008	115.4	0.0005

10.
Appendix B: Supplementary material to support Chapter 6

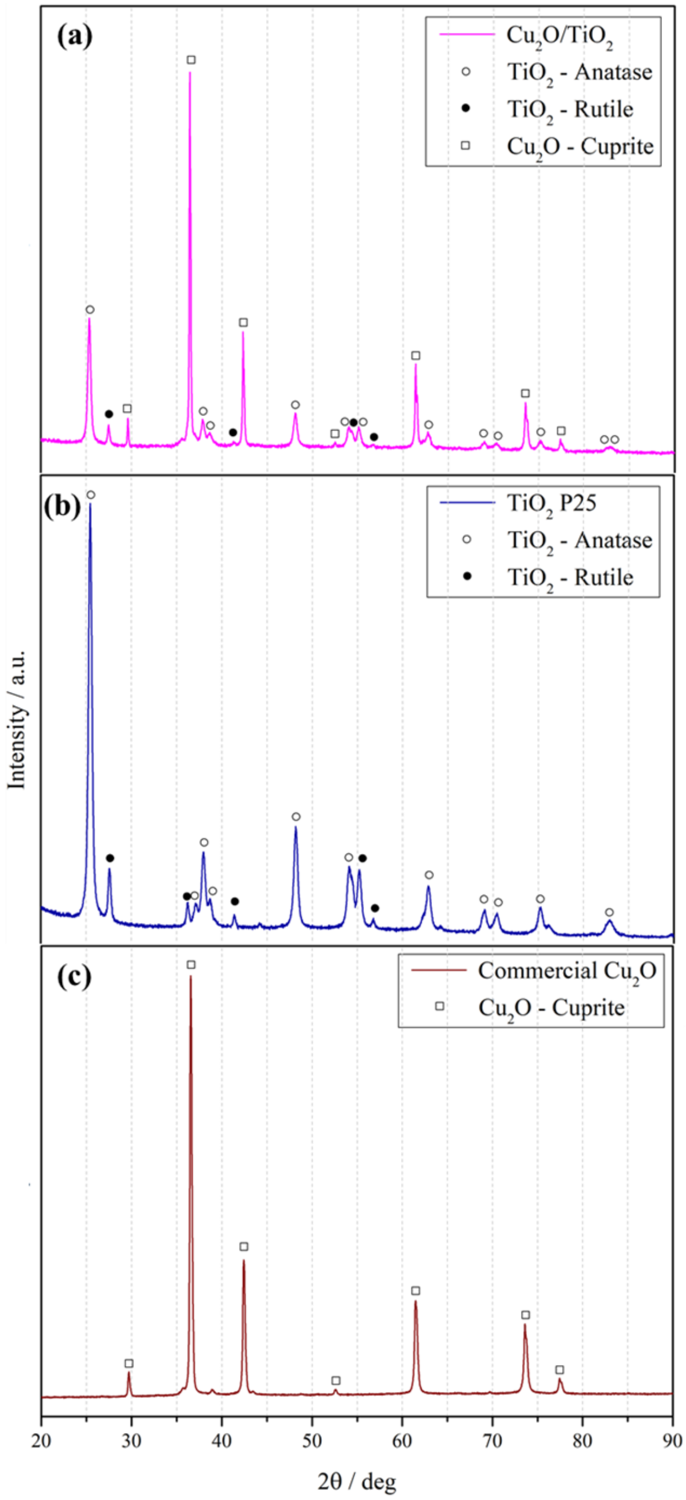

Figure 41: XRPD patterns for reference Cu_2O/TiO_2 heterostructure (a) TiO_2 P25 (b) and Commercial Cu_2O (c).

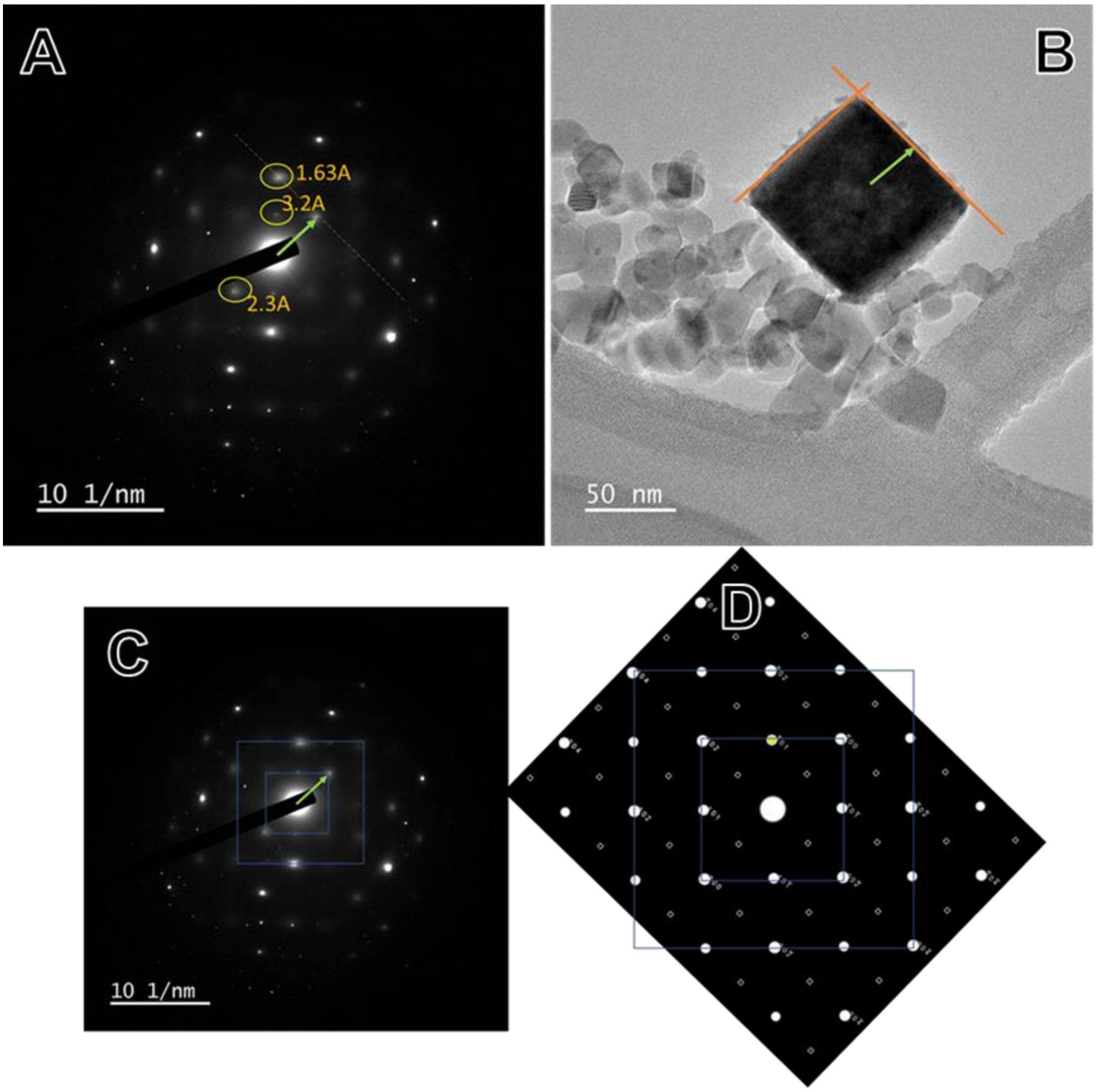

Figure 42: Details of selected area electron diffraction (SAED) patterns acquisition (b) and indexing (a, c, and d).

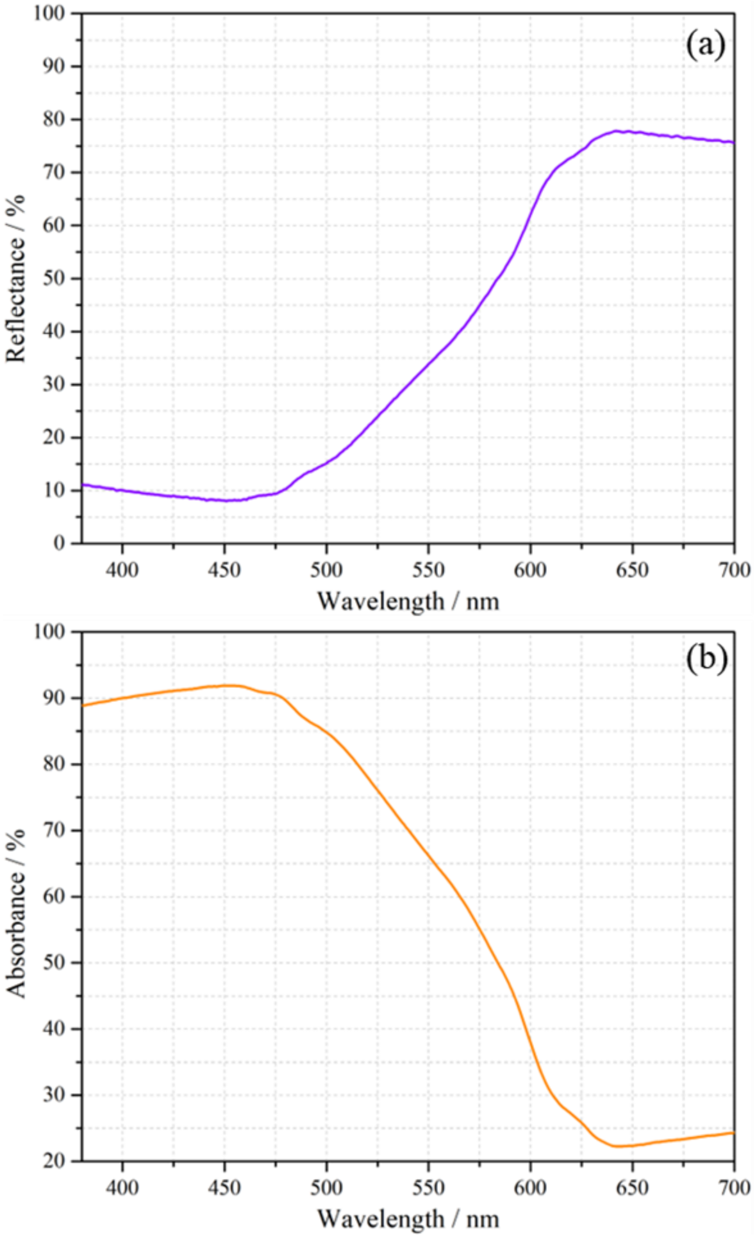

Figure 43: Reflectance *vs.* wavelength (a) and absorbance vs. wavelength (b) spectra for Cu_2O NCs/TiO_2 heterostructure.

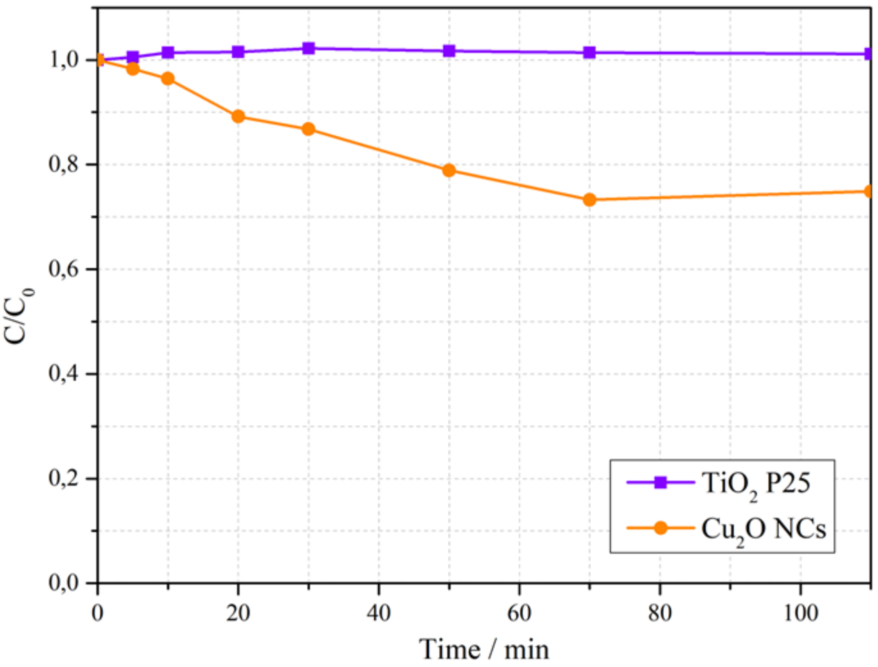

Figure 44: TC adsorption as a function of time in the presence of neat TiO_2 P25 (purple curve) and neat Cu_2O NCs (orange curve).

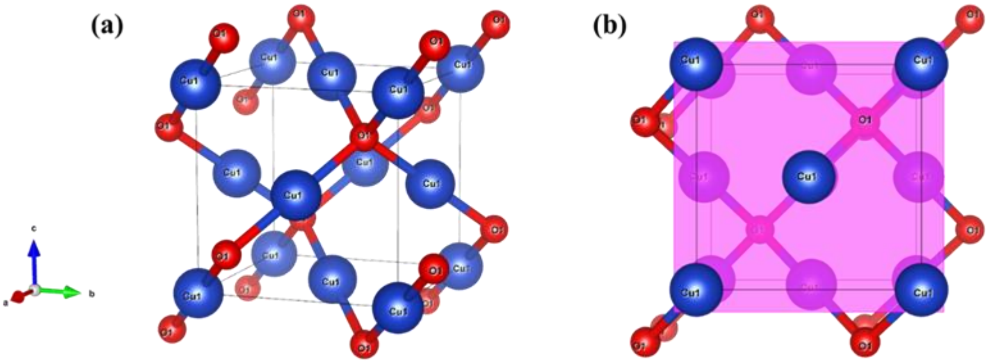

Figure 45: Cubic unit cell of cuprite (Cu_2O) phase generated by VESTA Version 3 software in the perspective view (a) and with the {100} family of planes highlighted (b).

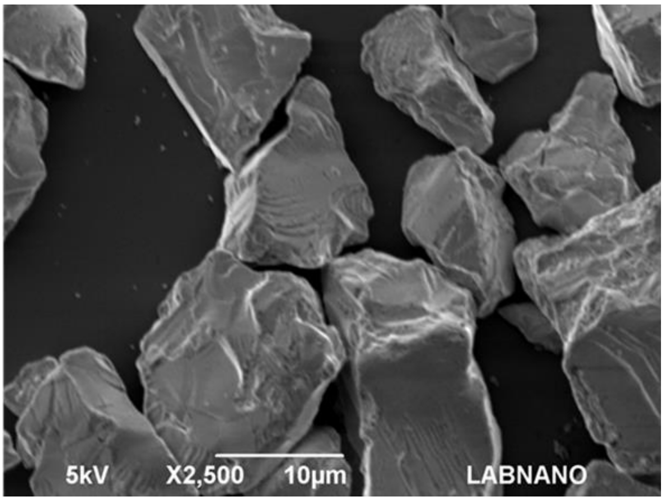

Figure 46: SEM image of the commercial Cu_2O used for preparation of the Cu_2O/TiO_2 reference sample.

11.
Appendix C: Scientific production

The results of this study are part of three articles:

⋆ Article published in the Journal of Photochemistry and Photobiology A: Chemistry (Elsevier), classified as A2 in Qualis Capes 2017-2020, Article DOI: 10.1016/j.jphotochem.2023.114652

Cu_2O nanocubes/TiO_2 heterostructure and its adsorption and photocatalytic properties for tetracycline removal

Emanuel C. Pessanha[a], Francine A. F. Menezes[b], André O. Guimarães[b], Paula Mendes Jardim[c], Bojan A. Marinkovic[a*]

[a]Department of Chemical and Materials Engineering, Pontifical Catholic University of Rio de Janeiro (PUC-Rio), 22453-900, Rio de Janeiro, RJ, Brazil
[b]Physical Science Laboratory, Northern Fluminense State University (UENF), 28013-602, Campos dos Goytacazes, Rio de Janeiro, Brazil
[c]Department of Metallurgical and Materials Engineering, Federal University of Rio de Janeiro, COPPE/UFRJ, 21941-972, Rio de Janeiro, Brazil

⋆ Article under review in the International Journal of Hydrogen Energy (Elsevier), classified as A1 in Qualis Capes 2017-2020:

Mechanochemical approach towards optimized Ni^{2+} spin configuration in NiO/TiO_2 heterojunction with enhanced solar-driven H_2 photoproduction

Emanuel do Couto-Pessanha[a,b], Victor Magno Paiva[c], Thiago J. A. Mori[d], Lluís Soler[b], Beatriz Canabarro[e], Paula Jardim[e], Eliane D'Elia[c], Jordi Llorca[b,*], Bojan A. Marinkovic[a,*]

[a]Department of Chemical and Materials Engineering, Pontifical Catholic University of Rio de Janeiro (PUC-Rio), 22453-900, Rio de Janeiro, RJ, Brazil
[b]Institute of Energy Technologies, Department of Chemical Engineering and Barcelona Research Center in Multiscale Science and Engineering, Universitat Politècnica de Catalunya, EEBE, Eduard Maristany 16, 08019 Barcelona, Spain

[c]Institute of Chemistry, Federal University of Rio de Janeiro, UFRJ, Rio de Janeiro 21941-909, Brazil
[d]Brazilian Synchrotron Light Laboratory (LNLS), Brazilian Center for Research in Energy and Materials (CNPEM), 13083-970, Campinas, SP, Brazil
[e]Department of Metallurgical and Materials Engineering, Federal University of Rio de Janeiro, COPPE/UFRJ, 21941-972, Rio de Janeiro, Brazil

⋆ Article to be submitted to the Journal of Physical Chemistry Letters (ACS), classified as A1 in Qualis Capes 2017-2020:

Efficient sunlight-driven photoproduction of superoxide and hydroxyl radicals by mechanochemically synthesized NiO/TiO$_2$ heterojunction: Insights from EPR/spin trapping

Emanuel do Couto-Pessanha[a,b], Francine A.F. Menezes[c], André O. Guimarães[c], Jordi Llorca[b,*], Bojan A. Marinkovic[a,*]

[a]Department of Chemical and Materials Engineering, Pontifical Catholic University of Rio de Janeiro (PUC-Rio), 22453-900, Rio de Janeiro, RJ, Brazil
[b]Institute of Energy Technologies, Department of Chemical Engineering and Barcelona Research Center in Multiscale Science and Engineering, Universitat Politècnica de Catalunya, EEBE, Eduard Maristany 16, 08019 Barcelona, Spain
[c]Physical Science Laboratory, Northern Fluminense State University (UENF), 28013-602 Campos dos Goytacazes, Rio de Janeiro, Brazil